

WASM: Minerals, Energy and Chemical Engineering

Assessment of Gas Adsorption Capacity in Shale Gas Reservoirs

Jie Zou

This thesis is presented for the Degree of

Doctor of Philosophy

of


Curtin University

February 2019

Declaration

To the best of my knowledge and belief, this thesis contains no material previously published by any other person, except where due acknowledgment has been made.

This thesis contains no material which has been accepted for the award of any other degrees or diplomas in any university.

Signature: 

Date: 17/04/2019

ABSTRACT

Unlike conventional natural gas, unconventional natural gas such as shale gas is stored in source rock and has drawn much attention all over the world. Shale gas contains not only free gas in pore space and natural fractures but also adsorbed gas on the matrix particle surface. As shale is very porous material with nano-scale pores, the amount of adsorbed gas in shale could be significant. To evaluate gas storage of shale gas system precisely, it is necessary to consider gas adsorption in shale. However, the gas adsorption capacity in shale is controlled by various parameters, including reservoir conditions (pressure and temperature) and internal parameters (composition, pore structure, and moisture content). In this study, we defined the controlling factors of gas adsorption capacity and adsorption kinetics in shale and introduced a prediction tool to estimate gas adsorption capacity in shale.

Shale samples in this study are from the Perth and Canning basins, Western Australia. High-pressure methane adsorption experiments were carried out on samples at different temperatures in both dry and wet conditions. The experiment results were fitted using the Langmuir model to obtain Langmuir volume and Langmuir pressure, which are the fundamental parameters for the evaluation of gas adsorption. Methane adsorption kinetics were also measured under different pressures and temperatures. The results of methane adsorption rate were fitted by the bidisperse diffusion model to determine parameters about diffusion in shale. The pore structure of the samples was studied using low-pressure adsorption experiment. Besides, some experimental data of methane adsorption in shale from references were also engaged to construct the prediction model.

The results of this study showed that temperature and moisture control methane adsorption capacity in shale gas system. The methane adsorption capacity decreases with increasing temperature. This negative effect of temperature on methane adsorption is more sensitive to high TOC shale samples than low TOC samples. Besides, the methane adsorption capacity is reduced by moisture, as moisture can occupy sorption sites and block pore throat in shale. Under actual reservoir condition, moisture and temperature work together. These two factors weaken each other on methane adsorption capacity in shale gas system.

Thermodynamic parameters were determined based on the temperature dependence of the Langmuir pressure. The results showed that organic matter releases more heat than clay minerals in terms of methane adsorption. Moreover, methane adsorbed on the organic matter has a different configuration from methane adsorbed on clay minerals. Comparing with wet samples, dry samples have more negative values of adsorption heat.

Methane adsorption rate in shale is positively related to temperature but not pressure. The results of effective diffusivity are more related to micropores (<2nm, from low-pressure CO₂ adsorption) than mesopores and macropores (2-100nm, from low-pressure N₂ adsorption). It is likely that micropores play the role of the throat for connectivity in shale.

Based on the controlling factors of methane adsorption in shale, a prediction model was introduced for adsorbed gas content at certain pressure and temperature. The model can help log analysts to quantify adsorbed gas from well-log data since TOC (total organic carbon) and V_{sh} (total clay content), which are the measure inputs of the introduced models, can be obtained from well-log data as well. The model showed a good prediction for Langmuir volume at experimental temperature (25°C). However, more data is required to improve the accuracy of the model for the Langmuir volume at reservoir temperature and Langmuir pressure.

Parts of this thesis have been published in the following journals and conference articles:

Zou, J. and Rezaee, R., 2016. Effect of particle size on high-pressure methane adsorption of coal. *Petroleum Research*, 1(1): 53-58.

Zou, J., Rezaee, R. and Liu, K., 2017. Effect of Temperature on Methane Adsorption in Shale Gas Reservoirs. *Energy & Fuels*, 31(11): 12081-12092.

Zou, J., Rezaee, R., Xie, Q., You, L., Liu, K. and Saeedi, A., 2018a. Investigation of moisture effect on methane adsorption capacity of shale samples. *Fuel*, 232: 323-332.

Zou, J., Rezaee, R. and Yuan, Y., 2018b. Investigation on the adsorption kinetics and diffusion of methane in shale samples. *Journal of Petroleum Science and Engineering*, 171: 951-958.

Zou, J. and Rezaee, R., 2019. A Prediction Model for Methane Adsorption Capacity in Shale Gas Reservoirs. *Energies*, 12(2): 280.

Table of Contents

ABSTRACT	iii
Table of Contents	vi
List of Figures	ix
List of Tables.....	xii
Nomenclature and Conversion Factors	xiii
Acknowledgements	xv
Chapter 1	1
1.1 Introduction	1
1.2 Thesis objectives	5
1.3 Structure of the thesis	5
References	6
Chapter 2	11
2.1 Introduction	11
2.2 Samples and sample preparations.....	11
2.2.1 Samples	11
2.2.2 Sample preparations	14
2.3 Methods	15
2.3.1 High-pressure methane adsorption analysis.....	15
2.3.2 Langmuir mode	18
2.3.3 Thermodynamic parameters.....	19
2.3.4 Adsorption rate analysis	20
2.3.5 Bidisperse diffusion model	20
2.3.6 Low-pressure nitrogen and carbon dioxide adsorption analysis	21
2.4 Determination of particle size used for sample preparation	22
2.4.1 Results	23
2.4.2 Discussion	26

References	28
Chapter 3	30
3.1 Introduction	30
3.2 Experimental results	30
3.2.1 Low-pressure adsorption analysis	30
3.2.2 High-pressure methane adsorption isotherms analysis	36
3.3 Discussion	41
3.3.1 The effect of temperature on methane adsorption.....	41
3.3.2 The effect of moisture on pore structure characteristics	43
3.3.3 The effect of moisture on methane adsorption characteristics.....	45
3.3.4 Methane adsorption characteristics at high temperature with moisture	49
3.3.5 The combined effect of moisture and high temperature on methane adsorption in shales	50
3.3.6 Thermodynamic parameters.....	53
3.3.7 Estimation of methane adsorption in shales with moisture at a high temperature.....	56
3.4 Conclusion.....	57
References	58
Chapter 4	61
4.1 Introduction	61
4.2 Experiment results	61
4.3 Discussion	61
4.3.1 Pressure effect on methane adsorption rate.....	61
4.3.2 Temperature effect on methane adsorption rate.....	62
4.3.3 Comparison of methane adsorption rate between samples	63
4.3.4 Diffusivity	64
4.4 Conclusion.....	70
References	71

Chapter 5	72
5.1 Introduction	72
5.2 Results	73
5.2.1 Model of Langmuir volume at experimental temperature	73
5.2.2 Model of Langmuir volume at reservoir temperature	78
5.2.3 Model of Langmuir pressure at experimental temperature and reservoir temperature.....	80
5.3 Discussion and conclusions.....	83
References	84
Chapter 6	87
6.1 Concluding remarks	87
6.2 Limitations.....	90
6.3 Recommendations and future research:.....	91
Appendix I.....	93
Appendix II	96

List of Figures

Figure 2.1 Location map showing the Canning and Perth basins of Western Australia (from DMP, 2014).....	12
Figure 2.2 Schematic diagram of adsorption apparatus: (a) experimental setup of the volumetric system for methane adsorption on shale samples. (1) analysis port valve; (2) vent valve; (3) degas port valve; (4) full vacuum valve; (5) manifold valve;(6) CH ₄ gas valve;(7) CO ₂ gas valve; (8) helium gas valve. (b) Sample tube consists of three parts: V _{xU} , the volume of the upper stem; V _{xL} , the volume of the lower stem; V _s , the volume of the sample cell.	16
Figure 2.3 Low-pressure N ₂ sorption/desorption isotherms of the studied samples at 77K: C45, C75, C250, and C1000 are sample names with particle size range in Table 2.5.....	23
Figure 2.4 Pore size distribution defined by incremental pore volume at the pore width range of 1-100nm.	25
Figure 2.5 Comparison of methane adsorption of samples with different particle size at 30°C. Points are the experimental results and lines are the Langmuir fitting results.	26
Figure 2.6 Cross section of a hypothetical particle (Rouquerol et al., 2014).....	27
Figure 3.1 Low-pressure N ₂ isotherms for the shale samples.	31
Figure 3.2 Low-pressure CO ₂ adsorption isotherms for the shale samples.	32
Figure 3.3 Pore size distribution defined by incremental pore volume within the width range of 0.4 to 100nm for the studied samples.	36
Figure 3.4 Methane adsorption capacity for the dry shale samples at different temperatures.	37
Figure 3.5 Comparison of methane adsorption isotherms for the dry shale samples at 25°C. Note that sample AC-2 has more adsorbed gas content than sample AC-4 at the first 3 pressure points.	37
Figure 3.6 Comparison of correlations between temperature and adsorbed methane under isobaric conditions. The points are the experimental results and the dotted curves are the linear regression fitting results.	38

Figure 3.7 Comparison of methane adsorption isotherms between dry and wet shale samples at different temperatures: the red and blue dots represent the dry and wet samples, respectively.....	39
Figure 3.8 Comparison of methane adsorption isotherms at 60°C for wet samples: sample AC-2, AC-5, and AC-5 have similar results.....	40
Figure 3.9 Comparison of correlations between adsorbed gas content and the decrease rate of methane adsorption with increasing temperature.	42
Figure 3.10 Comparison of adsorbed gas content normalized by TOC at 80°C for four shale samples. Samples AC-2 and AC-5 have larger adsorbed gas content normalized by TOC than samples AC-1 and AC-4.	43
Figure 3.11 Theoretical pore model for the thickness of adsorbed water, D and d are the pore diameter of at dry and wet conditions respectively; T is the thickness of adsorbed water, which can be defined as $(D-d)/2$; D-d represents the distance of the left shift in PSD.....	44
Figure 3.12 Micropore volume normalized to TOC for the dry samples.....	45
Figure 3.13 The reduced percentage of methane adsorption with moisture as a function of pressure for all shale samples. The solid line represents the general trend of the points.....	46
Figure 3.14 The reduction of methane adsorption with moisture as a function of pressure for all shale samples: $V_{\text{reduction}}=V_{\text{dry}}-V_{\text{wet}}$. The solid line represents the general trend of the points.....	46
Figure 3.15 Relation between the effect of moisture on methane adsorption and TOC for shale samples. The red line describes the correlation of $V_{\text{reduction}}/V_{\text{dry}}$ at maximum pressure (1015psi) to TOC, the blue line represents the correlation of $V_{L_{\text{reduction}}}/V_{L_{\text{dry}}}$ to TOC.	48
Figure 3.16 The correlation between the TOC and reduction of methane adsorption with moisture at maximum pressure.	49
Figure 3.17 Correlation of Langmuir volume for dry samples at 25°C and wet samples at 60°C to TOC.	50
Figure 3.18 The reduced percentage of methane adsorption with moisture as a function of pressure at different temperatures.....	51
Figure 3.19 The decrease rate of Langmuir volume with increasing temperature for the dry and wet samples.	52
Figure 3.20 The correlation between the heat of adsorption and the TOC.....	56

Figure 4.1 Methane adsorption rate at three pressure steps for the shale samples. The vertical axis is the fraction uptake and the horizontal axis is the square root of time ($s^{0.5}$).	62
Figure 4.2 Methane adsorption rate under 30bar at three different temperatures for sample AC-1 and AC-5.	63
Figure 4.3 The relation of methane adsorption rate to TOC and micropore volume. The adsorption rate at 50 bar shows a good correlation with TOC; a moderate correlation exists between the adsorption rate at 30 bar and the micropore volume.	64
Figure 4.4 The methane adsorption rate at 30bar fitted using the bidisperse diffusion model for the shale samples.	65
Figure 4.5 The relation of $Da'Ra2$ at 10bar to the TOC and micropore volume for the shale samples.	69
Figure 4.6 The relations of $Da'Ra2$ at 10 and 50bar to the sum of mesopore and macropore (<100nm) volume.	69
Figure 4.7 A hypothetical pore model in shale: micropore is not in fact a pore but it plays the role of the throat and contributes to the diffusion.	70
Figure 5.1 The relationship between the TOC and Langmuir volume at experimental temperature for the studied shale samples.	74
Figure 5.2 A weak relationship exists between the clay content and Langmuir volume at experimental temperature for the studied shale samples.	75
Figure 5.3 The relationship between the clay content and Langmuir volume at experimental temperature for low, medium and high TOC shale samples.	76
Figure 5.4 There is no meaningful relationship between the TOC-normalized Langmuir volume at experimental temperature and T_{max} for the studied shale samples.	77
Figure 5.5 The relationship between the measured and predicted Langmuir volume at experimental temperature.	78
Figure 5.6 The relationship between the TOC and decrease rate of Langmuir volume with increasing temperature.	80
Figure 5.7 The relationship between the Langmuir pressure and Langmuir volume at experimental temperature for the studied samples.	81
Figure 5.8 The relationship of the TOC to the fitting coefficient m .	82

List of Tables

Table 2.1 Composition of the studied shale samples from XRD.....	13
Table 2.2 Geochemical information for the studied shale samples from Rock-eval. 13	13
Table 2.3 Particle sizes used in high-pressure methane adsorption related studies. ..	22
Table 2.4 Petrographic composition of BM Alliance coal sample.	23
Table 2.5 Low pressure N ₂ sorption result of the studied samples	24
Table 2.6 Pore volume proportion of samples with different particle sizes.....	25
Table 2.7 Langmuir parameters of samples with different particle size	26
Table 3.1 Pore structure parameters derived from low-pressure nitrogen and carbon dioxide adsorption for the studied samples.....	33
Table 3.2 Langmuir parameters for the shale samples at different temperatures.	41
Table 3.3 Thermodynamic parameters of methane adsorption for the dry and wet shale samples.....	55
Table 3.4 Thermodynamic parameters of methane adsorption on different samples from published data.....	55
Table 3.5 Estimated methane adsorption capacity of shale samples under reservoir conditions.	57
Table 4.1 The slope of adsorption rate at three pressures for the shale samples.	64
Table 4.2 Gas diffusion parameters from the bidisperse model for the shale samples at 25°C.	67
Table 4.3 Gas diffusion parameters from bidisperse model for sample AC3-1 and AC3-5 at 45 and 60°C.....	68
Table 5.1 Considered factors of the prediction model for Langmuir parameters in previous studies.....	73

Nomenclature and Conversion Factors

n_{He}	Amount of helium dosed into the sample tube (mol)
n_{dosed}	Amount of methane dosed from manifold to sample tube (mol)
n_{Nads}	Amount of methane not adsorbed by the shale sample (mol)
n_{ads}	Excess amount of methane adsorbed on the shale sample (mol)
p_{s1}	Pressure of helium after dosing in the sample tube (bar)
p_s	Pressure of methane in sample tube (bar)
p_{mA}' , p_{mB}'	Pressure of methane before and after dosing in the manifold (bar)
p_{mA} , p_{mB}	Pressure of helium before and after dosing in the manifold (bar)
R	Gas constant, $8.3145JK^{-1} mol^{-1}$
T_{mA} , T_{mB}	Temperature of manifold before and after dosing (K)
T_{Am}	Ambient temperature in the lab (K)
T_{An}	Analysis temperature (K)
T_{mA}' , T_{mB}'	Temperature of methane before and after dosing in the manifold (bar)
T_s	Temperature of methane in the sample cell (K)
T_{xU}	Temperature of methane in the upper stem (K)
T_{xL}	Temperature of methane in the lower stem (K)
z_{mA}	Gas compressibility at p_{mA} and T_{mA}
z_{mB}	Gas compressibility at p_{mB} and T_{mB}
V_m	Manifold volume (cm ³)
V_{xU}	Volume of the upper stem (cm ³)
V_{xL}	Volume of the lower stem (cm ³)
V_s	Volume of the sample cell (cm ³)
V_{AmFS}	Total volume of free space at ambient temperature (cm ³)

z_{xU1}	Gas compressibility at p_{s1} and T_{mB}
z_{s1}	Gas compressibility at p_{s1} and T_{Am}
z_{xL}	Gas compressibility at p_{s1} and T_{Am}
z_{s2}	Gas compressibility at T_{An} and p_{s1}
z_{mA}'	Gas compressibility at p_{mA}' and T_{mA}'
z_{mB}'	Gas compressibility at p_{mB}' and T_{mB}'
z_s	Gas compressibility at T_s and p_s
z_{xU}	Gas compressibility at T_{xU} and p_s
z_{xL}	Gas compressibility at T_{xL} and p_s

Conversion factors

Pressure

MPa to PSIA	145.0377
-------------	----------

Adsorption

cm ³ /g to scf/ton	35.3125
mmol/g to scf/ton	791

Acknowledgements

In my younger years, I played video games a lot and was really good. When I received the offer of PhD four years ago I told myself, 'just a new game about real life and this part of life called PhD.' However, after more than three years study, I have understood that PhD means a great deal more than that.

First of all, I would like to express my most sincere appreciation to my supervisor Professor Reza Rezaee, without his enormous efforts and encouragement, I would not have completed this long journey. The discussions on my topic were full of enthusiasm and energy. More importantly, the serious attitude towards research I learned from him will inspire me to pursue a meaningful career.

For the funny experience and kind help I am grateful to my colleagues in our research group they are: Dr. Hongcai Wang and Nadia Testamanti who helped me a lot at the beginning of my lab work; Bob Webb, who supported me on the equipment; Lukman Johnson, Pooya Hadian, and Ms. Yujie Yuan, who helped me with data collection.

Special thanks also go to my co-supervisor Associate professor Ali Saeedi helped me with experiment setting up, kind staff in Department of petroleum engineering: Associate professor Mofazzal Hossain, Dr. Quan Xie and Ms. Nichole Sik.

Thanks also to the China scholarship council and State Key Laboratory of Oil and Gas Reservoir Geology and Exploitation (Southwest Petroleum University, China) for providing financial assistance for the research and Department of petroleum engineering and chemical engineering for providing the necessary facilities. I also acknowledge the Department of Mines, Industry Regulation and Safety for granting me to view and collect core samples from several boreholes of Canning Basin under Approval Nos. G32825 & N00413.

Last but not least, I would like to express my thanks to my girlfriend Ms. Fuping Li and my parents. Their emotional supports mean so much to me. Special thanks to my grandma passed away last year, I miss her so much.

Chapter 1

Introduction

1.1 Introduction

Methane adsorption in shale gas system has drawn much attention because of the significance of shale gas to mitigate the energy crisis of the world. With the development of the oil and gas industry and the increasing demand for energy, shale gas has been widely explored and developed all over the world. However, there are many uncertainties in the evaluation and development of shale gas due to the complicated adsorption properties of methane in the shale gas system. As reported, methane is stored as free gas and adsorbed gas in shale gas reservoirs. The percentage of adsorbed gas could be up to 85% in shale gas reservoir (Curtis, 2002). The adsorbed gas has also been reported to influence the gas flow and permeability, which are crucial to the field development plan (Guo et al., 2017). Therefore, understanding the theory of methane adsorption characteristics is required to reduce uncertainties in reservoir evaluation and design economical production strategies.

However, methane adsorption characteristics of shale gas reservoir are controlled by various factors. One of the most important controlling factors of methane adsorption in shales is nano-scale pore structure with large internal surface area (Ross and Bustin, 2009), which is characterized by many measurements. As pores in shale can be divided into three categories based on the IUPAC: micropores (<2nm), mesopores (2-50nm) and macropores (>50nm) (Rouquerol et al., 1994), various methods focusing on different pore size have been used to characterize pore structure of shale samples. Low-pressure CO₂ adsorption has been used for the characterization of micropores (Clarkson et al., 2013) and low-pressure N₂ adsorption for characterization of mesopores and macropores (2-100nm) (Labani et al., 2013). However, low-pressure adsorption has a maximum pore size limit of 300 nm (Scherdel et al., 2010). The mercury intrusion porosimetry (MIP) is an efficient and accurate method to determine the porosity of the rock, pore diameter, etc., but its application is limited to interconnected pores that range from 3.6 nm to 1 mm (Hinai et al., 2014; Mastalerz et

al., 2013). In addition, the nuclear magnetic resonance (NMR) is another indirect method to characterize pore size distribution, this method has been used to measure pore size distribution of tight sandstones and shale with high accuracy (Rezaee et al., 2012; Sigal, 2015; Wang et al., 2015). These techniques (MIP, LPA & NMR) can provide data of quantitative pore size distribution and reproducible porosity but no actual pore geometry. Direct approaches, such as field emission scanning electron microscopy/transmission electron microscopy (FE-SEM/TEM) (Loucks et al., 2009), focused ion beam scanning electron microscopy (FIB-SEM) (Curtis et al., 2012) and small angle neutron scattering (SANS) and ultra-small-angle neutron scattering (USANS) (Clarkson et al., 2012; Clarkson et al., 2013) have shown the geometry, size, and distributions of pores in shale. Data from these methods cannot be used to characterize the pore structure of the whole sample, because the scanned area is random and tiny (Liu et al., 2011). Three-dimensional X-ray (CT) imaging is another direct approach used in the numerical reconstruction of 3D pore texture, which can be applied at the microscale to the nanoscale.

As speculation still exists in the characterization of pore structure in shales, the effect of pore structure on methane adsorption capacity is unclear. Moreover, it is hard to isolate the influence of pore structure from the various controlling factors on methane adsorption capacity in shales by experiment method. Grand Canonical Monte Carlo (GCMC) simulation has been employed on methane adsorption in shale or coal system. Characteristics of methane adsorption isotherms have been studied using GCMC simulation on pores with ranged sizes, demonstrating that smaller pores exhibit larger excess density comparing to bigger pores (Mosher et al., 2013). Apart from the pore size, it is worth considering the effect of pore geometry on methane adsorption capacity in shales. Because the pore geometry controls the configuration of methane adsorption in a confined pore space, which results from the greater contribution of gas-solid interactions compared to gas-gas interactions (Liu et al., 2012).

Organic matter and inorganic matter in shale both can adsorb methane and control the pore structure (Yang et al., 2015). Total organic carbon (TOC) shows a positive linear correlation with methane adsorption capacity in shale gas system (Dang et al., 2017a; Ross and Bustin, 2009). The maturity of organic matter is also regarded as the controlling factor of methane adsorption capacity. TOC-normalized adsorption capacity was observed to increase with the increasing thermal maturity up to some

critical value and followed by a reversed trend at high maturity (Gasparik et al., 2014). Two reasons based on the previous reports can be used to explain this trend. One reason is that micropores are generated with thermal maturation, which offers more pore volume for methane adsorption (Ross and Bustin, 2009). Another reason is the changes in the surface chemistry of kerogen with thermal maturation: affinity between methane and kerogen increases with maturity because of increasing aromaticity (Zhang et al., 2012). In addition to the maturity and TOC, kerogen type was also reported to have an effect on methane adsorption capacity. The methane adsorption capacity of individual kerogen types follows the order: type III > type II > type I. Apart from the organic matter, for the clay-rich shales, the inorganic matter can also influence the total methane adsorption capacity (Fan et al., 2015). For pure clay minerals, the methane adsorption capacity was reported to decrease in the order: smectite > mixture of illite and smectite > kaolinite > chlorite > illite (Ji et al., 2012).

External parameters such as pressure, temperature and moisture can affect the methane adsorption capacity in shales as well. Moisture can reduce the methane adsorption capacity greatly by occupying sorption sites in shale gas reservoirs (Chalmers and Bustin, 2010). Studies related to the effect of moisture on methane adsorption have been conducted on coal, clay and shale samples using both experiment and simulation methods (Krooss et al., 2002; Zhao et al., 2017). A Monte Carlo simulation study on clay minerals has claimed that water molecules cover the clay surfaces by forming a water film (Jin and Firoozabadi, 2014). A combined experiment and simulation study on shale has shown that moisture in actual condition could exist as capillary water in pores and water film bounded on pore surface (Li et al., 2016). The capillary water blocks available adsorption sites and the water film changes the interaction between methane and clay. Another experiment study on low TOC shales demonstrated that moisture influences macropores most and micropores least, and methane adsorption capacity reduces significantly (Wang and Yu, 2016). However, micropores are believed to be more important than macropores in methane adsorption in shales. Besides, the methane adsorption capacity of shale decreases with increasing moisture content until a critical moisture content reached (Gasparik et al., 2014). By contrast, another study showed that no correlation exists between moisture content and methane adsorption capacity (Chalmers and Bustin, 2008). Although the effect of moisture on methane adsorption in shale gas reservoirs is well documented by experiment and

simulation studies, a question about how moisture reduces the methane adsorption capacity is still not well-understood. Especially, how moisture changes the pore structure characteristics of micropores and its related impact on methane adsorption are unclear.

Methane adsorption in shales is an exothermic process and, methane adsorption capacity reduces at the high temperature. Many methane adsorption studies at ranged temperature have shown that methane adsorption isotherms vary significantly at different temperatures (Guo, 2013; Ji et al., 2015). Adsorbed methane content decreases with rising temperature and the change of adsorbed gas content with increasing temperature is greater at higher pressure. Up to date, however, the study of the effect of temperature on methane adsorption of low TOC shale samples has rarely been mentioned and is still limited.

In addition, the contribution of adsorbed gas to gas transport in shale is a very important subject. Mechanisms of the gas transport related to the adsorbed gas include the gas adsorption, desorption, diffusion and Darcy flow. Given that a large proportion of pores in shale are nano-scale (Kuila et al., 2014; Labani et al., 2013), the gas flow in nano-scale pores is mainly limited by the gas diffusion rather than the Darcy flow in big pores or fractures. Therefore, adsorption kinetics from methane adsorption experiments describe the process of gas diffusion in pore throats and gas adsorption on pore surfaces. Some scholars have realized the importance of gas adsorption kinetics in coal and shale. Methane adsorption rate data has been analyzed for shale samples, showing a negative relationship between the adsorption rate and pressure (Dang et al., 2017). The diffusion behavior in porous material can be indirectly obtained from adsorption kinetics using diffusion models, such as the “unipore diffusion model” and the “bidisperse diffusion model”. Even though the unipore diffusion model has been successfully used for high-rank coals (Clarkson and Bustin, 1999), it is inadequate for shale with heterogeneous pore structures and would overrate the diffusivity (Dang et al., 2017; Yuan et al., 2014). This is because the unipore model assumes that the pore structure is homogenous. Unlike the unipore model, the bidisperse diffusion model was developed for small and large pores in the matrix, named as micropore and macropore, respectively (Ruckenstein et al., 1971). Note that the macropore and micropore in the bidisperse model represent pores with different sizes but not any specific sizes. The assumption of the bidisperse model is linear

isotherm. The methane adsorption isotherm of low pressure (<4MPa) was observed as linear in shale, and the adsorption rate of low pressure (<4MPa) were well fitted by the bidisperse model in previous work (Yuan et al., 2014). The fitting results have shown that macropore diffusivity decreases with increasing pressure, and both macropore and micropore diffusivity are reduced by water. Although some scholars have analyzed the gas adsorption rate and applied different diffusion models in shale (Chen et al., 2018; Dang et al., 2017b; Rani et al., 2018), the behavior of gas adsorption kinetics and diffusion in different shale samples are unclear.

1.2 Thesis objectives

This study attempted to investigate the methane adsorption capacity in shale gas system through laboratory measurements. The objectives of this study are to:

- Quantitatively describe the effect of temperature on methane adsorption capacity in shale gas system.
- Investigate the mechanism of moisture controlling methane adsorption in shales.
- Examine the combined effect of moisture and high temperature on methane adsorption capacity in shales.
- Characterize adsorption kinetics and diffusion of methane in shale.
- Establish a prediction model for methane adsorption capacity in shales.

1.3 Structure of the thesis

According to the above objectives, the content of each chapter in this study is explained briefly as follows:

Chapter 2 shows the geochemical and mineralogical information of the employed shale samples in this study. This chapter also addresses the experimental setups, procedures, and conditions for low-pressure adsorption and high-pressure methane adsorption experiments. Sample preparations are designed based on research purposes. The models to fit methane adsorption isotherms and adsorption kinetics are provided, which could determine the Langmuir parameters, thermal dynamic parameters, and effective diffusivities. In addition, the analytical particle size of sample powders used in this study is discussed.

Chapter 3 evaluates the effect of temperature and moisture and their combined effect on methane adsorption capacity in shales. A series of low-pressure and high-pressure

adsorption experiments were conducted on dry and moisturized samples at different temperatures. Methane adsorption isotherms were fitted by the Langmuir model to obtain Langmuir parameters. The results can provide a better understanding of the temperature and moisture controlling methane adsorption capacity in shales.

Chapter 4 characterizes methane adsorption kinetics and diffusivity in shales. Methane adsorption rate was measured by experiment and fitted by bidisperse diffusion model. The methane adsorption rate and diffusivity are discussed on various shale samples. It will be followed by a proposed pore model to explain the roles of different pores in the diffusion of shale.

Chapter 5 examines the effect of organic matter richness, clay content, and thermal maturity on the methane adsorption capacity of shale samples published in references and measured in our lab. The relationship between the Langmuir parameters and their controlling factors are quantitatively characterized. A prediction model for methane adsorption capacity in shales is built.

References

- Chalmers, G.R. and Bustin, M.R., 2010. PS The Effects and Distribution of Moisture in Gas Shale Reservoir Systems.
- Chalmers, G.R.L. and Bustin, R.M., 2008. Lower Cretaceous gas shales in northeastern British Columbia, Part I: geological controls on methane sorption capacity. *Bulletin of Canadian Petroleum Geology*, 56(1): 1-21.
- Chen, M., Kang, Y., Zhang, T., You, L., Li, X., Chen, Z., Wu, K. and Yang, B., 2018. Methane diffusion in shales with multiple pore sizes at supercritical conditions. *Chemical Engineering Journal*, 334: 1455-1465.
- Clarkson, C.R. and Bustin, R.M., 1999. The effect of pore structure and gas pressure upon the transport properties of coal: a laboratory and modeling study. 1. Isotherms and pore volume distributions. *Fuel*, 78(11): 1333-1344.
- Clarkson, C.R., Freeman, M., He, L., Agamalian, M., Melnichenko, Y.B., Mastalerz, M., Bustin, R.M., Radliński, A.P. and Blach, T.P., 2012. Characterization of tight gas reservoir pore structure using USANS/SANS and gas adsorption analysis. *Fuel*, 95: 371-385.

- Clarkson, C.R., Solano, N., Bustin, R.M., Bustin, A.M.M., Chalmers, G.R.L., He, L., Melnichenko, Y.B., Radliński, A.P. and Blach, T.P., 2013. Pore structure characterization of North American shale gas reservoirs using USANS/SANS, gas adsorption, and mercury intrusion. *Fuel*, 103: 606-616.
- Curtis, J.B., 2002. Fractured Shale-Gas Systems. *AAPG Bulletin*, 86(11): 1921-1938.
- Curtis, M.E., Sondergeld, C.H., Ambrose, R.J. and Rai, C.S., 2012. Microstructural investigation of gas shales in two and three dimensions using nanometer-scale resolution imaging. *AAPG Bulletin*, 96: 13.
- Dang, W., Zhang, J., Wei, X., Tang, X., Chen, Q., Li, Z., Zhang, M. and Liu, J., 2017. Geological controls on methane adsorption capacity of Lower Permian transitional black shales in the Southern North China Basin, Central China: Experimental results and geological implications. *Journal of Petroleum Science and Engineering*, 152: 456-470.
- Dang, W., Zhang, J., Wei, X., Tang, X., Wang, C., Chen, Q. and Lei, Y., 2017. Methane Adsorption Rate and Diffusion Characteristics in Marine Shale Samples from Yangtze Platform, South China. *Energies*, 10(5): 626.
- Fan, E., Shuheng Tang, Chenglong Zhang, Qiulei Guo and Sun, C., 2015 Methane sorption capacity of organics and clays in high-over matured shale-gas systems. *Energy, Exploration & Exploitation*, 32: 16.
- Gasparik, M., Bertier, P., Gensterblum, Y., Ghanizadeh, A., Krooss, B.M. and Littke, R., 2014. Geological controls on the methane storage capacity in organic-rich shales. *International Journal of Coal Geology*, 123: 34-51.
- Guo, S., 2013. Experimental study on isothermal adsorption of methane gas on three shale samples from Upper Paleozoic strata of the Ordos Basin. *Journal of Petroleum Science and Engineering*, 110: 132-138.
- Guo, W., Hu, Z., Zhang, X., Yu, R. and Wang, L., 2017. Shale gas adsorption and desorption characteristics and its effects on shale permeability. *Energy Exploration & Exploitation*: 0144598716684306.
- Hinai, A.A., Rezaee, R., Esteban, L. and Labani, M., 2014. Comparisons of pore size distribution: A case from the Western Australian gas shale formations. *Journal of Unconventional Oil and Gas Resources*, 8: 1-13.
- Ji, L., Zhang, T., Milliken, K.L., Qu, J. and Zhang, X., 2012. Experimental investigation of main controls to methane adsorption in clay-rich rocks. *Applied Geochemistry*, 27(12): 2533-2545.

- Ji, W., Song, Y., Jiang, Z., Chen, L., Li, Z., Yang, X. and Meng, M., 2015. Estimation of marine shale methane adsorption capacity based on experimental investigations of Lower Silurian Longmaxi formation in the Upper Yangtze Platform, south China. *Marine and Petroleum Geology*, 68, Part A: 94-106.
- Jin, Z. and Firoozabadi, A., 2014. Effect of water on methane and carbon dioxide sorption in clay minerals by Monte Carlo simulations. *Fluid Phase Equilibria*, 382: 10-20.
- Krooss, B.M., van Bergen, F., Gensterblum, Y., Siemons, N., Pagnier, H.J.M. and David, P., 2002. High-pressure methane and carbon dioxide adsorption on dry and moisture-equilibrated Pennsylvanian coals. *International Journal of Coal Geology*, 51(2): 69-92.
- Kuila, U., McCarty, D.K., Derkowski, A., Fischer, T.B., Topór, T. and Prasad, M., 2014. Nano-scale texture and porosity of organic matter and clay minerals in organic-rich mudrocks. *Fuel*, 135(Supplement C): 359-373.
- Labani, M.M., Rezaee, R., Saeedi, A. and Hinai, A.A., 2013. Evaluation of pore size spectrum of gas shale reservoirs using low pressure nitrogen adsorption, gas expansion and mercury porosimetry: A case study from the Perth and Canning Basins, Western Australia. *Journal of Petroleum Science and Engineering*, 112: 7-16.
- Li, J., Li, X., Wang, X., Li, Y., Wu, K., Shi, J., Yang, L., Feng, D., Zhang, T. and Yu, P., 2016. Water distribution characteristic and effect on methane adsorption capacity in shale clay. *International Journal of Coal Geology*, 159: 135-154.
- Liu, C., Shi, B., Zhou, J. and Tang, C., 2011. Quantification and characterization of microporosity by image processing, geometric measurement and statistical methods: Application on SEM images of clay materials. *Applied Clay Science*, 54(1): 97-106.
- Liu, Z., Horikawa, T., Do, D.D. and Nicholson, D., 2012. Packing effects on argon and methanol adsorption inside graphitic cylindrical and slit pores: A GCMC simulation study. *Journal of Colloid and Interface Science*, 368(1): 474-487.
- Loucks, R.G., Reed, R.M., Ruppel, S.C. and Jarvie, D.M., 2009. Morphology, Genesis, and Distribution of Nanometer-Scale Pores in Siliceous Mudstones of the Mississippian Barnett Shale. *Journal of Sedimentary Research* 79: 14.
- Mastalerz, M., Schimmelmanna, A., Drobnia, A. and Chen, Y., 2013. Porosity of Devonian and Mississippian New Albany Shale across a maturation gradient:

- Insights from organic petrology, gas adsorption, and mercury intrusion. *AAPG Bulletin*, 97: 23.
- Mosher, K., He, J., Liu, Y., Rupp, E. and Wilcox, J., 2013. Molecular simulation of methane adsorption in micro- and mesoporous carbons with applications to coal and gas shale systems. *International Journal of Coal Geology*, 109–110: 36-44.
- Rani, S., Prusty, B.K. and Pal, S.K., 2018. Adsorption kinetics and diffusion modeling of CH₄ and CO₂ in Indian shales. *Fuel*, 216: 61-70.
- Rezaee, R., Saeedi, A. and Clennell, B., 2012. Tight gas sands permeability estimation from mercury injection capillary pressure and nuclear magnetic resonance data. *Journal of Petroleum Science and Engineering*, 88–89: 92-99.
- Ross, D.J.K. and Bustin, R.M., 2009. The importance of shale composition and pore structure upon gas storage potential of shale gas reservoirs. *Marine and Petroleum Geology*, 26(6): 916-927.
- Rouquerol, J., Avnir, D., Fairbridge, C.W., Everett, D.H., Haynes, J.M., Pernicone, N., Ramsay, J.D.F., Sing, K.S.W. and Unger, K.K., 1994. Recommendations for the characterization of porous solids (Technical Report), *Pure and Applied Chemistry*, pp. 1739.
- Ruckenstein, E., Vaidyanathan, A.S. and Youngquist, G.R., 1971. Sorption by solids with bidisperse pore structures. *Chemical Engineering Science*, 26(9): 1305-1318.
- Scherdel, C., Reichenauer, G. and Wiener, M., 2010. Relationship between pore volumes and surface areas derived from the evaluation of N₂-sorption data by DR-, BET- and t-plot. *Microporous and Mesoporous Materials*, 132(3): 572-575.
- Sigal, R.F., 2015. Pore-Size Distributions for Organic-Shale-Reservoir Rocks From Nuclear-Magnetic-Resonance Spectra Combined With Adsorption Measurements. *SPE Journal*.
- Wang, H., Rezaee, R. and Saeedi, A., 2015. Evaporation Process and Pore Size Distribution in Tight Sandstones: A Study Using NMR and MICP. *Procedia Earth and Planetary Science*, 15: 767-773.
- Wang, L. and Yu, Q., 2016. The effect of moisture on the methane adsorption capacity of shales: A study case in the eastern Qaidam Basin in China. *Journal of Hydrology*, 542: 487-505.

- Yang, F., Ning, Z., Zhang, R., Zhao, H. and Krooss, B.M., 2015. Investigations on the methane sorption capacity of marine shales from Sichuan Basin, China. *International Journal of Coal Geology*, 146: 104-117.
- Yuan, W., Pan, Z., Li, X., Yang, Y., Zhao, C., Connell, L.D., Li, S. and He, J., 2014. Experimental study and modelling of methane adsorption and diffusion in shale. *Fuel*, 117: 509-519.
- Zhang, T., Ellis, G.S., Ruppel, S.C., Milliken, K. and Yang, R., 2012. Effect of organic-matter type and thermal maturity on methane adsorption in shale-gas systems. *Organic Geochemistry*, 47: 120-131.
- Zhao, T., Li, X., Zhao, H. and Li, M., 2017. Molecular simulation of adsorption and thermodynamic properties on type II kerogen: Influence of maturity and moisture content. *Fuel*, 190: 198-207.

Chapter 2

Methods and materials

2.1 Introduction

The quantification of gas storage in shale is challenging due to its heterogeneous pore structure and complex composition. To evaluate methane adsorption capacity under reservoir conditions in shale gas system, one reliable and popular research method is high-pressure methane adsorption experiment. The high-pressure methane adsorption experiment can provide the adsorbed gas content as a function of pressure at constant temperature, which is defined as gas adsorption isotherm. Prior to the high-pressure adsorption experiment, the shale samples must be well prepared. The first step of sample preparation is to crush the samples to particular particle size, as the rock sample takes too long to reach the adsorption equilibrium (Chen et al., 2015). The second step is to dry the shale samples at high temperature to remove the residual moisture or volatile. Methane adsorption isotherms are fitted by the Langmuir model to calculate the Langmuir parameters and thermal dynamic parameters, which are important to characterize methane adsorption capacity of shale samples. Adsorption kinetics are fitted by the bidisperse diffusion model to determine effective diffusivities. In addition, low-pressure CO₂ and N₂ adsorption were conducted as well to characterize the pore structure of shale samples.

This chapter presents a detailed description of the compositional information of the studied shale samples, sample preparations, experiments and fitting models.

2.2 Samples and sample preparations

2.2.1 Samples

A total of 15 shale samples were analyzed in this experimental study, 10 samples from the Ordovician Goldwyer Formation of the Canning Basin and 5 samples from the Permian Carynginia Formation of the Perth Basin. Tables 2.1 and 2.2 show the mineralogical composition and geochemical analysis, respectively. T_{\max} of the Canning Basin samples varies between 441 and 458°C, which is lower than that of the

samples in the Perth Basin (458 to 465°C). Clay mineral content of the studied samples ranges from 27.9 to 83.5%. Generally, the Canning Basin samples are more argillaceous than the Perth Basin samples.

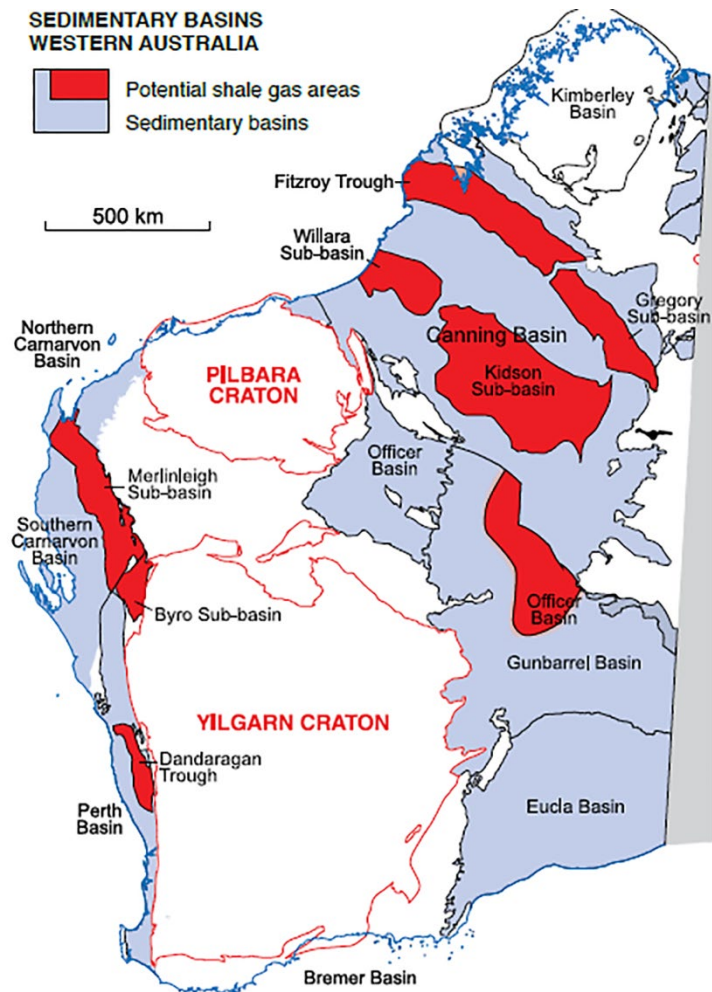


Figure 2.1 Location map showing the Canning and Perth basins of Western Australia (from DMP, 2014).

Table 2.1 Composition of the studied shale samples from XRD.

Basin	Sample	Depth (m)	Quartz (%)	Kaolinite (%)	Illite/Mica (%)	Chlorite (%)	Total Clay (%)	Other minerals (%)
Perth Basin	AC-1	2780	24.5	2.6	46.4	7.1	56	19.5
	AC-2	2794	53	0.8	27.2	3.1	31.1	15.9
	AC-3	2806	41.3	0.8	34.7	5.2	40.7	18
	AC-4	2812	53.8	0.5	24.5	2.9	27.9	18.3
	AC-5	2831	44.5	1.2	27.6	4.3	33.1	22.4
Canning Basin	T-1	1201	15.7	1.5	71.1	3.9	76.6	7.7
	T-2	1371	N/A	N/A	N/A	N/A	N/A	N/A
	T-3	1390	12.4	1.5	67.5	14.5	83.5	4.1
	T-4	1473	17.4	7.1	61.3	5.9	74.3	8.3
	T-5	1478	20.1	1.3	56.2	10.1	67.5	12.4
	T-6	1506	16.2	1.6	44.6	8.7	54.9	28.9
	T-7	1516	17.3	2.3	48.3	3.6	54.2	28.5
	T-8	1521	27.1	1.4	32.0	3.7	37.1	35.8
	T-9	1529	16.5	2.2	49.2	4.5	56.0	27.5
	T-10	1531	12.9	2.0	61.2	5.2	68.4	18.6

N/A: not available.

Table 2.2 Geochemical information for the studied shale samples from Rock-eval.

Basin	Sample	TOC (wt %)	S ₁ (mg/g)	S ₂ (mg/g)	S ₃ (mg/g)	HI	OI	PI	T _{max} °C
Perth Basin	AC-1	3.03	0.54	1.95	0.16	64	5	0.22	459
	AC-2	0.64	0.13	0.25	0.17	39	27	0.34	458
	AC-3	1.82	0.33	1.15	0.03	63	2	0.22	460
	AC-4	1.08	0.19	0.52	0.09	48	8	0.27	465
	AC-5	0.23	0.04	0.1	0.19	43	83	0.29	N/A
Canning Basin	T-1	0.28	0.04	1.1	0.49	393	175	0.03	442
	T-2	0.52	0.22	0.9	0.42	173	81	0.2	453
	T-3	1.26	0.63	2.43	0.28	193	22	0.21	454
	T-4	3.2	2.12	7.55	0.51	236	16	0.22	454
	T-5	3.1	1.57	4.66	0.43	165	15	0.25	456
	T-6	2.6	1.78	5.62	0.57	216	22	0.24	453
	T-7	1.53	1.74	3.41	0.35	223	23	0.34	441
	T-8	1.24	1.43	3.23	0.4	260	32	0.31	453
	T-9	2.76	2.33	5.83	0.49	211	18	0.29	448
	T-10	0.75	0.51	0.85	0.41	113	55	0.37	458

HI, the hydrogen index; OI, the oxygen index; PI, the production index.

To construct a prediction model for methane adsorption capacity in shales (Chapter 5), we also analyzed some high-pressure methane adsorption data from literature. As the high-pressure methane adsorption experiments are intrinsically controlled by various

factors (Gasparik et al., 2014), all the considered data must be obtained under similar experimental conditions (e.g., dry with the particle size of $<250\ \mu\text{m}$) with available compositional and geochemical information. It is worth mentioning that data of wet shale samples were not employed because the moisturization level is not constant and the number of shale samples in wet condition is constrained. Meanwhile, the 60 mesh ($<250\ \mu\text{m}$) was used in this study, as it has been widely used in the related studies. Under these conditions, a total of 66 samples from 6 Basins in China and Western Australia were studied (Guo et al., 2017; Ji et al., 2015; Ji et al., 2014; Wang et al., 2016). The samples have a TOC range of 0.23 to 28.48 wt% and clay content range of 20.1 to 83.5%. Thermal maturity of the samples was measured by rock-eval in T_{max} , ranges from 424 to 589 °C. Vitrinite Reflectance (R_o) is not used for the thermal maturity, because the convention from T_{max} to R_o is not constant for different basins. The wide ranges of compositional and geochemical parameters indicate good representativeness of the studied shale samples. The detailed information about the studied samples is provided in an appendix at the end of the thesis.

2.2.2 Sample preparations

All the studied shale samples were crushed to powders below $250\ \mu\text{m}$. After at least 8 hours degassing (110°C) to remove moisture and volatile, about 5 and 0.5 grams of samples were used for high-pressure methane adsorption and low-pressure nitrogen and carbon dioxide adsorption tests, respectively. Procedures of samples preparations are designed differently for dry and wet samples.

After crushing, all the samples were dried under vacuum at 110°C for 8 hours to remove residual moisture completely, which may alter some clays texturally and chemically. Before loading the sample into the sample cell of the low-pressure/high-pressure adsorption measurements, all the samples were degassed to remove volatile compounds. For the dry samples, the typical degassing temperature of 110°C was used, which is consistent with the drying temperature.

To prepare wet samples, around 10 grams of each dried sample was moisturized in an atmosphere of the saturated solution (KCl) at 25°C for 72 hours, which provides a consistent relative humidity (RH) of 84% (Greenspan, 1977). Even though only one moisturization level was conducted, it still can offer informative comparisons between

dry and wet samples on adsorption measurements. Besides, it has been observed that methane adsorption in shale decreases with increasing RH and no change exists between 75 and 97% RH. Thus, the 84% RH we chose in this study can influence the methane adsorption in shales strikingly. For moisturized samples, 40°C is used as the degassing temperature to remove free and condensed water but not high enough for clay-bound water under near vacuum condition. It is inevitable that water desorbs during degassing. Thus, we compared the weight of samples before and after 8 hours degassing. The percentage of reduced weight after degassing for both dry and moisturized samples ranges from 4 to 6%, which indicates that the loss of bound water during degassing is very limited for wet samples. Therefore, the moisture content studied in this study is the adsorbed water excluding the condensed water and free water. Besides, even though the degassing temperature is 110°C for dry samples and 40°C for wet samples, the different adsorption results between the dry and wet samples cannot attribute to the different degassing temperature as all samples were initially dried at 110°C.

2.3 Methods

2.3.1 High-pressure methane adsorption analysis

High-pressure up to 7MPa (1015psi) methane adsorption was measured on shale samples using Micromeritics high-pressure volumetric analyzer (HPVAII-200) (Figure 2.1). The experimental setup basically consists of a vacuum pump, an outgassing furnace with a temperature controller, a sample cell, a sample chamber, a thermostat and a reference cell connected to two pressure transducers (high-pressure transducer and low-pressure transducer). All valves are controlled by software on the connected computer. The experimental temperature is controlled by the thermostat connected to the sample chamber, which holds the sample cell. The thermostat was filled with water due to the expected experimental temperature less than 100°C. The sample cell is put inside the sample chamber. The temperature in the sample chamber is measured by a temperature probe and recorded by the software of the instrument. The pressure is measured by a pressure transducer with an accuracy $\pm 0.04\%$ and stability $\pm 0.1\%$.

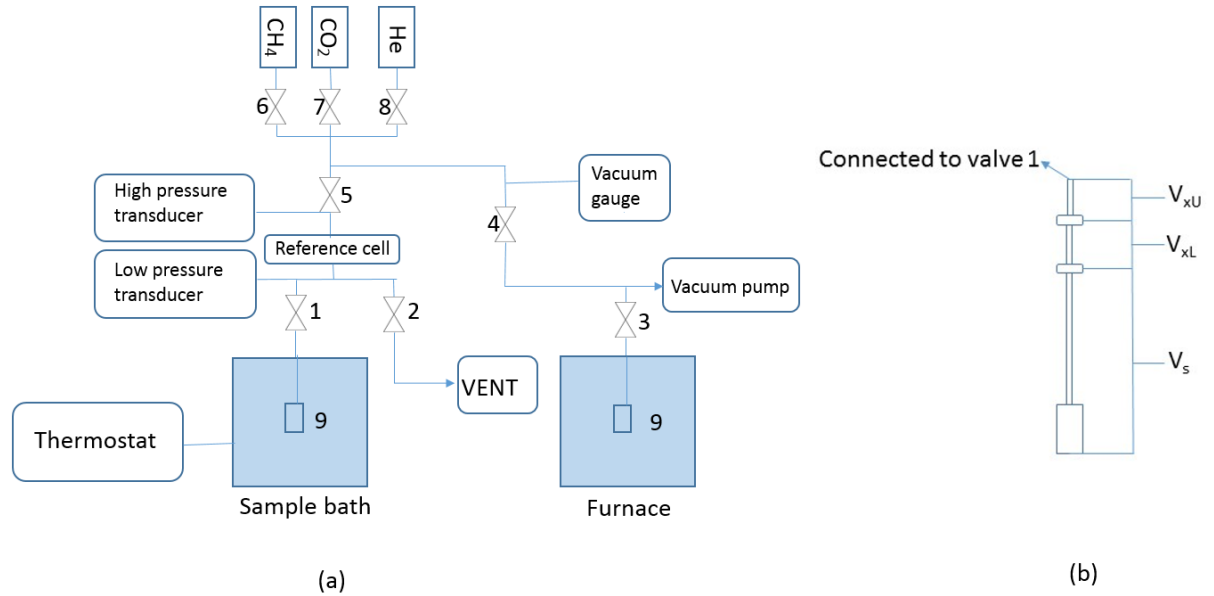


Figure 2.2 Schematic diagram of adsorption apparatus: (a) experimental setup of the volumetric system for methane adsorption on shale samples. (1) analysis port valve; (2) vent valve; (3) degas port valve; (4) full vacuum valve; (5) manifold valve; (6) CH₄ gas valve; (7) CO₂ gas valve; (8) helium gas valve. (b) Sample tube consists of three parts: V_{xU} , the volume of the upper stem; V_{xL} , the volume of the lower stem; V_s , the volume of the sample cell.

The procedures of adsorption measurement for each sample at different temperatures were as follows:

- (1) Degassing the sample in the furnace for more than 12 hours. After the sample had cooled down to the ambient temperature, the sample cell was attached to the sample tube and then connected to valve 1. A 60-micron filter gasket was used between the sample cell and tube to prevent sample particles from entering the tube.
- (2) Purging the system. After attaching the sample cell to valve 1, helium was dosed to the reference cell and sample cell until the pressure increased to 15bars (217.6psi). Then helium vented out with decreasing pressure to around 1bar (14.5psi). This step was repeated three times to purge the system. Finally, the system was vacuumed by a pump.
- (3) Measuring the void volume at ambient temperature using helium expansion. It is assumed that helium is not adsorbed on the sample, so the helium volume dosed into the sample tube is regarded as the volume of free space. Up to 10bars (145.0psi) of helium was dosed to reference cell. As soon as the determined equilibrium criteria was met (pressure variation less than 0.001 bars in one minute or waiting for 15 minutes after dosing the gas into the reference cell), helium was dosed into

sample cell. In this process, pressure and temperature before and after helium dosed from a gas cylinder to the manifold are recorded. With compressibility factors at each temperature and pressure, the amount of helium dosed to the sample tube was determined with compressibility factors at each temperature and pressure using Equation 2.1. Herein, compressibility factors were provided by the software of HPVA, which are calculated from multiple equations of state using NIST REFROP.

$$n_{He} = \frac{p_{mA}V_m}{T_{mA}z_{mA}R} - \frac{p_{mB}V_m}{T_{mB}z_{mB}R} \quad \text{Equation 2.1}$$

As shown in Figure 2.1b, the sample cell volume has three different temperature zones: V_{xL} , V_{xU} and V_s . The Upper stem and manifold have the same temperature, which is recorded by the software. Lower stem and sample cell are connected with the same pressure and temperature. The measuring temperature is used for lower stem and sample cell for helium expansion. Therefore, the total volume of free space at ambient temperature was determined in Equations 2.2 and 2.3.

$$n_{He} = \frac{p_{s1}V_{xU}}{T_{mB}z_{xU1}R} + \frac{p_{s1}(V_{xL} + V_s)}{T_{Am}z_{s1}R} \quad \text{Equation 2.2}$$

$$V_{AmFS} = V_{xU} + V_{xL} + V_s \quad \text{Equation 2.3}$$

The upper stem is in the temperature controlled region of the manifold. This volume is about 7cm³ and temperature is measured by a resistance temperature detectors.

(4) Measuring void volume in the sample cell at analysis temperature. After increasing temperature in the sample cell using the connected thermostat, the volume of free space at analysis temperature in sample cell was determined using Equation 2.4. It is worth mentioning that ambient temperature was used for the lower stem in this step. The temperature gradient between the analysis temperature in the sample chamber and the exposed lower stem at ambient temperature was averaged out in the free space measurement.

$$n_{He} = \frac{p_{s1}V_{xU}}{T_{mB}z_{xU1}R} + \frac{p_{s1}V_{xL}}{T_{Am}z_{xL}R} + \frac{p_{s1}V_s}{T_{An}z_{s2}R} \quad \text{Equation 2.4}$$

(5) Measuring adsorbed amount of methane at expected pressure points. The equipment system was evacuated first after helium expansion. Then the methane was dosed to manifold from the gas cylinder which provides 99.999% purity methane. Once the equilibrium criteria (pressure variation less than 0.001 bars in one minute or waiting for 15 minutes after dosing the gas into the reference cell) was reached, methane was dosed to the sample tube and cell. The next pressure step was not started until the equilibrium criteria for methane adsorption in the sample cell was reached. This step was repeated to the maximum pressure as expected. In this process, data logging interval of pressure and temperature in the sample cell was 2 mins or 0.005 bars. The temperature of the lower stem was measured as well for the calculation of adsorbed gas content. Given the amount of methane dosed from the manifold, the amount of methane adsorbed was calculated using Equations 2.5, 2.6 and 2.7.

$$n_{dosed} = \frac{P_{mA} V_m}{T_{mA} z_{mA} R} - \frac{P_{mB} V_m}{T_{mB} z_{mB} R} \quad \text{Equation 2.5}$$

$$n_{Nads} = \frac{p_s V_s}{T_s z_s R} + \frac{p_s V_{xU}}{T_{xU} z_{xU} R} + \frac{p_s V_{xL}}{T_{xL} z_{xL} R} \quad \text{Equation 2.6}$$

$$n_{ads} = n_{dosed} - n_{Nads} \quad \text{Equation 2.7}$$

2.3.2 Langmuir mode

Gas adsorption is usually described by isotherm, which is the amount of adsorbed gas as a function of pressure at constant temperature. As for methane adsorption on shale, Langmuir equation has been used to fit experimental results due to its simplicity and accuracy. It is worth mentioning that the used Langmuir equation does not imply that the Langmuir theory is justified.

According to the Langmuir equation, the amount of adsorbed methane can be expressed using Equation 2.8.

$$V_{ads.} = \frac{V_L P}{P + P_L} \quad \text{Equation 2.8}$$

Where V_L is the Langmuir volume, defined as the maximum amount of gas that can be adsorbed on shale at an infinite pressure; P_L is the Langmuir pressure, defined as

the pressure at which one-half of the Langmuir volume can be adsorbed, P is the experimental pressure.

Langmuir volume and Langmuir pressure were determined using the rearranged Langmuir Equation 2.9.

$$\frac{P}{V_{ads.}} = \frac{P}{V_L} + \frac{P_L}{V_L} \quad \text{Equation 2.9}$$

Given that experimental pressure is recorded and the amount of adsorbed methane is measured, a plot of $\frac{P}{V_{ads.}}$ versus P is provided as a fitted line. The slope is $\frac{1}{V_L}$, and the

intercept is $\frac{P_L}{V_L}$. Langmuir volume is used to describe the maximum adsorbed gas volume at infinite pressure. Langmuir pressure describes the affinity between adsorbate and adsorbent.

It is worth mentioning that the Langmuir function is an absolute adsorption model while in high-pressure adsorption the excess character of the measurable adsorption process becomes more and more relevant. However, the Langmuir model is still meaningful in this work for relatively low maximum experimental pressure (7MPa).

2.3.3 Thermodynamic parameters

The reciprocal of Langmuir pressure is Langmuir constant (K), which is a function of temperature and adsorption thermodynamic parameters as shown in Equation 2.10:

$$K \times p^0 = \exp\left(\frac{q}{RT} + \frac{\Delta s^0}{R}\right) \text{ or } \ln K = \frac{q}{RT} + \frac{\Delta s^0}{R} - \ln p^0 \quad \text{Equation 2.10}$$

Where q is the heat of methane adsorption, Δs^0 is the standard entropy; p^0 is 0.1MPa as standard atmospheric pressure; R is the gas constant, $8.3145\text{JK}^{-1}\text{mol}^{-1}$. Langmuir constant at different temperatures is determined by Equation 2.9, and then a plot of $\ln K$ versus $\frac{1}{T}$ is provided as a fitted line. The slope is $\frac{q}{R}$ and the intercept is

$\frac{\Delta s^0}{R} - \ln 0.1$. Therefore, adsorption thermodynamic parameters can be obtained from

Langmuir isotherms at different temperatures.

2.3.4 Adsorption rate analysis

Methane adsorption rate can also be measured using Micromeritics high-pressure volumetric analyzer (HPVAII-200). The methane adsorption rate was measured to a maximum pressure of 50bar with a pressure step of 10bar. During each pressure step, pressure (every 0.002bar) in sample cell as a function of time was recorded until meeting the determined equilibrium criteria (pressure variation less than 0.003 bar in one minute or waiting for 60 minutes after dosing the gas into the reference cell). The adsorption rate at any time t can be obtained by the approximation (Busch et al., 2004):

$$M_t/M_\infty \approx (P_0 - P_t)/(P_0 - P_\infty) \quad \text{Equation 2.11}$$

Where, M_t/M_∞ is the ratio of the volume of adsorbed gas at time t and at equilibrium; P_t and P_∞ are the pressure in the sample cell at time t and at equilibrium respectively; P_0 is the first pressure in the pressure decay during the adsorption process. Some scholars have mentioned that the pressure increases in a few seconds to attain thermal equilibrium after opening valve and allowing the gas into the sample cell from manifold (Clarkson and Bustin, 1999). Therefore, the maximum pressure at each pressure step was regarded as P_0 . Furthermore, the temperature in the manifold was set to be consistent with the experimental temperature in the sample cell.

2.3.5 Bidisperse diffusion model

The bidisperse diffusion model describes the gas diffusion in a spherical particle comprising an agglomeration of small pores within a large pore (Ruckenstein et al., 1971). The small pore and large pore are regarded as micropore and macropore, respectively. The equations of gas diffusion in micropore and macropore are provided as following Ruckenstein et al., (1971):

$$\frac{D_a \varepsilon_a}{r_a^2} \frac{\partial}{\partial r_a} \left[r_a^2 \frac{\partial C_a}{\partial r_a} \right] = \varepsilon_a \frac{\partial C_a}{\partial t} + S_a \frac{\partial C_{sa}}{\partial t} + n4\pi R_i^2 \varepsilon_i D_i \left(\frac{\partial C_i}{\partial r_i} \right)_{r_i=R_i} \quad \text{Equation 2.12}$$

$$\frac{D_i \varepsilon_i}{r_i^2} \frac{\partial}{\partial r_i} \left[r_i^2 \frac{\partial C_i}{\partial r_i} \right] = \varepsilon_i \frac{\partial C_i}{\partial t} + S_i \frac{\partial C_{si}}{\partial t} \quad \text{Equation 2.13}$$

The solutions of the Equations 2.12 and 2.13 have been given based on the assumption of linear isotherms. Moreover, a simplified solution has also been provided to easily fit the adsorption rate data.

$$\frac{M_t}{M_\infty} = \frac{\left[1 - \frac{6}{\pi^2} \sum_{n=1}^{\infty} \frac{1}{n^2} \exp\left(-\frac{n^2 \pi^2 D_a' t}{R_a^2}\right)\right] + \frac{\beta}{3\alpha} \left[1 - \frac{6}{\pi^2} \sum_{n=1}^{\infty} \frac{1}{n^2} \exp\left(-\frac{n^2 \pi^2 \alpha D_i' t}{R_i^2}\right)\right]}{1 + \frac{\beta}{3\alpha}} \quad \text{Equation 2.14}$$

$$\text{Where } = \frac{D_i'}{R_i^2} \bigg/ \frac{D_a'}{R_a^2}; \quad D_a' = \frac{D_a}{1 + H_a S_a / \varepsilon_a}; \quad D_i' = \frac{D_i}{1 + H_i S_i / \varepsilon_i}; \quad \beta = \frac{3(1 - \varepsilon_a) \varepsilon_i R_a^2}{\varepsilon_a R_i^2} \frac{D_i}{D_a}$$

Where D_a is the macropore diffusivity, m^2/s , D_i is the micropore diffusivity, m^2/s ; ε_a is the macropore porosity, ε_i is the micropore porosity; r_a is the distance from macrosphere centre, m, r_i is the distance from microsphere centre, m; C_a is the macropore gas concentration, mol/m^3 , C_i is the micropore gas concentration, mol/m^3 ; C_{sa} is the macropore adsorbed gas concentration, mol/m^2 , C_{si} is the micropore adsorbed gas concentration, mol/m^2 ; H_a is the isotherm constant for macropore, m^3/m^2 , H_i is the isotherm constant for micropore, m^3/m^2 ; S_a is the macropore surface area, m^2/m^3 , S_i is the micropore surface area, m^2/m^3 ; R_i is the microspheres radius, m; R_a is the macrosphere radius, m; n is the number of microspheres per unit volume of macrosphere. The parameters in the equations, including $\frac{D_a'}{R_a^2}$ and $\frac{D_i'}{R_i^2}$ and $\frac{\beta}{\alpha}$ can be determined by fitting the adsorption rate data from experiment.

2.3.6 Low-pressure nitrogen and carbon dioxide adsorption analysis

Pore structure characteristics in shale were described by low-pressure nitrogen and carbon dioxide adsorption. Low-pressure nitrogen was measured on a Micromeritics® Tristar II apparatus at 77K. Carbon dioxide adsorption was measured on a Micromeritics® Tristar II plus apparatus at 273K. Both gas adsorption volume was measured over the relative equilibrium adsorption pressure (P/P_0) range of 0.01-0.99, where P is the gas vapor pressure in the system and P_0 is the saturation pressure of nitrogen.

The nitrogen adsorption data was interpreted by the Brunauer-Emmett-Teller (BET) method for BET surface area and nitrogen-based density functional theory for mesopores and macropores size distribution. The pore size range from the nitrogen-based density functional theory is 2.7 to 100nm. The surface area is calculated in the P/P_0 range of 0.1-0.3. The carbon dioxide adsorption data was interpreted using Dubinin-Astakhov (D-A) for micropores volume and micropores surface area, which

is calculated in the (P/P_0) range of 0.01-0.05. Carbon dioxide-based non-local density functional theory was used to describe the micropores size distribution. The pore size range from the carbon dioxide-based non-local density functional theory is 0.4 to 1.6nm. Therefore, there is a gap in pore size distribution between 1.6 and 2.7nm.

2.4 Determination of particle size used for sample preparation

Prior to the high-pressure adsorption experiment, the sample is crushed and sieved to particular particle size. Surprisingly, different particle size has been used in high-pressure methane adsorption related studies. Table 2.3 shows the particle size used in high-pressure methane adsorption related studies. A study by Clarkson and Bustin (1999) has suggested that a particle size of 4mesh (<4.75mm) and 60mesh (<0.250mm) coal sample has a negligible effect on high-pressure methane adsorption. Another study on pure clay samples has shown that methane adsorption capacity of clay minerals increases with decreasing particle size because of the enlarged internal surface area (Ji et al., 2012). Furthermore, the effect of particle size on gas adsorption porosimetry and high-pressure CO₂ adsorption has been investigated as well (Chen et al., 2015; Lutynski and González González, 2016), which has shown that micropore volume generally increases with particle size reduction. Although high-pressure methane adsorption has been widely used, the effect of particle size on the high-pressure methane adsorption is not clear.

Table 2.3 Particle sizes used in high-pressure methane adsorption related studies.

Literature	particle size (µm)
Gasparik, 2013	500-1000, <100
Ross and Bustin, 2009	<250
Chalmers and Bustin, 2012	<250
Zhang et al., 2012	150-500

To avoid wasting the collected shale samples, coal sample was used as analogy of organic matter of shale. We measured high-pressure methane adsorption on the same coal sample in different particle sizes. Low-pressure N₂ sorption was also engaged to give an insight into the pore structure characteristics of the studied samples.

For the purpose of this section, the particle size of the sample was the only experimental variable. Herein, commercial coal provided by BM Alliance coal

operations Pty Ltd was used. Table 2.4 shows the sample information. The mean Vitrinite Reflectance of the sample is 1.43%.

The original coal was sieved to four particle size range: 325mesh, 200-325mesh, 60-100mesh, and 18-20mesh. The samples were measured on high-pressure methane adsorption and low-pressure N₂ adsorption.

Table 2.4 Petrographic composition of BM Alliance coal sample.

Telovitrinite (%)	71.1
Detrovitrinite (%)	3.7
Fusinite (%)	3.3
Semi-Fusinite (%)	13
Macrinite (%)	0.3
Inertodetrinite (%)	4
Mineral matter (%)	4.5

2.4.1 Results

Figure 2.2 shows the comparison of low-pressure N₂ adsorption and desorption isotherms of samples with different particle sizes.

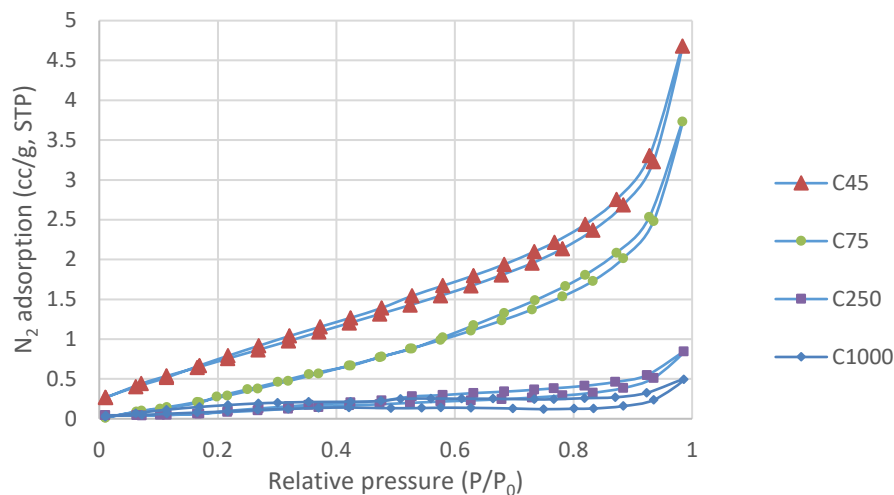


Figure 2.3 Low-pressure N₂ sorption/desorption isotherms of the studied samples at 77K: C45, C75, C250, and C1000 are sample names with particle size range in Table 2.5.

As shown in Table 2.5, total pore volume and BET surface area increase significantly with particle size reduction. The total pore volume of C45 sample is 0.733 cm³ per 100gram, which is nearly 10 times of total pore volume of C1000 sample (0.07 cm³

per 100gram). The BET surface area increases from 0.4757 m²/g to 3.3571m²/g from the coarsest to the finest sample. The BET surface area is the summary of the internal surface area and the external surface area. It is assumed that all particles are spherical. Based on the average radius of the studied samples, the external surface area can be calculated by the following formula:

$$a = 6 / \rho d$$

where a is the external surface area (with the assumption that the surface is completely smooth), ρ is the sample density, d is the particle diameter.

Table 2.5 Low pressure N₂ sorption result of the studied samples

Sample	Particle size range	BET surface area(m ² /g)	Total pore volume(cm ³ /100g)	External surface area(m ² /g)	Internal surface area(m ² /g)
C45	<45μm (325mesh)	3.36	0.7	5.82E-02	3.302
C75	45~75μm (325-200mesh)	3.29	0.56	3.64E-02	3.25
C250	150~250μm (100-60mesh)	0.58	0.13	1.09E-02	0.57
C1000	850~1000μm (20-18mesh)	0.48	0.07	2.36E-03	0.48

Given that the sample density here is the true density of coal, a value of 1.37g/cm³ is used for theoretical calculation (Stanton, 1982). The external surface area of samples with different particle size is shown in table 2.5. The internal surface area is obtained by subtracting an external surface area from BET surface area. The increase in BET surface area with particle size reduction mainly results from an increase in internal surface.

Figure 2.3 shows the pore size distribution of samples with different particle size using incremental pore volume. All studied samples reveal multimodal pore size distribution and pore volume increases with decreasing particle size. Although pore size distribution among varying particle size follows the same trend for pores larger than 10nm, it is different for pores less than 10nm: the main mode of C45 is between 2.5nm to 3.7nm; the main mode of C75 is between 3.7nm to 5.0nm; the main mode of C250 is between 3.0nm to 3.7nm. Table 2.6 is the pore volume proportion of samples with different particle size. It is shown that the pore volume proportion of small pores (<10nm) increases with particle size reduction.

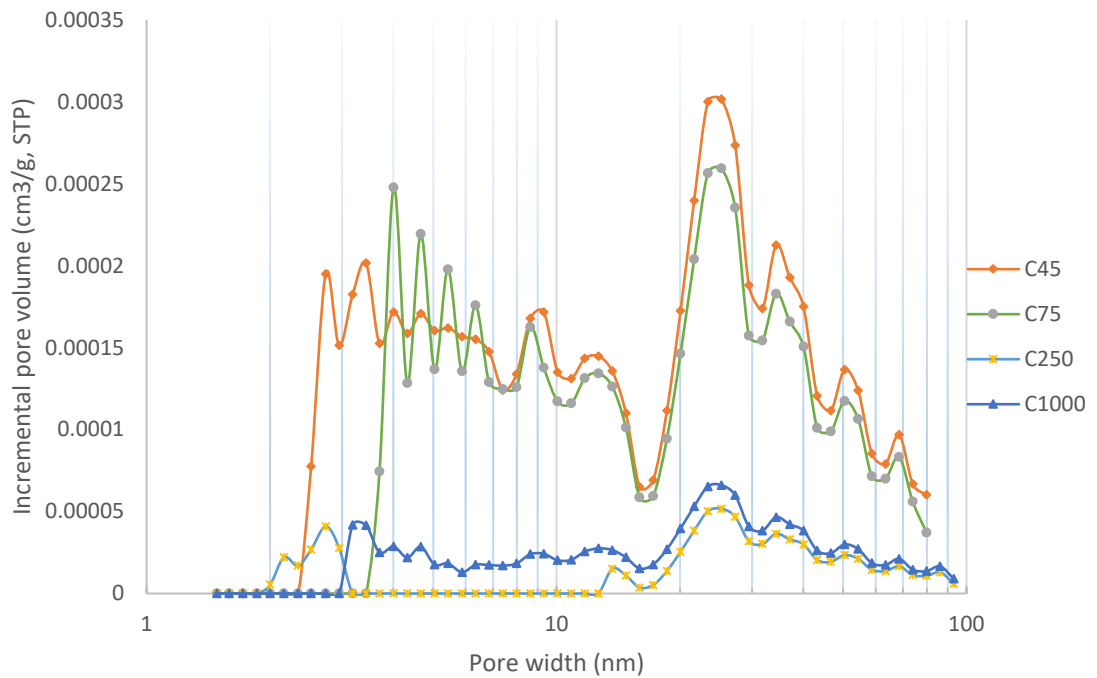


Figure 2.4 Pore size distribution defined by incremental pore volume at the pore width range of 1-100nm.

Table 2.6 Pore volume proportion of samples with different particle sizes

Sample name	Pore volume proportion of small pores(<10nm)	Pore volume proportion of big pores(>10nm)
C45	40.60%	59.40%
C75	35.70%	64.30%
C250	28%	72%
C1000	19.10%	80.90%

Figure 2.4 compares methane adsorption on coal samples with different particle size. Isotherm curves for samples with different particle size are different from each other. In general, methane adsorption capacity increases with decreasing particle size at 145psi and the adsorption increase rate of the fine sample decreases rapidly with increasing pressure. C45 has the highest methane adsorption capacity at 145psi and reaches its methane adsorption peak at 870psi. C250 has low methane adsorption capacity at 145psi, but the adsorption increase rate remains stable with increasing pressure. Therefore, the methane adsorption capacity of samples at 870psi with different particle size follows this order: C75>C250>C45 >C1000.

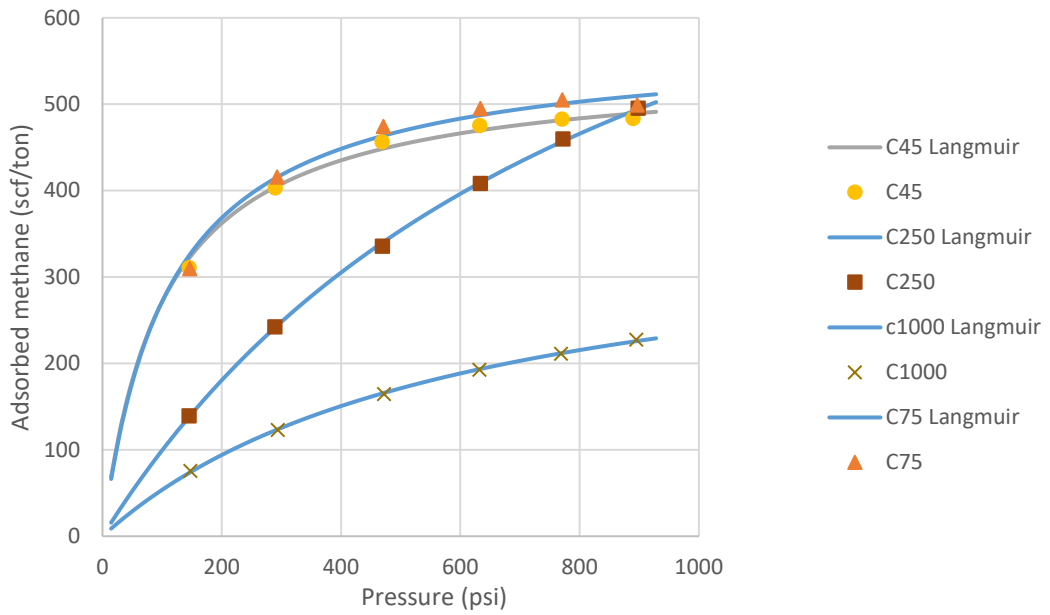


Figure 2.5 Comparison of methane adsorption of samples with different particle size at 30°C. Points are the experimental results and lines are the Langmuir fitting results.

As shown in Figure 2.4, methane adsorption isotherms can be well fitted by the Langmuir equation. Table 2.7 shows the Langmuir volume (V_L), Langmuir pressure (P_L) and correlation coefficient (R^2). Among samples with varying particle size, C250 has the highest Langmuir volume.

Table 2.7 Langmuir parameters of samples with different particle size

Sample	V_L (scf/ton)	P_L (psi)	R^2
C45	545	101	0.999
C75	573	111	0.998
C250	984	890	0.999
C1000	378	604	0.999

2.4.2 Discussion

Particle size can influence the pore structure of the sample significantly. The crushing sample creates new sections in particle and the sections can connect more pores to the particle surface. The introduced connectivity of pores enlarges the internal surface area and pore volume and changes pore size distribution. For coarse samples, small pores (<10nm) are neglected because the pressure equilibrium of N_2 sorption takes too much time to reach or small pores (<10nm) are isolated. As for fine sample, small pores (<10nm) are connected by new sections and pressure equilibrium of N_2 sorption is

easy to reach. Therefore, pore size distribution of small pores (<10nm) is different with decreasing particle size.

The hypothetical types of pores are shown in Figure 2.5 (Rouquerol et al., 2014). Decreasing particle size can influence closed pores rather than open pores (if pore channels are wide enough for probe gas). The introduced connectivity of isolated pores results in an increase in pore volume and surface area and the difference in pore size distribution. So the increase in total pore volume from C1000 to C45 indicates that isolated pores in studied coal sample is at least 10 times of open pores in terms of pore volume. Meanwhile, pore volume proportion of small pores (<10nm) increases with particle size reduction, so crushing sample connects more small pores than big pores (> 10nm). Therefore, isolated pores have more small pores (<10nm) than big pores (>10nm) in terms of pore volume.

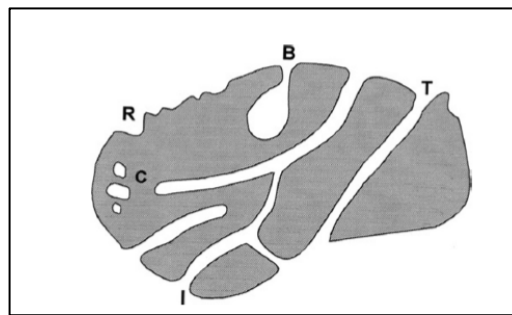


Figure 2.6 Cross section of a hypothetical particle (Rouquerol et al., 2014).

Methane adsorption capacity of coal sample is related to particle size. The studied coal sample with different particle sizes have different Langmuir volume and pressure. However, no trend is found between the Langmuir parameters and particle size. Sample C250 has the largest Langmuir volume and pressure. Besides, it has been reported that the particle fractions of coal sample have different compositions (Busch et al., 2004), which could be another reason that the particle size has an impact on methane adsorption and pore structure of coal sample.

Based on the experimental results, an appropriate particle size can be recommended for high-pressure methane adsorption experiment in this study. If sample powder is too fine, much new connectivity for small pores is introduced by crushing sample. If the sample is too coarse, the time to reach pressure equilibrium would be very long. Both small and big pores can be measured in the 150-250 μ m sample, and 150-250 μ m sample has the highest Langmuir volume.

References

- Busch, A., Gensterblum, Y., Krooss, B.M. and Littke, R., 2004. Methane and carbon dioxide adsorption–diffusion experiments on coal: upscaling and modeling. *International Journal of Coal Geology*, 60(2): 151-168.
- Chen, Y., Wei, L., Mastalerz, M. and Schimmelmann, A., 2015. The effect of analytical particle size on gas adsorption porosimetry of shale. *International Journal of Coal Geology*, 138: 103-112.
- Clarkson, C.R. and Bustin, R.M., 1999. The effect of pore structure and gas pressure upon the transport properties of coal: a laboratory and modeling study. 1. Isotherms and pore volume distributions. *Fuel*, 78(11): 1333-1344.
- Gasparik, M., Rexer, T.F.T., Aplin, A.C., Billemont, P., De Weireld, G., Gensterblum, Y., Henry, M., Krooss, B.M., Liu, S., Ma, X., Sakurovs, R., Song, Z., Staib, G., Thomas, K.M., Wang, S. and Zhang, T., 2014. First international inter-laboratory comparison of high-pressure CH₄, CO₂ and C₂H₆ sorption isotherms on carbonaceous shales. *International Journal of Coal Geology*, 132: 131-146.
- Greenspan, L., 1977. Humidity fixed points of binary saturated aqueous solutions. *Journal of research of the national bureau of standards*, 81(1): 89-96.
- Guo, S., Lü, X., Song, X. and Liu, Y., 2017. Methane adsorption characteristics and influence factors of Mesozoic shales in the Kuqa Depression, Tarim Basin, China. *Journal of Petroleum Science and Engineering*, 157: 187-195.
- Ji, L., Zhang, T., Milliken, K.L., Qu, J. and Zhang, X., 2012. Experimental investigation of main controls to methane adsorption in clay-rich rocks. *Applied Geochemistry*, 27(12): 2533-2545.
- Ji, W., Song, Y., Jiang, Z., Chen, L., Li, Z., Yang, X. and Meng, M., 2015. Estimation of marine shale methane adsorption capacity based on experimental investigations of Lower Silurian Longmaxi formation in the Upper Yangtze Platform, south China. *Marine and Petroleum Geology*, 68, Part A: 94-106.
- Ji, W., Song, Y., Jiang, Z., Wang, X., Bai, Y. and Xing, J., 2014. Geological controls and estimation algorithms of lacustrine shale gas adsorption capacity: A case study of the Triassic strata in the southeastern Ordos Basin, China. *International Journal of Coal Geology*, 134–135: 61-73.

- Lutynski, M. and González González, Miguel Á., 2016. Characteristics of carbon dioxide sorption in coal and gas shale – The effect of particle size. *Journal of Natural Gas Science and Engineering*, 28: 558-565.
- Rouquerol, F., Rouquerol, J., Sing, K.S.W., Maurin, G. and Llewellyn, P., 2014. 1 - Introduction, *Adsorption by Powders and Porous Solids (Second Edition)*. Academic Press, Oxford, pp. 1-24.
- Ruckenstein, E., Vaidyanathan, A.S. and Youngquist, G.R., 1971. Sorption by solids with bidisperse pore structures. *Chemical Engineering Science*, 26(9): 1305-1318.
- Stanton, R.W., 1982. Determination of the true density of pulverized coal samples. 82-835.
- Wang, Y., Zhu, Y., Liu, S. and Zhang, R., 2016. Methane adsorption measurements and modeling for organic-rich marine shale samples. *Fuel*, 172: 301-309.
- Western Australia Department of Mines and Petroleum, 2014. Natural gas from shale and tight rocks: An overview of Western Australia's regulatory framework. Access through website: www.dmp.wa.gov.au
- Zou, J., Rezaee, R. and Liu, K., 2017. The effect of temperature on methane adsorption in shale gas reservoirs. *Energy & Fuels*.

Chapter 3

Effect of temperature and moisture on methane adsorption in shales

3.1 Introduction

In-situ conditions such as the presence of moisture and high temperature can affect methane adsorption capacity in shale gas reservoirs significantly. Moisture is known to reduce methane adsorption in shale by occupying sorption sites. High temperature, as an important parameter of in-situ state of shale, reduces the methane adsorption capacity as methane adsorption in shales is physical adsorption and accompanied by heat release. Moreover, for the in-situ state of shale, the moisture and high temperature are always working together. By analyzing the results of adsorption experiments for pre-dried and pre-moisturized shale samples at different temperatures, this chapter attempts to address the effect of temperature, moisture, and their combined effect on methane adsorption capacity in shales.

A total of 6 shale samples were studied for the temperature and moisture effect on methane adsorption capacity in shale. The samples were measured on high-pressure methane adsorption at different temperatures in the dry and wet conditions described in Chapter 2. Low-pressure adsorption approach was also used to characterize pore structure of the samples studied.

3.2 Experimental results

3.2.1 Low-pressure adsorption analysis

Nitrogen and carbon dioxide sorption isotherms of all samples in dry and wet conditions are shown in Figures 3.1 and 3.2, respectively. Sample T-5 was only measured in dry condition. It is obvious that the dry sample adsorbs more N_2 and CO_2 than the wet one, except for sample AC-1.

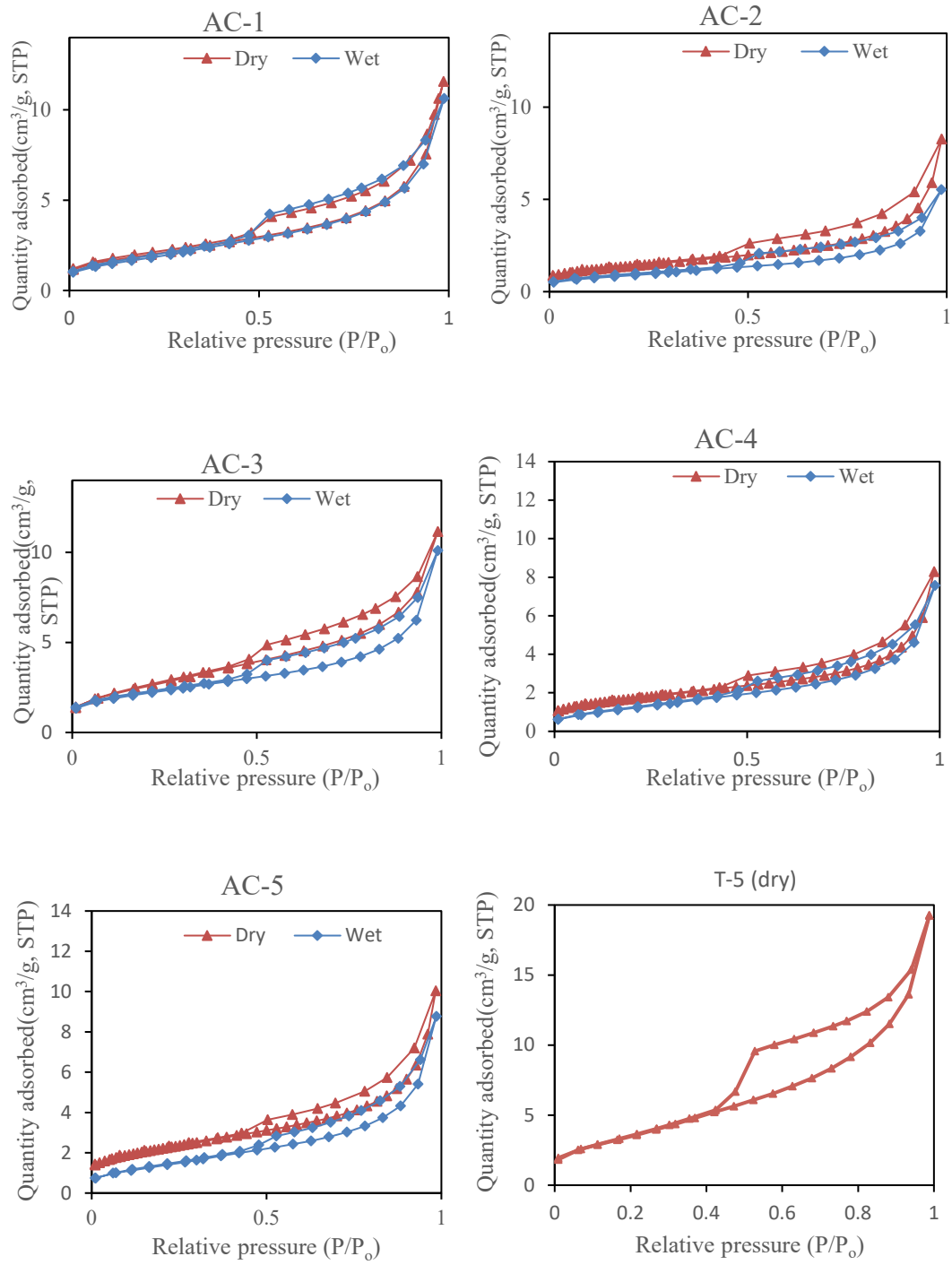


Figure 3.1 Low-pressure N₂ isotherms for the shale samples.

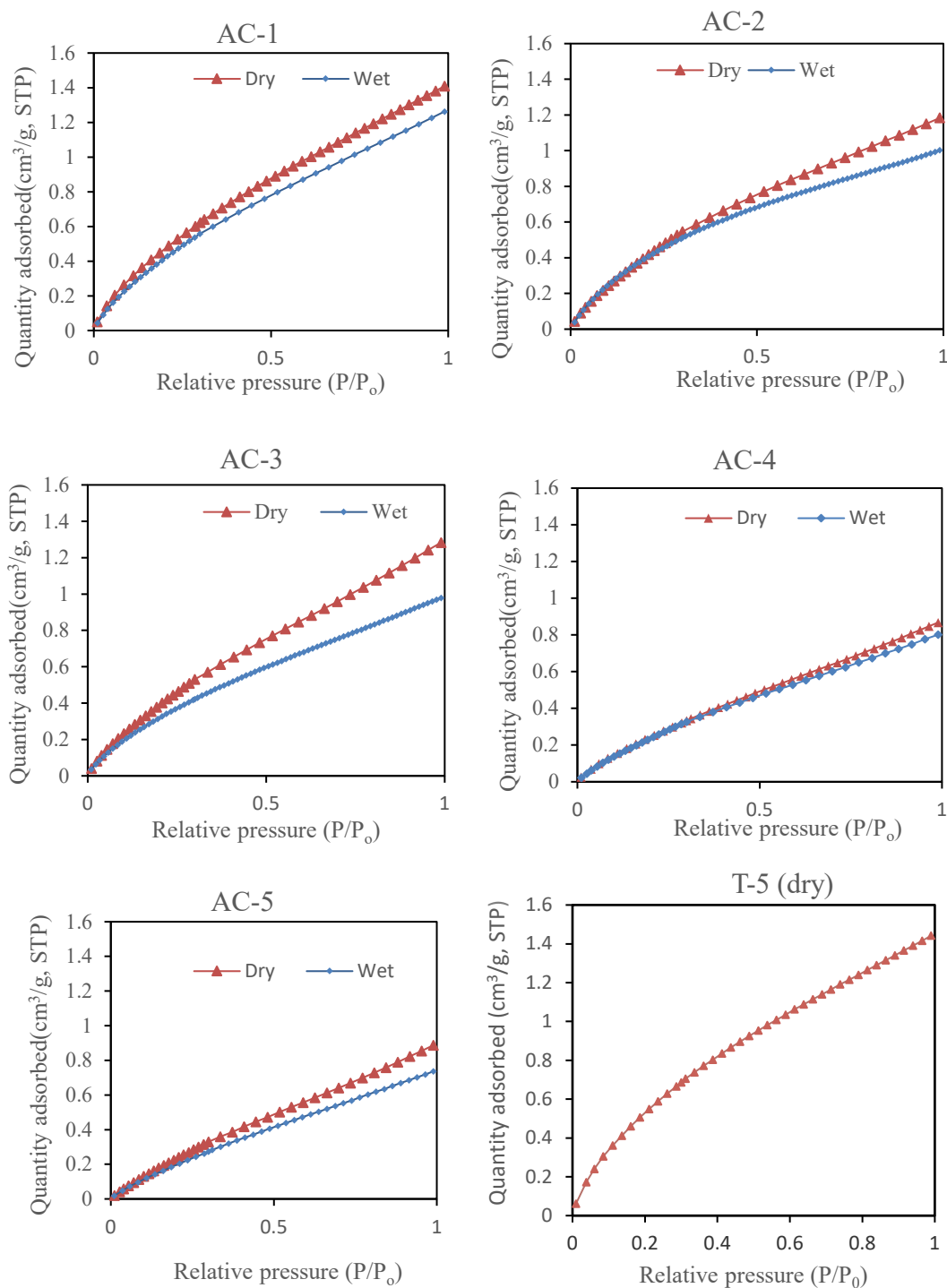


Figure 3.2 Low-pressure CO₂ adsorption isotherms for the shale samples.

Table 3.1 shows the BET surface area and total pore volume from N₂ isotherms and micropore volume from CO₂ isotherms. Sample AC-2 with low TOC (0.64) has large micropore volume. BET surface area of the dry sample is larger than that of the wet sample. The reduced percentage of BET surface area due to moisture for the studied samples ranges between 5.6% and 33.0%. Sample AC-1 has the smallest reduced

percentage value. The micropore volume of dry samples ranges between 0.1466 and 0.2844 cm³/100g, while for wet samples this value varies from 0.1361 to 0.1919 cm³/100g. The reduced percentage of micropore volume for the studied samples ranges between 3.7% and 32.7%. As can be noted, the change in the percentage of micropore volume of AC-4 and AC-5 is smaller than the other samples.

Table 3.1 Pore structure parameters derived from low-pressure nitrogen and carbon dioxide adsorption for the studied samples.

	BET surface area (m ² /g)			Total pore volume (cm ³ /100g)			Micropore volume (cm ³ /100g)		
	Dry	Wet	Reduction (%)	Dry	Wet	Reduction (%)	Dry	Wet	Reduction (%)
AC-1	7.1	6.7	5.6	11.6	10.5	9.0	0.2844	0.1913	32.7
AC-2	4.9	3.3	33.0	8.3	5.5	33.0	0.2665	0.1896	28.9
AC-3	9.7	7.6	21.1	11.2	10.1	9.3	0.2679	0.1919	28.4
AC-4	6.0	4.7	21.9	8.3	7.6	8.6	0.1625	0.1565	3.7
AC-5	7.8	5.2	33.0	10.0	8.8	12.6	0.1466	0.1361	7.2
T-5	13.7	N/A	N/A	19.3	N/A	N/A	0.2094	N/A	N/A

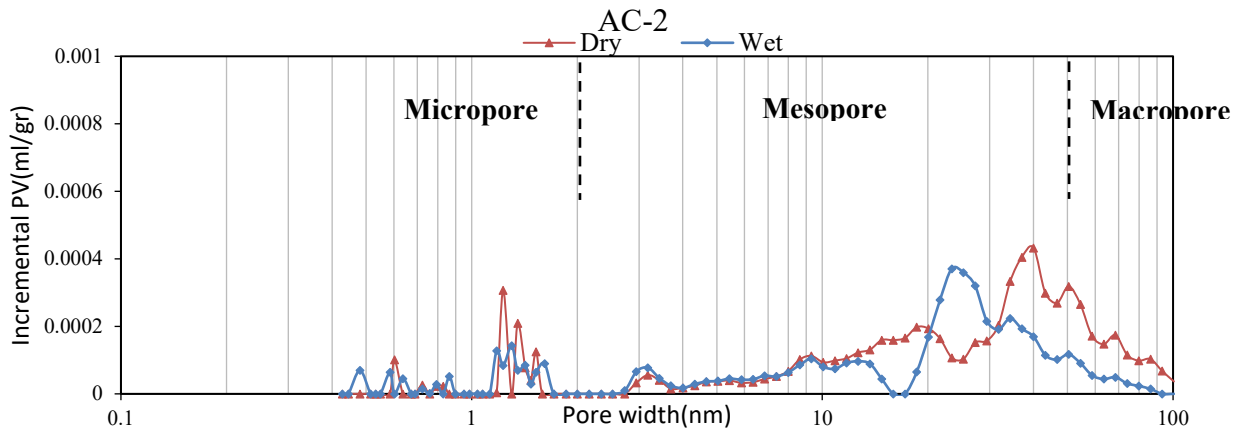
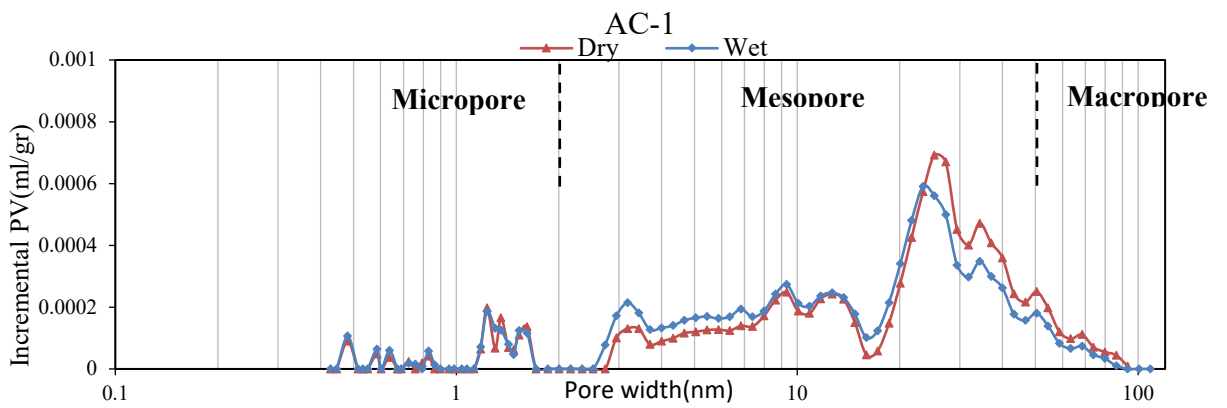
N₂ isotherms in Figure 3.1 are of type II, which can be described as slit model (De Boer, 1958). Therefore, the slit model was applied in the density functional theory model to determine the pore size distribution. Figure 3.3 illustrates that the pore size distribution from low-pressure nitrogen and carbon dioxide adsorption isotherms focus on nano-scale pores ranging from 0.4 to 100nm. All studied samples reveal multimodal pore size distribution, demonstrating complex pore structures in the studied samples.

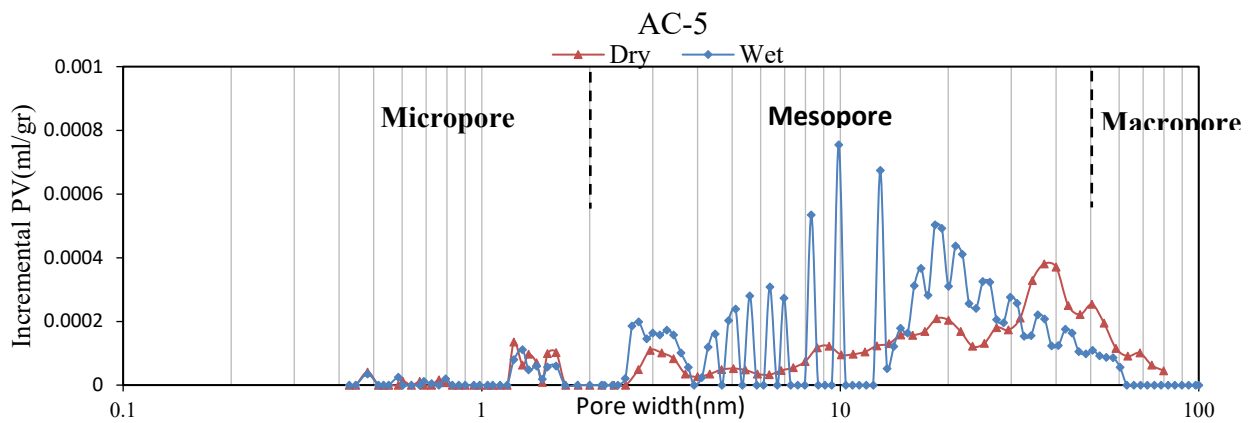
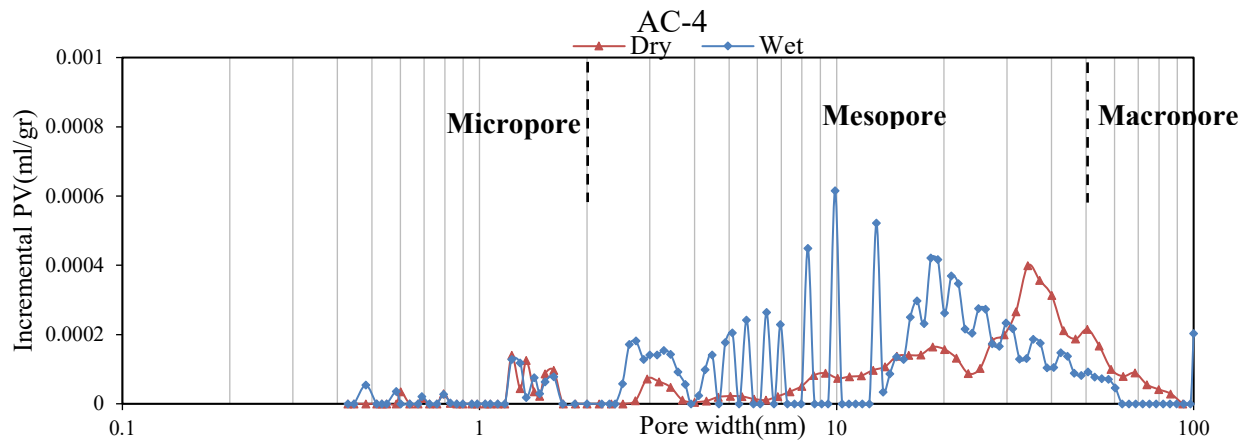
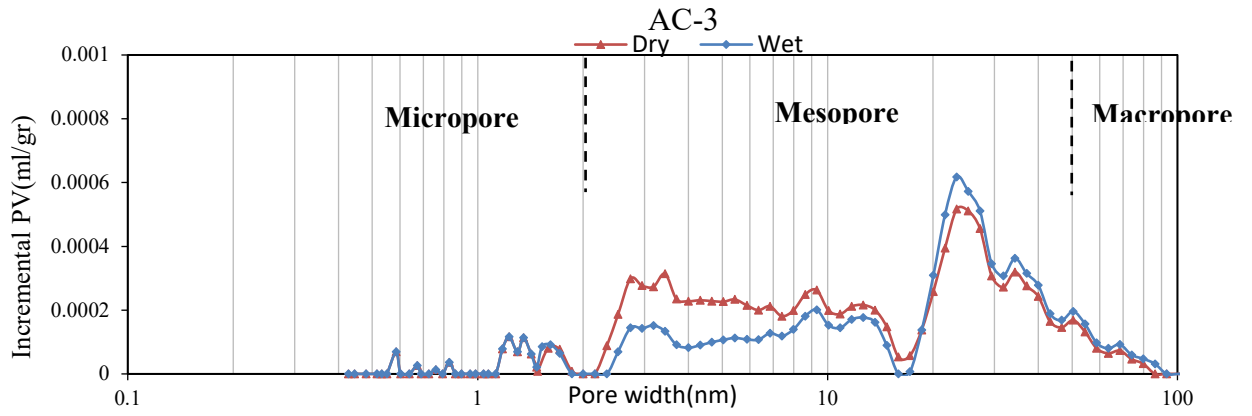
According to the comparison of pore size distribution (PSD) between the dry and wet samples, the change in PSD shape of the samples after moisturizing can be grouped into three different ranges of pore diameter.

- (1) Micropores (0.4-2 nm): The dry and wet samples have minimal or no obvious difference in the PSD shape for sample AC-1, AC-3, AC-4, while sample AC-2 and AC-5 have more striking changes in PSD shape after moisturizing for pore diameters ranging from 1.1 to 1.6nm.
- (2) Fine mesopores (2-16 nm): Sample AC-1 and AC-2 have very similar PSD shapes in the dry and wet states. For sample AC-3, the dry sample has a much larger pore volume than the wet sample. The PSD of wet samples for sample

AC-4 and AC-5 appears in the discrete form, which is different from the continuous PSD of dry samples.

- (3) Big mesopores and macropores (16-100nm): No obvious change exists in the PSD shape after moisturizing for sample AC-3 and sample AC-1. Apart from these two samples, the other samples have a distinct shift toward smaller pore width from the dry to wet samples.





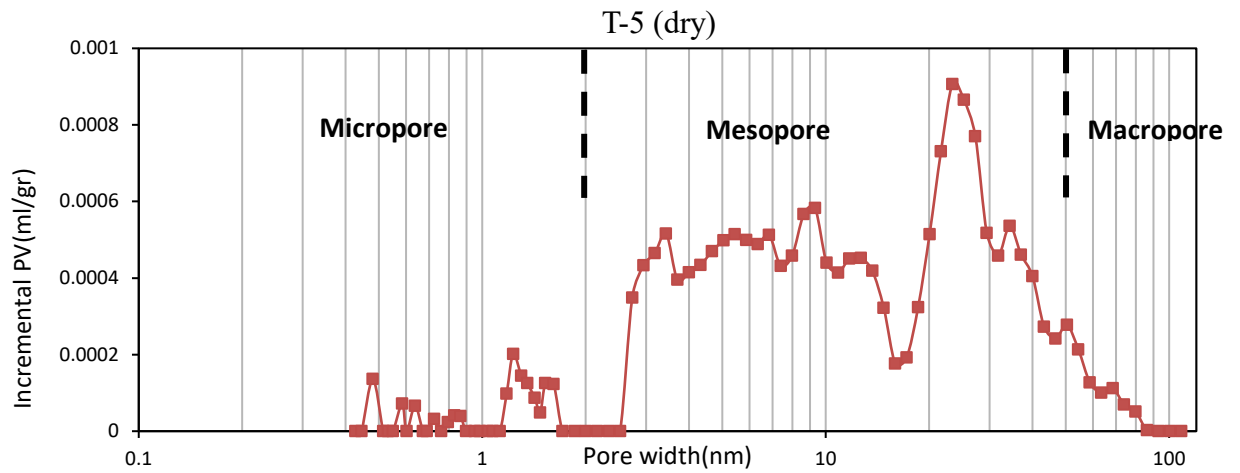
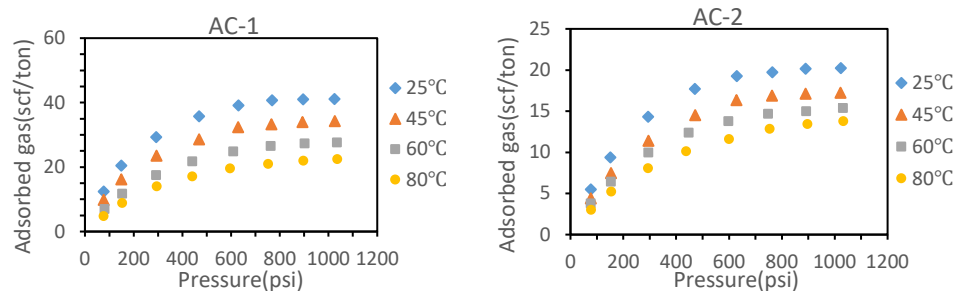


Figure 3.3 Pore size distribution defined by incremental pore volume within the width range of 0.4 to 100nm for the studied samples.

3.2.2 High-pressure methane adsorption isotherms analysis

Figure 3.4 shows methane adsorption isotherms for the dry shale samples at different temperatures. Under the same pressure, as the temperature increases, the adsorption decreases. At 25°C the adsorption capacity of the studied samples decreases in the following order: T-5 > AC-1 > AC-3 > AC-4 > AC-5, which is consistent with the order of TOC contents (Figure 3.5).

In order to quantify the effects of the pressure and temperature on the methane adsorption, we derived the adsorption quantity of the samples under various temperature and pressure and the results can be seen in Figure 3.6. Adsorbed methane content decreases with increasing temperature at each pressure. The slope of the curve, regarded as the decrease rate of methane adsorption with increasing temperature, increases with increasing pressure from 5 to 50bars (725.2psi) but remains stable when pressure keeps increasing from 50 to 70bars (1015.3psi).



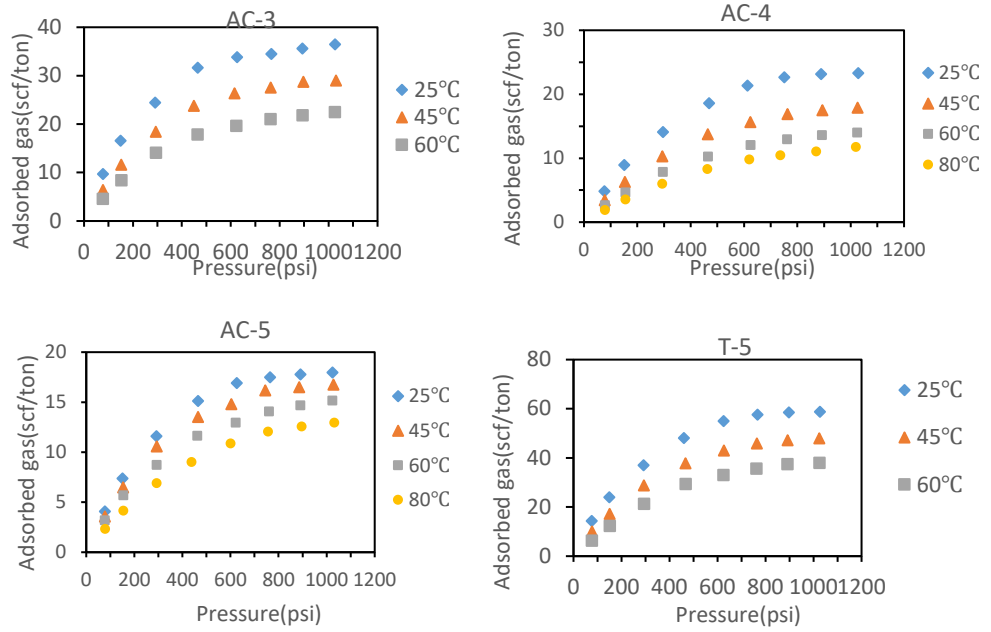


Figure 3.4 Methane adsorption capacity for the dry shale samples at different temperatures.

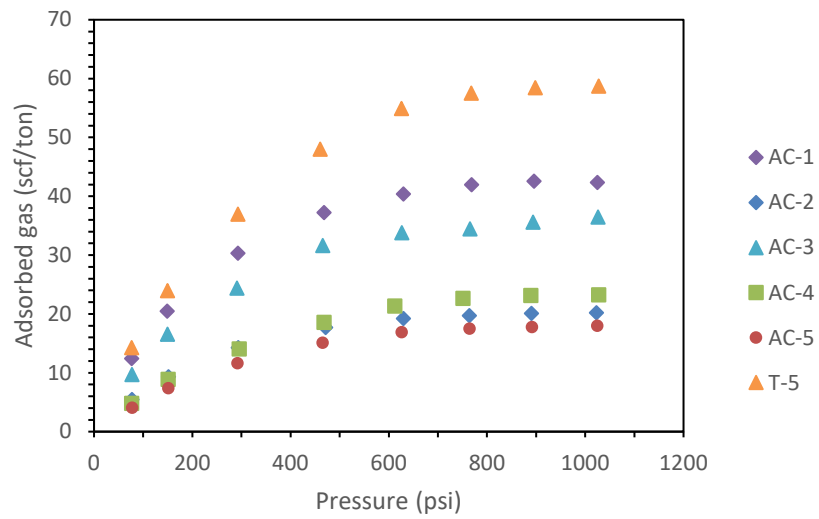


Figure 3.5 Comparison of methane adsorption isotherms for the dry shale samples at 25°C. Note that sample AC-2 has more adsorbed gas content than sample AC-4 at the first 3 pressure points.

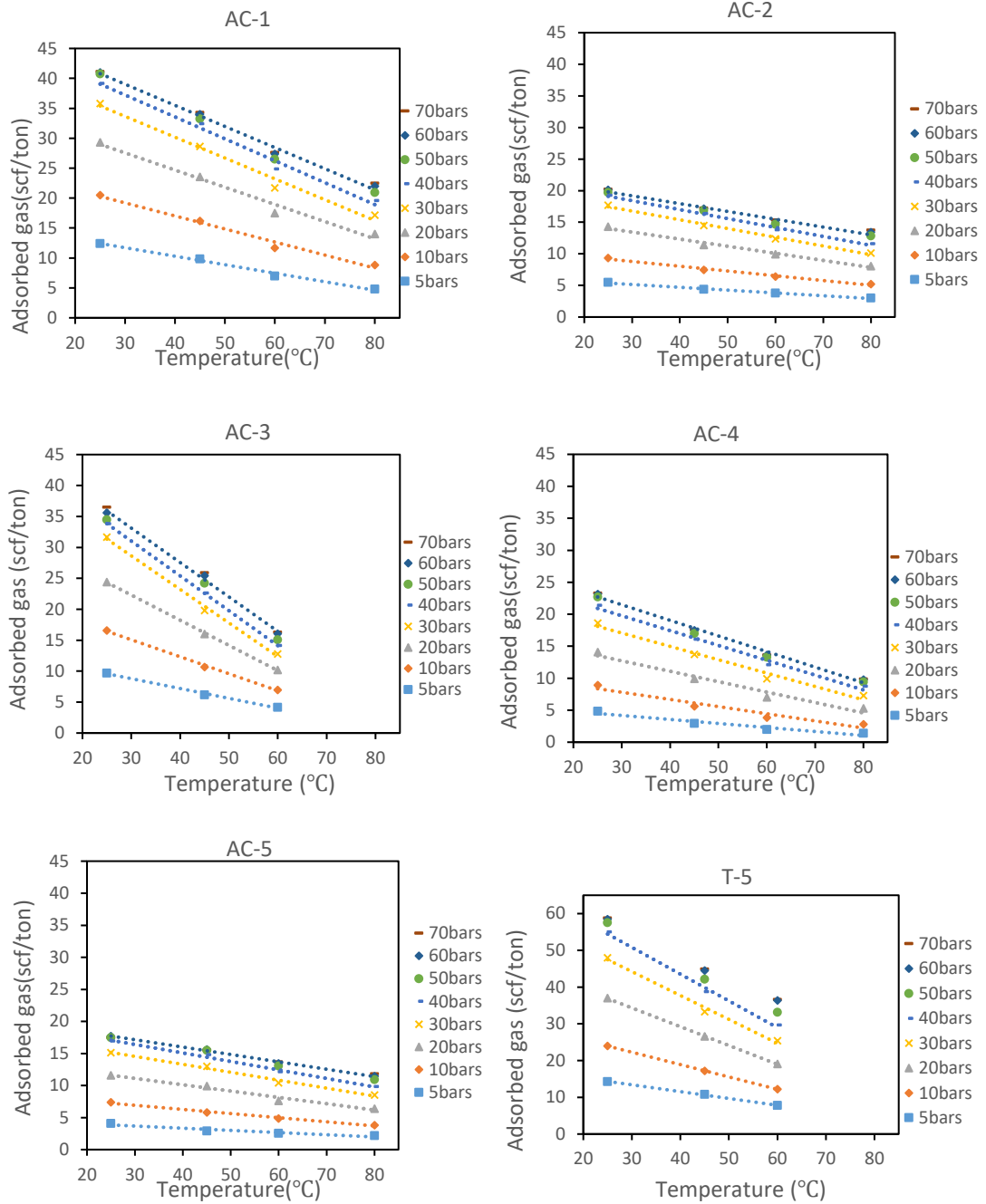


Figure 3.6 Comparison of correlations between temperature and adsorbed methane under isobaric conditions. The points are the experimental results and the dotted curves are the linear regression fitting results.

Figure 3.7 shows the comparison of methane adsorption isotherms for dry and wet samples at three different temperatures (25, 45 and 60°C). For each sample, methane adsorption capacities of the dry and wet sample decrease with increasing temperature. Compared with wet samples, the dry sample has larger methane adsorption at the same temperature. Meanwhile, the differences in methane adsorption between the dry and wet samples decrease with rising temperature. For sample AC-1, the difference of

methane adsorption between the dry and wet sample at maximum experimental pressure decreases from 7.1 to 3.5 scf/ton as the temperature increases from 25 to 60°C.

Figure 3.8 shows the comparison of methane adsorption isotherms for the wet samples at 60°C. At this high temperature the moisture equilibrated, high TOC samples AC-1 and AC-3 (3.3% and 1.82% TOC) have larger methane adsorption capacities than the other samples AC-2, AC-4, and AC-5 with TOC values ranging from 0.23 to 1.08% have similar methane adsorption isotherms.

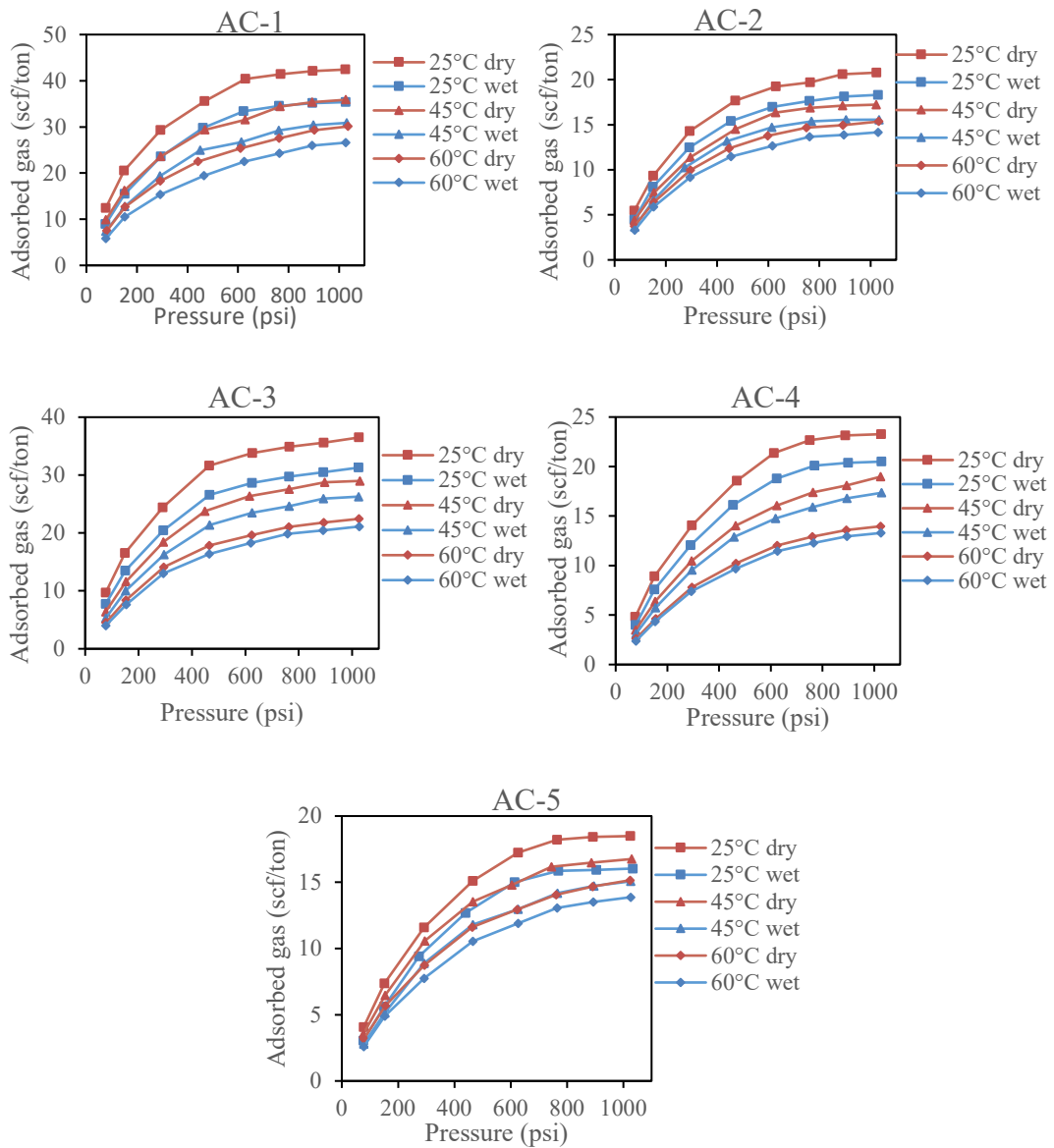


Figure 3.7 Comparison of methane adsorption isotherms between dry and wet shale samples at different temperatures: the red and blue dots represent the dry and wet samples, respectively.

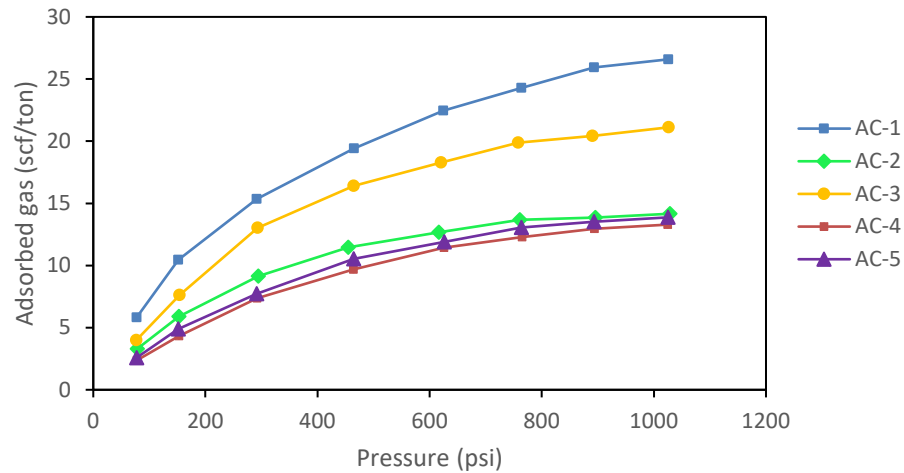


Figure 3.8 Comparison of methane adsorption isotherms at 60°C for wet samples: sample AC-2, AC-5, and AC-5 have similar results.

Methane adsorption isotherms can be well fitted by the Langmuir equation and the fitting results are presented in Table 3.2. For the dry samples, Langmuir volumes decrease and Langmuir pressures increase with increasing temperature; The Langmuir volume of the shale samples shows different degrees of change upon temperature increase from 25°C to 80°C. For instance, Langmuir volumes of methane adsorption on samples AC-1 and AC-4 decrease from 51 to 37 (scf/ton) (27.5% change) and 34 to 20 (scf/ton) (41.1% change), respectively. However, Langmuir volumes on samples AC-2 and AC-5 both decrease from 26 to around 20 (scf/ton) (23.1% change).

Comparison between the dry and wet samples shows a decrease in Langmuir volume after moisturization. At 60°C, the Langmuir volume of wet samples decreases in the order AC-1>AC-3>AC-4=AC-5>AC-2, which is not in agreement with the order of TOC contents. Compared with the dry samples, the wet samples have a higher Langmuir pressure at any temperature. As shown, the Langmuir pressures of wet samples at 60°C are significantly higher than those of the dry sample at 25°C.

Table 3.2 Langmuir parameters for the shale samples at different temperatures.

		25°C		45°C		60°C		80°C	
		V _L (scf/ton)	P _L (psi)	V _L (scf/ton)	P _L (psi)	V _L (scf/ton)	P _L (psi)	V _L (scf/ton)	P _L (psi)
AC-1	dry	51.3	218.9	46.3	277.8	40.2	346.9	37.6	433.8
	wet	46.9	294.8	41.7	338.7	37.5	388.7	N/A	N/A
AC-2	dry	26.9	256.1	23.1	306.7	20.6	322.5	19.8	429.2
	wet	24.2	294.8	21.2	316.9	19.4	344.2	N/A	N/A
AC-3	dry	46.5	263.8	40.5	364.3	32.5	424.9	N/A	N/A
	wet	41.2	299.4	38.2	421.6	31.5	468.8	N/A	N/A
AC-4	dry	34.2	422.1	29.5	544.6	22.2	562.0	20.5	729.7
	wet	31.2	464.5	27.7	575.0	21.5	588.1	N/A	N/A
AC-5	dry	26.5	383.5	24.0	398.3	22.1	445.3	20.7	505.4
	wet	24.7	475.3	23.4	521.8	21.5	522.1	N/A	N/A
T-5	dry	80.6	338.2	63.7	371.7	50.3	481.4	N/A	N/A

3.3 Discussion

3.3.1 The effect of temperature on methane adsorption

The effect of temperature on methane adsorption of shale samples is related to their composition. As shown in Figure 3.6, methane adsorption decreases with increasing temperature under isobaric condition. The decrease rate, used to describe the effect of temperature on methane adsorption, differs from pressure to pressure and sample to sample. For each sample, the decrease rate increases with increasing pressure for pressure less than 50bars. Meanwhile, as a general rule of physisorption, adsorbed gas content increases with increasing pressure. The trend of adsorbed gas content with pressure is in line with the trend of the decrease rate with pressure. So it is reasonable to guess the decrease rate is positively related to adsorbed gas content.

However, the correlation between the decrease rate and adsorbed gas content is not true of shale samples with different compositions. Figure 3.9 shows that the correlation between adsorbed gas content and the decrease rate follows this order: AC-3 > T-5 > AC-1 = AC-4 > AC-2 = AC-5. Sample AC-2 and AC-5 are less sensitive to the increased temperature on methane adsorption comparing to the other samples with relatively high TOC. Adsorbed gas content normalized by TOC at 80°C presented in

Figure 3.10, displays samples AC-2 and AC-5 with low TOC have abnormally larger TOC-normalized adsorbed gas content than sample AC-1 and AC-4 with relatively high TOC. It might infer that the proportion of methane adsorbed on clay minerals is much higher for sample AC-2 and AC-5 than sample AC-1 and AC-4. The lesser sensitivity to the increased temperature for sample AC-2 and AC-5 could attribute to the higher proportion of methane adsorbed on clay minerals, which implies the methane adsorbed on clay minerals is less sensitive to the increased temperature than that adsorbed on kerogen. Even when relatively high TOC and low TOC samples have the same adsorbed gas content at different pressures, the decrease rate of methane adsorption with increasing temperature is greater on relatively high TOC sample, which also suggests that the methane adsorbed on kerogen is more sensitive to the increased temperature on methane adsorption than on clay minerals.

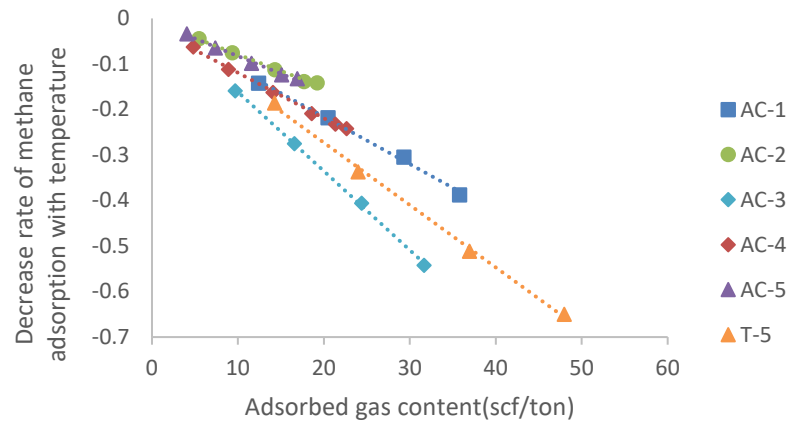


Figure 3.9 Comparison of correlations between adsorbed gas content and the decrease rate of methane adsorption with increasing temperature.

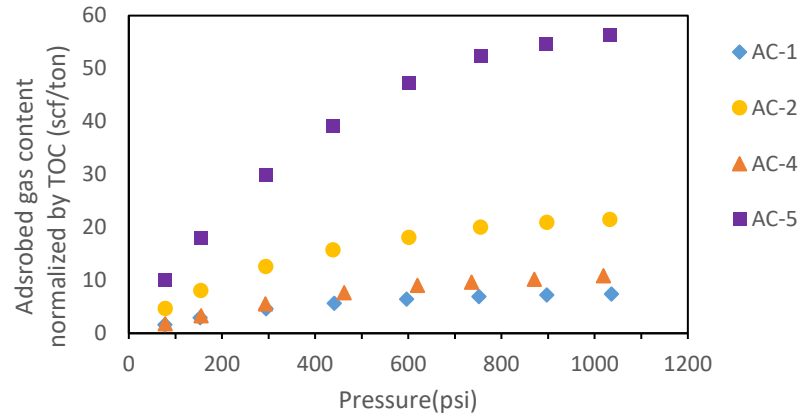


Figure 3.10 Comparison of adsorbed gas content normalized by TOC at 80°C for four shale samples. Samples AC-2 and AC-5 have larger adsorbed gas content normalized by TOC than samples AC-1 and AC-4.

3.3.2 The effect of moisture on pore structure characteristics

The comparison of N₂-based and CO₂-based adsorption isotherms, PSD shapes and pore structure parameters between dry and wet samples prove that the pore structure characteristics in shales change substantially after moisturizing. In PSD shapes, the most striking phenomenon is the left shift mode for big mesopores and macropores from dry to wet sample. The possible reason could be that the pore diameter of the big mesopores and macropores is reduced due to adsorbed water, and the water which is adsorbed on the pore walls has a similar thickness. As shown in Figure 3.11, D and d are the pore diameter of one pore from the dry and wet sample respectively; D-d represents the change of pore diameter from the dry to the wet sample, which is the distance of the left shift. Adsorbed water on the surface of pore displays as a film with a certain thickness. The thickness of adsorbed water can be generally described by the half distance of the shift mode. In this case, the thickness of adsorbed water for AC-2, AC-4, and AC-5 ranges from 8 to 9nm. It has been reported the thickness of adsorbed water in shales is controlled by various factors, such as relative humidity, pore size, and clay type (Li et al., 2016a; Li et al., 2017; Li et al., 2016b). Besides, no shift exists in the PSD of sample AC-3 and AC-1, which suggests limited hydrophilic sites in big mesopores and macropores of the samples.

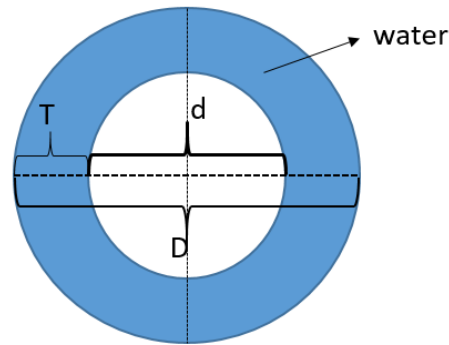


Figure 3.11 Theoretical pore model for the thickness of adsorbed water, D and d are the pore diameter of at dry and wet conditions respectively; T is the thickness of adsorbed water, which can be defined as $(D-d)/2$; $D-d$ represents the distance of the left shift in PSD.

Compared with the big mesopores and macropores, fine mesopores have no systematic change in pore structure characteristics after moisturizing for all samples. For sample AC-1 and AC-2, no significant change in PSD of fine mesopores exists after moisturizing, demonstrating no hydrophilic sites in fine mesopores. Sample AC-3 has a distinct decrease in the pore volume of fine mesopores from dry to wet sample, but different from the shift mode mentioned for the big mesopores and macropores. Due to the narrow enough pore throat of fine mesopores, the adsorbed water with certain thickness could block pore network connectivity and isolate potential sorption sites. With respect to sample AC-4 and AC-5, PSD of fine mesopores is discontinuous for the wet sample. The PSD is calculated by fitting isotherms from DFT model on individual pores to experimental isotherms of N_2 (Lastoskie et al., 1993). The possible reason for the discontinuous PSD is the reduced pore volume after moisturization.

Micropores characteristics in shales are also changed by moisture according to the decrease in micropore volume and change of PSD in micropores between the dry and wet samples. However, the change in PSD shape for high TOC samples is not as obvious as that for low TOC samples. Low TOC samples (AC-2, AC-5) have a larger proportion of clay-hosted micropore volume than high TOC samples (AC-1, AC-3, and AC-4). Micropore volume normalized by TOC is shown in Figure 3.12, indicating that low TOC samples (AC-2 and AC-5) have abnormally larger normalized micropore volume than high TOC samples. The proportion of clay-hosted microporosity for these low TOC samples is much larger than the other three samples. Water mainly adsorbs on the hydrophilic sites at the surface of clays, so both micropore volume and PSD of micropores in low TOC samples changes significantly with moisture. As for high TOC samples (AC-1, AC-3, and AC-4) with a low proportion of clay-hosted microporosity

and a high proportion of organic matter-hosted microporosity, the similar PSD between the dry and wet sample indicates that the amount of hydrophilic sites in organic matter is very limited. However, the high TOC sample (AC-1, AC-3) with no obvious change in PSD has a striking decrease in micropore volume after moisturizing. The phenomenon implies that micropore volume in the high TOC sample decreases evenly along the pore diameter range by adsorbed water. The reduced micropore volume is composed of the clay-hosted and organic matter-hosted micropore volume. Therefore, even though water adsorbed on clay blocks the narrow throat directly, organic matter-hosted micropores connected to the narrow throat is blocked indirectly. The largely reduced micropore volume of sample AC-1 and AC-3 illustrates that a significant amount of organic matter-hosted micropores is connected to the clay-hosted throat and could be indirectly blocked by adsorbed water.

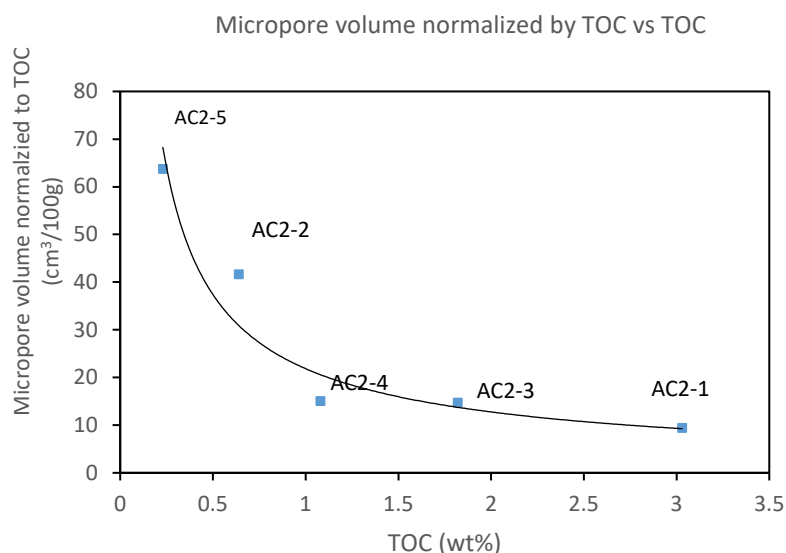


Figure 3.12 Micropore volume normalized to TOC for the dry samples.

3.3.3 The effect of moisture on methane adsorption characteristics

Methane adsorption capacity in shale-gas systems changes along the entire pressure range due to the presence of moisture. The effect of moisture on methane adsorption changes with increasing pressure. The ratio of $V_{\text{reduction}}/V_{\text{dry}}$ ($V_{\text{reduction}}$ refers to $V_{\text{dry}} - V_{\text{wet}}$) in Figure 3.13, which can quantify the effect of moisture on methane adsorption, decreases first and then becomes stable with increasing pressure. $V_{\text{reduction}}$ in Figure 3.14, the reduction of methane adsorption capacity with moisture, increases at the first stage and then remains stable during the second stage with increasing pressure.

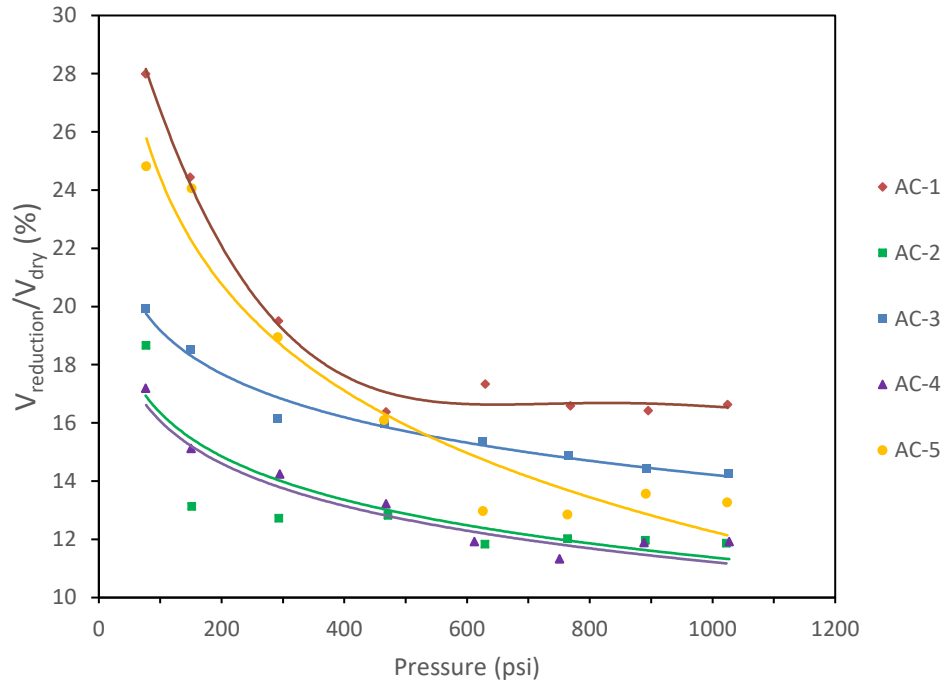


Figure 3.13 The reduced percentage of methane adsorption with moisture as a function of pressure for all shale samples. The solid line represents the general trend of the points.

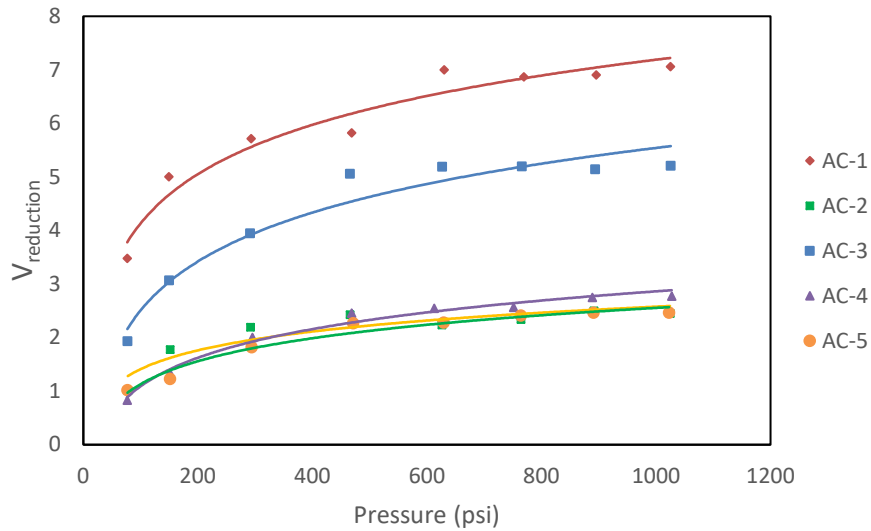


Figure 3.14 The reduction of methane adsorption with moisture as a function of pressure for all shale samples: $V_{\text{reduction}} = V_{\text{dry}} - V_{\text{wet}}$. The solid line represents the general trend of the points.

Therefore, at the first stage with low pressure, the decrease of $V_{\text{reduction}}/V_{\text{dry}}$ with increasing pressure suggests that the effect of moisture on methane adsorption decreases with increasing pressure. According to the pore-filling theory, gas is adsorbed in small pores first and then into bigger pores with increasing pressure. It might infer that the moisture effect on the methane adsorption is stronger in small

pores than larger pores. This is because that the small pores like micropores discussed in the last section could be thoroughly blocked by adsorbed water and not available to methane adsorption. With increasing pore diameter, larger pores like mesopores are less likely to be blocked by adsorbed water than small pores. Methane is gradually adsorbed into bigger pores with increasing pressure, but the effect of moisture on methane adsorption decrease.

At the second stage with high pressure, the difference of methane adsorption between the dry and wet samples attributes to the multilayer adsorbed water in big pores like big mesopores and macropores. $V_{\text{reduction}}$ and $V_{\text{reduction}}/V_{\text{dry}}$ both become relatively stable, which indicate the effect of the adsorbed water on methane adsorption in big pores is very limited. This finding could be explained in four assumptions: 1) the amount of methane adsorbed in big pores is very limited, as methane adsorption capacity in shales is mainly controlled by micropores and fine mesopores (Mosher et al., 2013); 2) Methane and moisture may adsorb at different sorption sites. It has been observed that shale can have both high moisture content and methane adsorption capacity (Chalmers and Bustin, 2008). In this case, moisture can reduce methane adsorption only if blocking connectivity of the pore network; 3) the coverage of adsorbed water is not sufficient. Methane adsorption capacity decreases with increasing of water coverage on clays (Li et al., 2016a). The limited reduction of methane adsorption in big pores may result from the small coverage of adsorbed water; 4) Methane is dissolved in water at high pressure. As reported, methane solubility in water increases with increasing pressure (Duan et al., 1992; Ma and Huang, 2017). With increasing pressure to the second stage, methane dissolved in water may weaken the moisture effect on methane adsorption.

The effect of moisture on methane adsorption in shales is related to TOC for the studied samples. The $V_{\text{reduction}}/V_{\text{dry}}$ at maximum pressure (1015psi) and $V_{L\text{reduction}}/V_{L\text{dry}}$, used to describe the effect of moisture on methane adsorption for each sample, have a positive correlation with TOC rather than clay content for the studied samples (Figure 3.15). The correlation demonstrates that high TOC sample is more sensitive to moisture comparing with low TOC sample on methane adsorption. In other words, clay adsorbs moisture directly, but the moisture effect on methane adsorption is related to organic matter. Organic matter-hosted small pores, as micropores discussed in the last section, could be indirectly blocked by water adsorbed on clay. Therefore, the

positive relation between moisture effect on methane adsorption and TOC illustrates that the high TOC sample has a large proportion of organic matter-hosted small pores blocked by adsorbed water, which is in agreement with the result of micropore volume.

In addition, $V_{L\text{reduction}}/V_{L\text{dry}}$ of samples AC-2 (0.64% TOC) is higher than that of sample AC-4 (1.08%TOC). This is because the low TOC sample has a larger proportion of methane adsorption capacity on clay. Although the amount of organic matter-hosted small pores blocked is limited in low TOC sample, the reduced pore volume from clay-hosted pores can lead to a significant decrease in methane adsorption capacity.

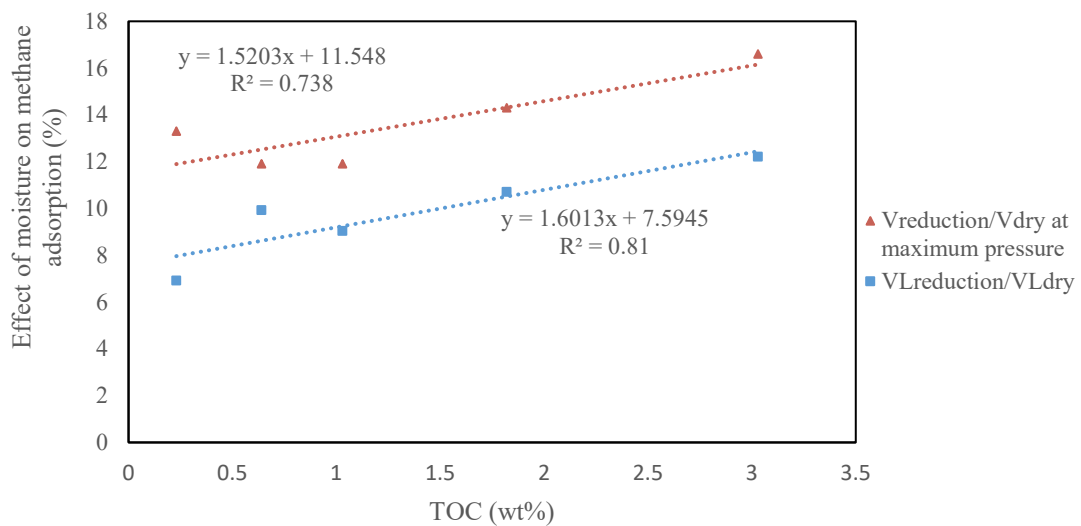


Figure 3.15 Relation between the effect of moisture on methane adsorption and TOC for shale samples. The red line describes the correlation of $V_{\text{reduction}}/V_{\text{dry}}$ at maximum pressure (1015psi) to TOC, the blue line represents the correlation of $V_{L\text{reduction}}/V_{L\text{dry}}$ to TOC.

The correlation between TOC and reduction of methane adsorption with moisture in Figure 3.16 is not in agreement with the trend reported by Wang and Yu (2016), which suggested a negative correlation between TOC and the differences on methane adsorption between dry and wet shales. The possible reason could be that the shale samples in the reported study show a positive relationship between the methane adsorption capacity and the clay content instead of the TOC, which indicates a high proportion of methane adsorption on clay. Thus, the reduced methane adsorption with moisture has no positive relation with TOC.

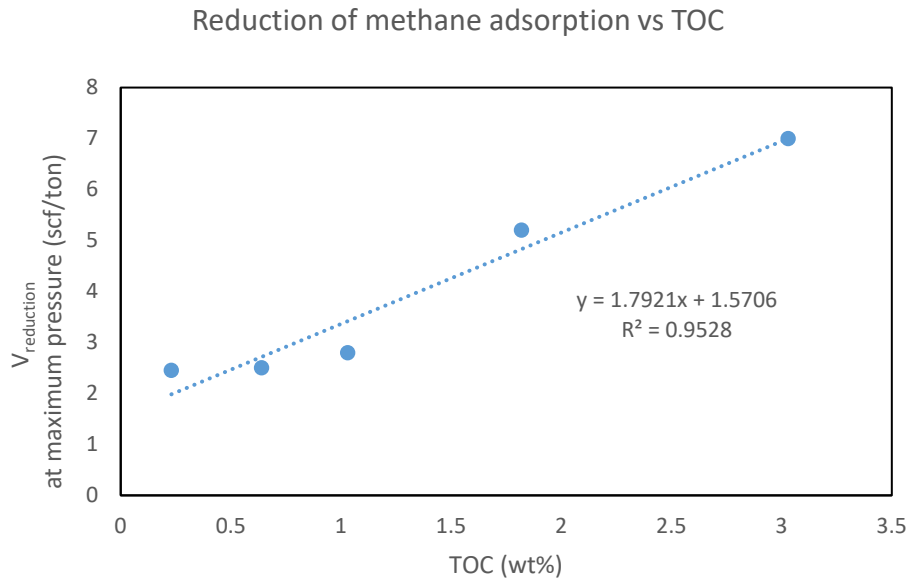


Figure 3.16 The correlation between the TOC and reduction of methane adsorption with moisture at maximum pressure.

3.3.4 Methane adsorption characteristics at high temperature with moisture

The organic fraction (TOC) is the main controlling factor of methane adsorption in shales at high temperature with moisture. As shown in Figure 3.17, positive linear correlations exist between the Langmuir volume and TOC for both dry samples at 25°C and wet samples at 60°C. However, wet samples of AC-2, AC-4, and AC-5 with low TOC (TOC ranges from 0.23 to 1.08%) have similar Langmuir volume at 60°C. This means that the role of organic matter in methane adsorption for low TOC sample is not critical due to the combined effect of high temperature and moisture. In this case, other parameters (clay content and pore structure) need to be considered in the determination of the Langmuir volume at high temperature with moisture. Compared with the dry samples at 25°C, correlation of Langmuir volume to TOC for the wet samples at 60°C has a lower slope of regression, which implies that the conditions (high temperature and presence of moisture) may restrain the contribution of organic matter to methane adsorption in shales.

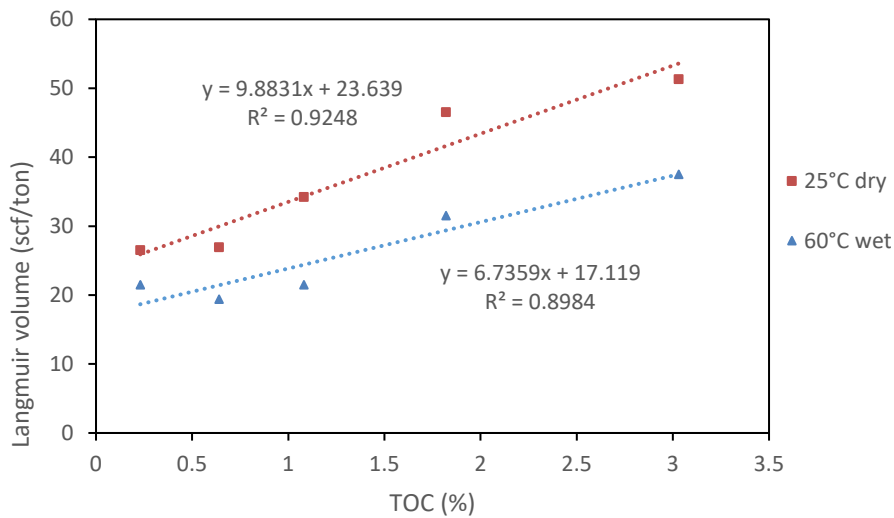


Figure 3.17 Correlation of Langmuir volume for dry samples at 25°C and wet samples at 60°C to TOC.

In addition, the reciprocal of Langmuir pressure can be used to describe the affinity of methane adsorption in shales. As shown in Table 3.2, Langmuir pressure increases with increasing temperature and moisture, which demonstrates that the increased temperature and presence of moisture lead to a weaker affinity for the methane adsorption in shales.

3.3.5 The combined effect of moisture and high temperature on methane adsorption in shales

The moisture and high temperature can reduce the methane adsorption in shales individually. However, the coexistence of these two factors can bring some joint effects. The moisture effect on methane adsorption in shales decreases with increasing temperatures. As shown in Figure 3.18, $V_{\text{reduction}}/V_{\text{dry}}$, used to quantify the moisture effect on methane adsorption, decreases with increasing temperature for all the studied samples. The range of $V_{\text{reduction}}/V_{\text{dry}}$ at maximum pressure for all samples at 25°C is 12% to 17%, while $V_{\text{reduction}}/V_{\text{dry}}$ at the maximum pressure at 60°C decreases to the range of 5% to 14%. Besides, the wet samples are less sensitive to the high temperature compared with the dry samples. The temperature effect on methane adsorption can be described by the decrease rate of methane adsorption capacity with increasing temperature. As shown in Figure 3.19, the decrease rate of Langmuir volume with increasing temperature for the dry samples is larger than the wet ones. The wet samples

have a decrease rate of Langmuir volume in the range of 0.09 to 0.27, while the decrease rate for the dry samples ranges from 0.13 to 0.4. Therefore, the effect of high temperature and moisture on methane adsorption in shales weakens each other.

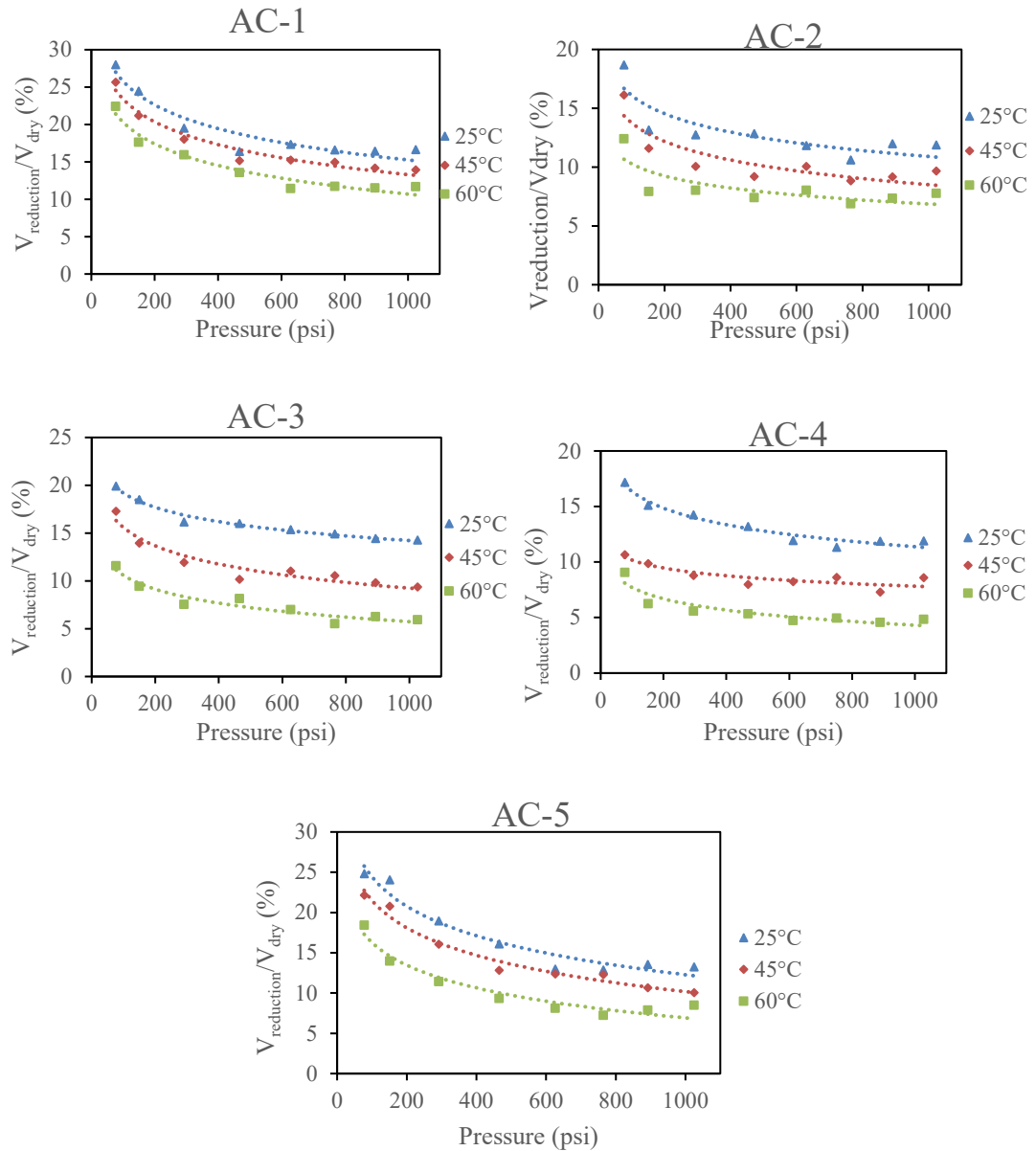


Figure 3.18 The reduced percentage of methane adsorption with moisture as a function of pressure at different temperatures.

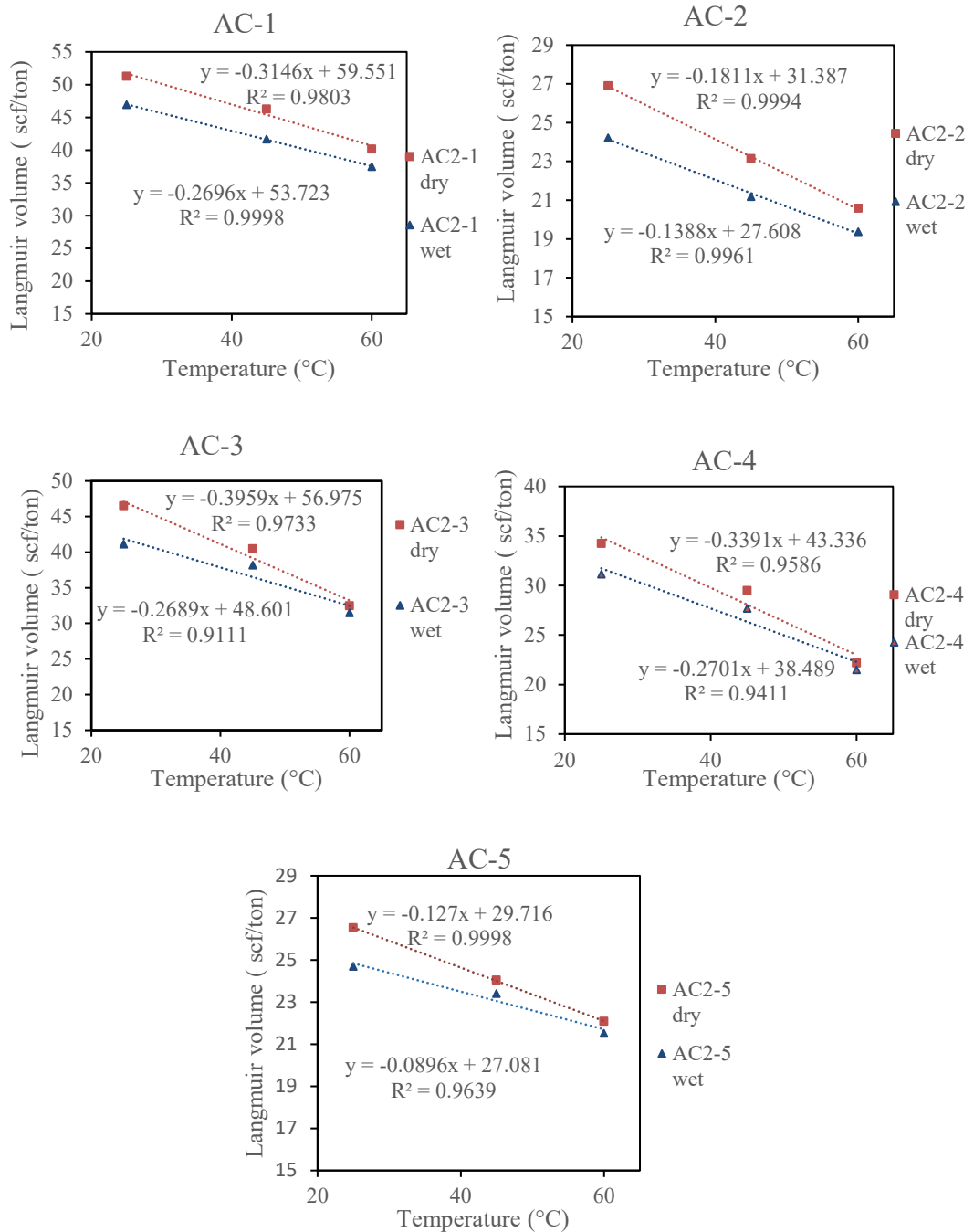


Figure 3.19 The decrease rate of Langmuir volume with increasing temperature for the dry and wet samples.

The phenomenon that moisture and high temperature effect weakens each other can be explained by their mechanisms of reducing methane adsorption in shales. As physical adsorption, methane adsorption in shales releases heat, which is restrained by the increased temperature. The increased temperature reduces the adsorbed methane on all sorption sites. Unlike the high temperature, moisture only reduces the adsorbed methane on the certain sorption sites, which are blocked or covered by adsorbed water

in shales (Li et al., 2016; Li et al., 2017). In this case, the possible reason for the moisture and high temperature weakening each other is that the two factors mainly influence the same part of adsorbed methane. In this work, the small pores are more sensitive to moisture than large pores. It might infer that the high temperature also primarily reduce adsorbed methane in the small pores.

3.3.6 Thermodynamic parameters

Thermodynamic parameters were calculated from the temperature dependence of the Langmuir pressure, including the heat of adsorption and the standard entropy of adsorption listed in Table 3.3.

Figure 3.20 shows that the heat of adsorption for the dry samples is positively related to the TOC. It has been reported that the process of methane adsorption on kerogen releases more heat than that on clay minerals (Ji et al., 2012; Zhang et al., 2013; Zhang et al., 2012). As for shale sample AC-2 and AC-5 with very low TOC in this study, a certain amount of methane adsorbed on clay minerals contributes to the low heat of adsorption. The heat of adsorption decreases with the increasing proportion of methane adsorbed on clay minerals. Moreover, the correlation coefficient is 0.83 in Figure 3.21, demonstrating that the heat of adsorption is not only related to the TOC.

The heat of adsorption determined for the dry shale samples in this work is ranging between 4.5 and 14.5 kJ/mol, which is smaller than the published results in Table 3.4 on kerogen, organic-rich shale and even Montmorillonite clay and I-S mixed clay (Gasparik et al., 2014; Ji et al., 2012; Zhang et al., 2013; Zhang et al., 2012). The reason could be: 1. the studied shale samples have low TOC (0.23~3.07%); 2. the particle size used in this study (<250 μm) is much coarser than the particle size of the Montmorillonite clay and I-S mixed clay in the literature <50 μm . It has been shown that the decreasing of particle size can change the pore size distribution of shale samples by crushing sample rock into powder, which leads to increased small pore and internal surface areas (Chen et al., 2015). The changed pore size distribution enhances the heat of methane adsorption (Myers, 2004).

After moisturizing, the heat of adsorption shows a decrease for each sample. Given that the dominant mechanism of moisture effect on methane adsorption is the blockage of small pores, the difference in the thermodynamic parameters between dry and wet

samples is attributed to the blocked small pores. The decrease in heat of adsorption after moisturizing illustrates that the heat of adsorption for the blocked small pores is larger than that of the whole sample. In this case, the larger heat of adsorption for the blocked small pores can be explained in two aspects: 1. methane adsorbed in small pores releases more heat than that in larger pores for the same composition (clay or kerogen) (Myers, 2004); 2. sorption sites on kerogen primarily distribute in small pores in shales, and kerogen is believed to have larger heat of adsorption than clay minerals (Ji et al., 2012; Zhang et al., 2012).

The entropy of adsorption reflects the restricted mobility of adsorbed molecules (Xia et al., 2006), which should be close to the loss of translational entropy from three-dimensional free gas to two-dimensional adsorbed gas (Xia and Tang, 2012). The dry samples have more negative entropy of adsorption than the wet ones, which indicates methane adsorbed in dry samples has less mobility than that in wet samples. The less mobility of adsorbed methane in wet samples is attributed to the blocked small pores by moisture. Methane adsorbed in small pores has less mobility than that in larger pores. It has been reported that methane adsorbed in small pores has a larger density than methane adsorbed in larger pores (Mosher et al., 2013).

Note that the difference in thermodynamic parameters between the dry and wet sample is striking for the studied samples except sample AC-3, which suggests that the thermodynamic parameters of the small pores blocked by moisture in sample AC-3 are similar to the parameters of the large pores. In addition, the standard entropy of adsorption for the dry samples is ranging between -42 and -74.7 Jmol⁻¹K⁻¹. Sample AC-2 and AC-5 with low TOC have less negative values, which indicates that methane molecules adsorbed on clay minerals have more mobility than methane molecules adsorbed on kerogen. The difference in mobility suggests different configurations of methane adsorbed on clay and kerogen. It is likely that methane adsorbed on clay minerals has a lower density than that on kerogen.

Table 3.3 Thermodynamic parameters of methane adsorption for the dry and wet shale samples.

		Heat of adsorption, q (kJmol ⁻¹)	Entropy of adsorption, Δs (Jmol ⁻¹ K ⁻¹)
AC-1	Dry	10.7	-58.5
	Wet	6.4	-46.6
AC-2	Dry	7.8	-49.7
	Wet	3.6	-37.0
AC-3	Dry	11.2	-62.1
	Wet	10.7	-61.4
AC-4	Dry	8.2	-55.6
	Wet	5.8	-48.4
AC-5	Dry	4.5	-42.0
	Wet	2.3	-36.9
T-5	Dry	14.5	-74.7

Table 3.4 Thermodynamic parameters of methane adsorption on different samples from published data.

	Heat of adsorption, q (kJmol ⁻¹)	Entropy of adsorption, Δs (Jmol ⁻¹ K ⁻¹)
Green river kerogen(type I) ^a	10.3	-49
Woodford Kerogen(type II) ^a	21.9	-81.1
Cameo coal(type III) ^a	28	-92.2
Green river rock ^a	15.1	-64.5
Woodford rock ^a	15.3	-57.2
Lee C-5-1 rock ^a	14	-56.9
Oxy Tarrant #A-3 rock ^a	7.3	-36.2
Blakely#1 rock ^a	18.4	-63.4
Montmorillonite clay ^b	16.6	-79.5
I-S mixed layer ^b	14.6	-77.2
Illite clay ^b	10.3	-65.3
Kaolinite clay ^b	9.6	-65.3
Chlorite ^b	9.4	-64.8

Note: ^a from Ross and Marc Bustin (2007) and Zhang et al.(2012) ^b from Ji et al.(2012)

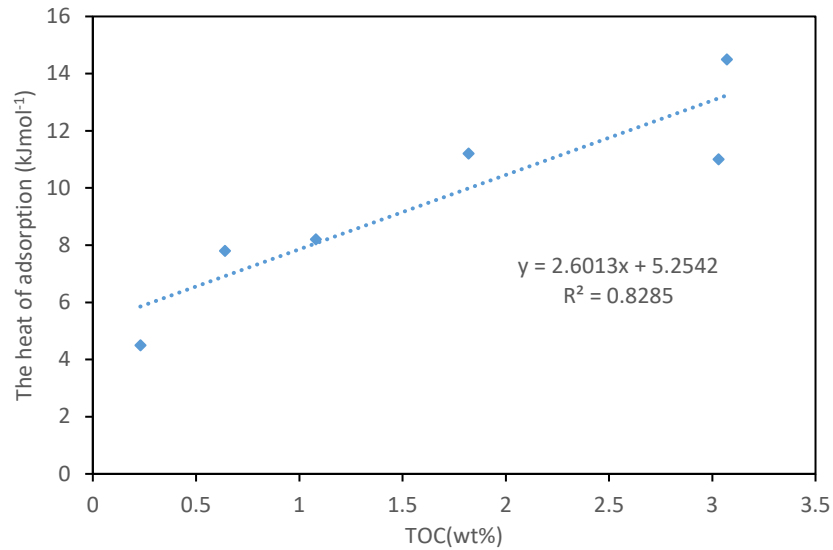


Figure 3.20 The correlation between the heat of adsorption and the TOC.

3.3.7 Estimation of methane adsorption in shales with moisture at a high temperature

This study has confirmed that methane adsorption capacity in shales is greatly reduced by the coexistence of high temperature and moisture which is real for the in-situ state of shale. To estimate the gas adsorption potential in shales under the actual condition, external parameters (temperature, pressure, and moisture) must be considered. Given the surface pressure (14.7psi) and temperature (23°C), the pressure and temperature of the studied samples at reservoir condition are determined using the pressure and temperature gradient in Table 3.5. In terms of moisture, we assume the moisture content for each sample is constant at all depths. Herein, the moisture content derived from relative humidity of 84% in this work is used. The methane adsorption isotherm of each sample at reservoir conditions is described by Langmuir parameters. The Langmuir pressure and Langmuir volume are calculated using the temperature dependence in Table 3.2. Based on the measured adsorption isotherms, the methane adsorption capacity (V(scf/ton)) under the actual reservoir condition was estimated. The results are listed in Table 3.5.

Table 3.5 Estimated methane adsorption capacity of shale samples under reservoir conditions.

	Pressure (psi)	Temperature (°C)	V _L (scf/ton)	P _L (psi)	v(scf/ton)
AC-1	4128	121	21.2	551.8	18.7
AC-2	4149	121	10.8	418.0	9.8
AC-3	4176	122	15.9	905.8	13.0
AC-4	4203	122	5.5	842.6	4.5
AC-5	4167	122	16.2	604.4	14.1

Note: the temperature gradient is 35.1°C/km; the pressure gradient is 1479.4 psi/km.

No correlations exist between the estimated methane adsorption capacity and the TOC under actual reservoir conditions considering the presence of moisture and high temperature. The methane adsorption capacity under actual reservoir conditions decreases in the following order: AC-1>AC-5>AC-3>AC-2>AC-4. Sample AC-4 with 1.08% TOC has the lowest methane adsorption capacity, while sample AC-5 with 0.23% TOC has large methane adsorption in reservoir condition. The two factors limit the contribution of organic matter to methane adsorption. Given the low TOC range of the studied samples, more data are required for shale samples with high TOC values.

3.4 Conclusion

- The effect of temperature on methane adsorption is different for shale samples with different compositions. Methane adsorption on kerogen is more sensitive to temperature increase than methane adsorption on clay minerals.
- Moisture leads to a shift to smaller sizes in PSD of big mesopores (16-50 nm) and macropores (>50 nm) from dry to wet sample due to the multilayers adsorbed water. The thickness of the multilayer adsorbed water can be generally determined from the half distance of the shift in PSD shape. No shift is observed in the PSD of fine mesopores (2 nm-16 nm) but a decrease in pore volume with moisture. As for micropores, all the studied samples show the decrease tendency in micropore volume, but the change in PSD shape for high TOC samples is not as obvious as that for low TOC samples.
- The effect of moisture on methane adsorption in shales is largest at low pressure. It decreases first and then keeps stable with increasing pressure. The moisture effect on methane adsorption in shales decreases with increasing pore

diameter: small pores like micropores can be thoroughly blocked by adsorbed water, but bigger pores like mesopores are less likely to be blocked.

- The effect of moisture on methane adsorption in shales is related to the TOC. For the high TOC samples, organic matter-hosted pores can be blocked by the water adsorbed in clay-hosted small pores. The reduction of the methane adsorption in low TOC samples with moisture is due to the blocked clay-hosted small pores.
- Wet samples have lower Langmuir volumes and larger Langmuir pressures than dry samples at experimental temperatures. Langmuir volume decreases and Langmuir pressure increases with increasing temperature for both dry and wet samples.
- Moisture and high temperature can reduce the methane adsorption in shales individually, and the two factors weaken each other for methane adsorption on shales. The moisture effect on methane adsorption in shales decreases with increasing temperature. The dry samples are more temperature sensitive than the wet samples. This phenomenon implies that both the increased temperature and moisture have a greater impact on the methane adsorption of small pores in shales.
- The heat of adsorption for the dry shale samples is lower than the results in the literature due to the lower TOC and coarser particle size. According to the standard entropy of adsorption, methane adsorbed on clay minerals has more mobility than methane adsorbed on kerogen, which indicates the different configurations between methane adsorbed on clay minerals and kerogen.
- The heat of adsorption shows a decreasing trend and the entropy of adsorption becomes less negative after moisturizing. The difference in thermodynamic parameters between the dry and wet samples is attributed to the blocking of small pores by moisture, illustrating that methane adsorbed in the blocked small pores release more heat and have less mobility than the methane adsorbed in the whole sample.

References

Chalmers, G.R.L. and Bustin, R.M., 2008. Lower Cretaceous gas shales in northeastern British Columbia, Part I: geological controls on methane sorption capacity. *Bulletin of Canadian Petroleum Geology*, 56(1): 1-21.

- Chen, Y., Wei, L., Mastalerz, M. and Schimmelmann, A., 2015. The effect of analytical particle size on gas adsorption porosimetry of shale. *International Journal of Coal Geology*, 138: 103-112.
- De Boer, J., 1958. The shape of capillaries. The structure and properties of porous materials: 68-92.
- Duan, Z., Møller, N., Greenberg, J. and Weare, J.H., 1992. The prediction of methane solubility in natural waters to high ionic strength from 0 to 250°C and from 0 to 1600 bar. *Geochimica et Cosmochimica Acta*, 56(4): 1451-1460.
- Fan, E., Shuheng Tang, Chenglong Zhang, Qiulei Guo and Sun, C., 2015 Methane sorption capacity of organics and clays in high-over matured shale-gas systems. *Energy, Exploration & Exploitation*, 32: 16.
- Gasparik, M., Bertier, P., Gensterblum, Y., Ghanizadeh, A., Krooss, B.M. and Littke, R., 2014. Geological controls on the methane storage capacity in organic-rich shales. *International Journal of Coal Geology*, 123: 34-51.
- Ji, L., Zhang, T., Milliken, K.L., Qu, J. and Zhang, X., 2012. Experimental investigation of main controls to methane adsorption in clay-rich rocks. *Applied Geochemistry*, 27(12): 2533-2545.
- Lastoskie, C., Gubbins, K.E. and Quirke, N., 1993. Pore size distribution analysis of microporous carbons: a density functional theory approach. *The Journal of Physical Chemistry*, 97(18): 4786-4796.
- Li, J., Li, X., Wang, X., Li, Y., Wu, K., Shi, J., Yang, L., Feng, D., Zhang, T. and Yu, P., 2016a. Water distribution characteristic and effect on methane adsorption capacity in shale clay. *International Journal of Coal Geology*, 159: 135-154.
- Li, J., Li, X., Wu, K., Feng, D., Zhang, T. and Zhang, Y., 2017. Thickness and stability of water film confined inside nanoslits and nanocapillaries of shale and clay. *International Journal of Coal Geology*, 179(Supplement C): 253-268.
- Li, J., Li, X., Wu, K., Wang, X., Shi, J., Yang, L., Zhang, H., Sun, Z., Wang, R. and Feng, D., 2016b. Water Sorption and Distribution Characteristics in Clay and Shale: Effect of Surface Force. *Energy & Fuels*, 30(11): 8863-8874.
- Ma, J. and Huang, Z., 2017. Experiments of methane gas solubility in formation water under high temperature and high pressure and their geological significance. *Australian Journal of Earth Sciences*, 64(3): 335-342.
- Mosher, K., He, J., Liu, Y., Rupp, E. and Wilcox, J., 2013. Molecular simulation of methane adsorption in micro- and mesoporous carbons with applications to

- coal and gas shale systems. *International Journal of Coal Geology*, 109–110: 36-44.
- Myers, A.L., 2004. Characterization of nanopores by standard enthalpy and entropy of adsorption of probe molecules. *Colloids and Surfaces A: Physicochemical and Engineering Aspects*, 241(1–3): 9-14.
- Ross, D.J.K. and Marc Bustin, R., 2007. Shale Gas Potential of the Lower Jurassic Gordondale Member, Northeastern British Columbia, Canada. *CSPG Bulletin*, 55(1): 25.
- Wang, L. and Yu, Q., 2016. The effect of moisture on the methane adsorption capacity of shales: A study case in the eastern Qaidam Basin in China. *Journal of Hydrology*, 542: 487-505.
- Xia, X., Litvinov, S. and Muhler, M., 2006. Consistent Approach to Adsorption Thermodynamics on Heterogeneous Surfaces Using Different Empirical Energy Distribution Models. *Langmuir*, 22(19): 8063-8070.
- Xia, X. and Tang, Y., 2012. Isotope fractionation of methane during natural gas flow with coupled diffusion and adsorption/desorption. *Geochimica et Cosmochimica Acta*, 77: 489-503.
- Zhang, T., Ellis, G.S., Ruppel, S.C., Milliken, K., Lewan, M. and Sun, X., 2013. Effect of Organic Matter Properties, Clay Mineral Type and Thermal Maturity on Gas Adsorption in Organic-Rich Shale Systems, *Unconventional Resources Technology Conference*, Denver, Colorado, 12-14 August 2013, pp. 1996-2001.
- Zhang, T., Ellis, G.S., Ruppel, S.C., Milliken, K. and Yang, R., 2012. Effect of organic-matter type and thermal maturity on methane adsorption in shale-gas systems. *Organic Geochemistry*, 47: 120-131.
- Zou, J., Rezaee, R. and Liu, K., 2017. Effect of Temperature on Methane Adsorption in Shale Gas Reservoirs. *Energy & Fuels*, 31(11): 12081-12092.

Chapter 4

Methane adsorption kinetics and diffusion in shale

4.1 Introduction

Mechanisms of gas transport in shales differs significantly from conventional gas reservoirs due to its complex geological properties and adsorbed gas content. Gas flow in shale is mainly controlled by gas diffusion, which can be characterized indirectly by adsorption kinetics. Thus, we investigated the adsorption kinetics on different shale samples at different temperatures and pressures. Gas diffusion parameters were determined by fitting data of adsorption rate using the bidisperse diffusion model. The proposed method offers an alternative to the gas desorption measurement for the gas flow parameters in shale if the desorption data is not available. In addition, the analysis of the adsorption rate can also give an insight into the process of gas adsorption.

4.2 Experiment results

A total of 5 shale samples were used to measure the adsorption kinetics in wet condition. Figure 4.1 shows the curves of methane adsorption rate for the studied samples at three pressure steps (10, 30 and 50 bars). The three pressure steps were chosen to improve the comparative results, as the curves of the adsorption rate under close pressures are similar. For all the curves of methane adsorption rate, the fractional uptake ($\frac{M_t}{M_\infty}$) increases strikingly at the initial time range and then becomes relatively stable in the later period.

4.3 Discussion

4.3.1 Pressure effect on methane adsorption rate

For all studied samples the methane adsorption rate shows a reduction with increasing pressure. As shown in Figure 4.1, the adsorption rate at low pressure is larger than that of high pressure. The negative relationship between methane adsorption rate and pressure in shale has been observed in previous works (Dang et al., 2017; Rani et al., 2018; Yuan et al., 2014). The phenomenon has been explained that gas molecule-

molecule collision is intensive at high pressure, which could lead to a slow gas adsorption (Rani et al., 2018). In addition, according to the pore-filling theory, gas first adsorbs in small pores and then move into bigger pores with increasing pressure. As the adsorption rate at low pressure is greater, it can be suggested that the methane adsorption process in small pores is faster than in large pores.

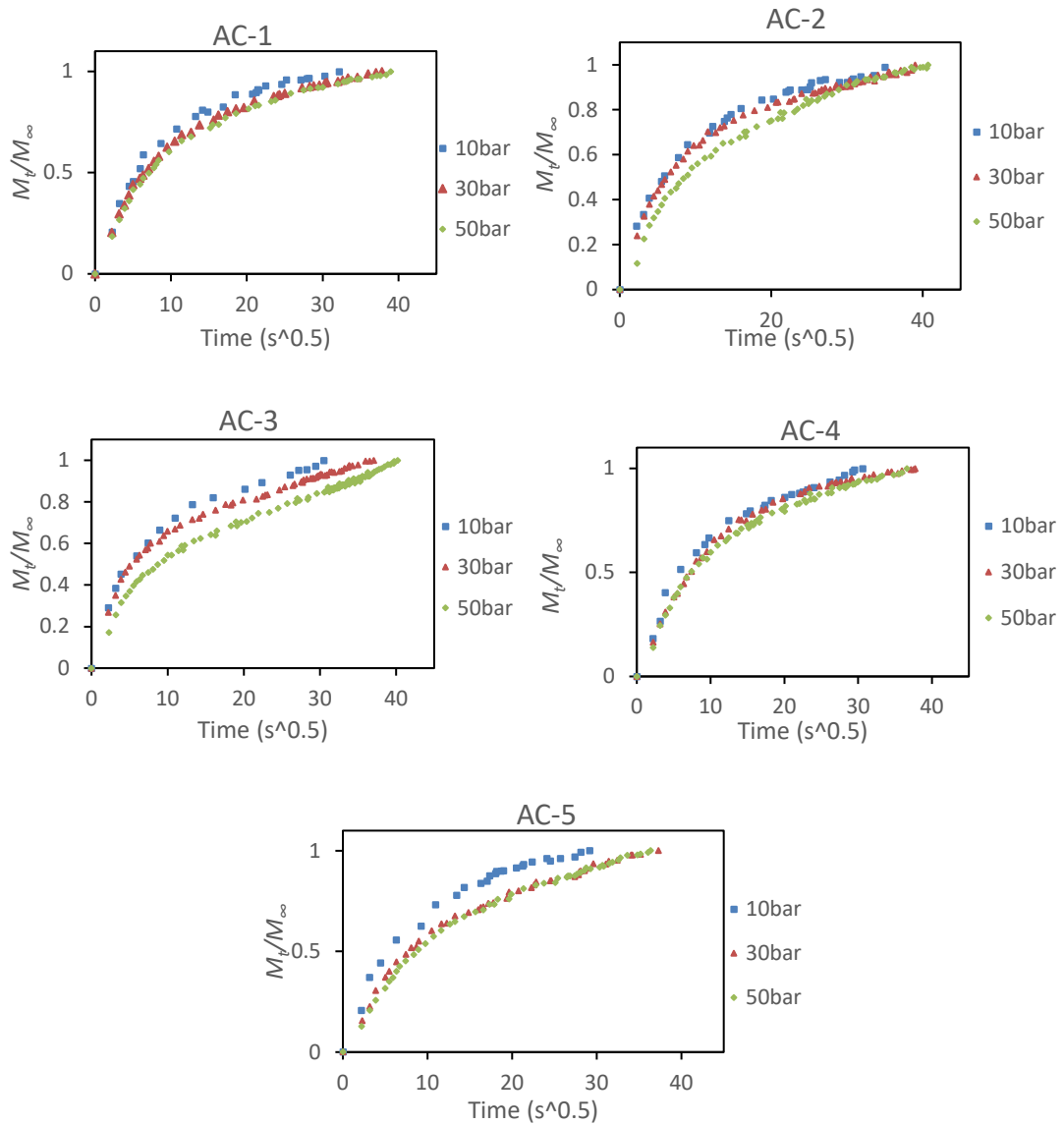


Figure 4.1 Methane adsorption rate at three pressure steps for the shale samples. The vertical axis is the fraction uptake and the horizontal axis is the square root of time ($\text{s}^{0.5}$).

4.3.2 Temperature effect on methane adsorption rate

Figure 4.2 shows the methane adsorption rate at different temperatures for sample AC-1 and AC-5. The methane adsorption rate (30bar) is greater at a higher temperature,

indicating the positive effect of temperature on the methane adsorption rate. It has been explained that gas molecules move faster in pore throats and have more collisions with the pore walls at high temperature, leading to a faster gas transport and adsorption (Wang et al., 2016).

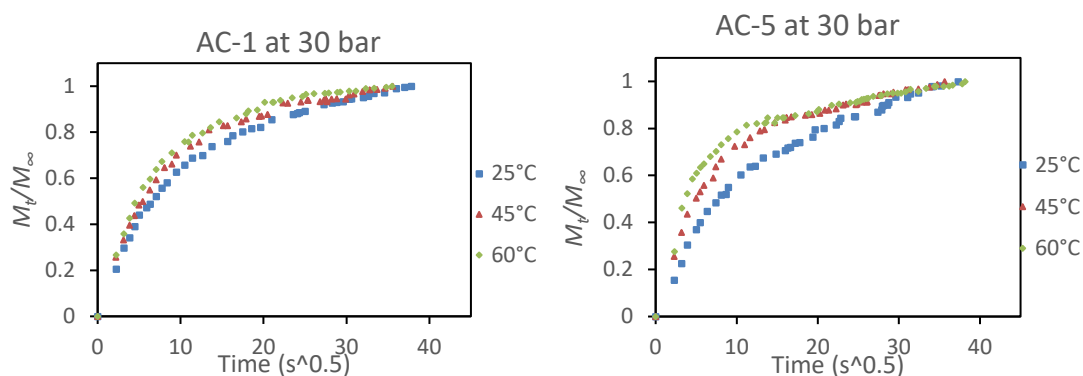


Figure 4.2 Methane adsorption rate under 30bar at three different temperatures for sample AC-1 and AC-5.

4.3.3 Comparison of methane adsorption rate between samples

We also compared the methane adsorption rate of different shale samples at the three pressure steps (10, 30 and 50bar). As the adsorption rate curves are very similar to each other, a quantifying method was used to calculate the slope of the curve in the initial time range, which is regarded as the linear portion of the adsorption rate curve. The time range chosen includes at least 4 time points above zero, so $6s^{0.5}$ was used in each determination of adsorption rate. Table 4.1 shows the slope of methane adsorption rate at 3 pressure steps for all the samples.

Figure 4.3 shows a good relationship between the TOC and slope of adsorption rate at 50bar, which indicates the organic matter contributes to the methane adsorption rate at high pressure. As for low pressure, the slope of adsorption rate at 10 and 30bar have no relation to the TOC. However, it can be seen in Figure 4.3 that a moderate positive relation exists between the slope of the adsorption rate at 30bar and micropore volume. It might be inferred that the sample with high micropore volume provides more surface area for adsorption and more throats for gas flow, which could lead to a great adsorption rate. Furthermore, the relations between the micropore volume and the slopes of the adsorption rate at 10 and 50bar are weak, indicating the effect of micropore volume on the adsorption rate is not consistent for different pressure steps.

In addition, no relation exists between the sum of the mesopore and macropore (<100nm) volume and adsorption rate at the three pressure steps. In a word, the controlling factors of methane adsorption rate are complex, and more parameters need to be studied.

Table 4.1 The slope of adsorption rate at three pressures for the shale samples.

	Slope, 10bar	Slope, 30bar	Slope 50bar
AC-1	0.093	0.086	0.08
AC-2	0.094	0.089	0.069
AC-3	0.105	0.1	0.074
AC-4	0.091	0.076	0.074
AC-5	0.091	0.074	0.064

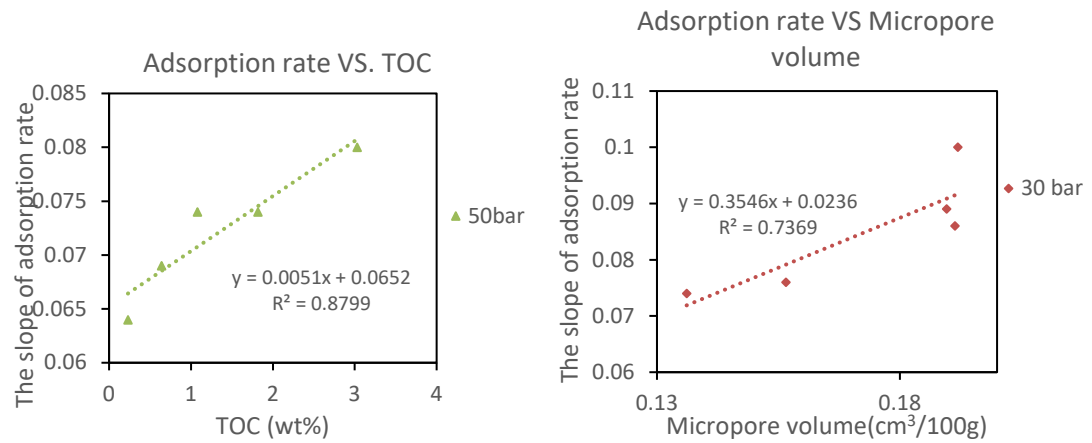


Figure 4.3 The relation of methane adsorption rate to TOC and micropore volume. The adsorption rate at 50 bar shows a good correlation with TOC; a moderate correlation exists between the adsorption rate at 30 bar and the micropore volume.

4.3.4 Diffusivity

The bidisperse diffusion model (see Chapter 2.3.5) was used to fit the methane adsorption rate for the shale samples (Figure 4.4). As shown, the bidisperse diffusion model gives a good match with the data of methane adsorption rate in shales. The fitting results provide the parameters of the bidisperse diffusion model in Tables 4.2 and 4.3, including $\frac{D_a'}{R_a^2}$ and $\frac{D_i'}{R_i^2}$. R_a , the macrosphere radius, could represent the mean particle radius of sample. As the samples were crushed to the same particle size (see Chapter 2.2.2), R_a is consistent for all the samples. As for R_i , it is believed that the

microsphere radius (R_i) is controlled by organic matter or clay minerals in shale. Herein, the shale samples are from the same formation of one borehole, so R_i is considered uniform for all the samples. Therefore, informative comparisons on effective diffusivities (D_a' and D_i') can be obtained from $\frac{D_a'}{R_a^2}$ and $\frac{D_i'}{R_i^2}$. Tables 4.2 and 4.3 show that $\frac{D_a'}{R_a^2}$ is larger than $\frac{D_i'}{R_i^2}$ for all the measurements, indicating that the macropore effective diffusivity (D_a') is much greater than the micropore effective diffusivity (D_i'), because the R_i is significantly smaller than the R_a . Therefore, gas diffusion in shale includes a faster macropore diffusion and a slower micropore diffusion.

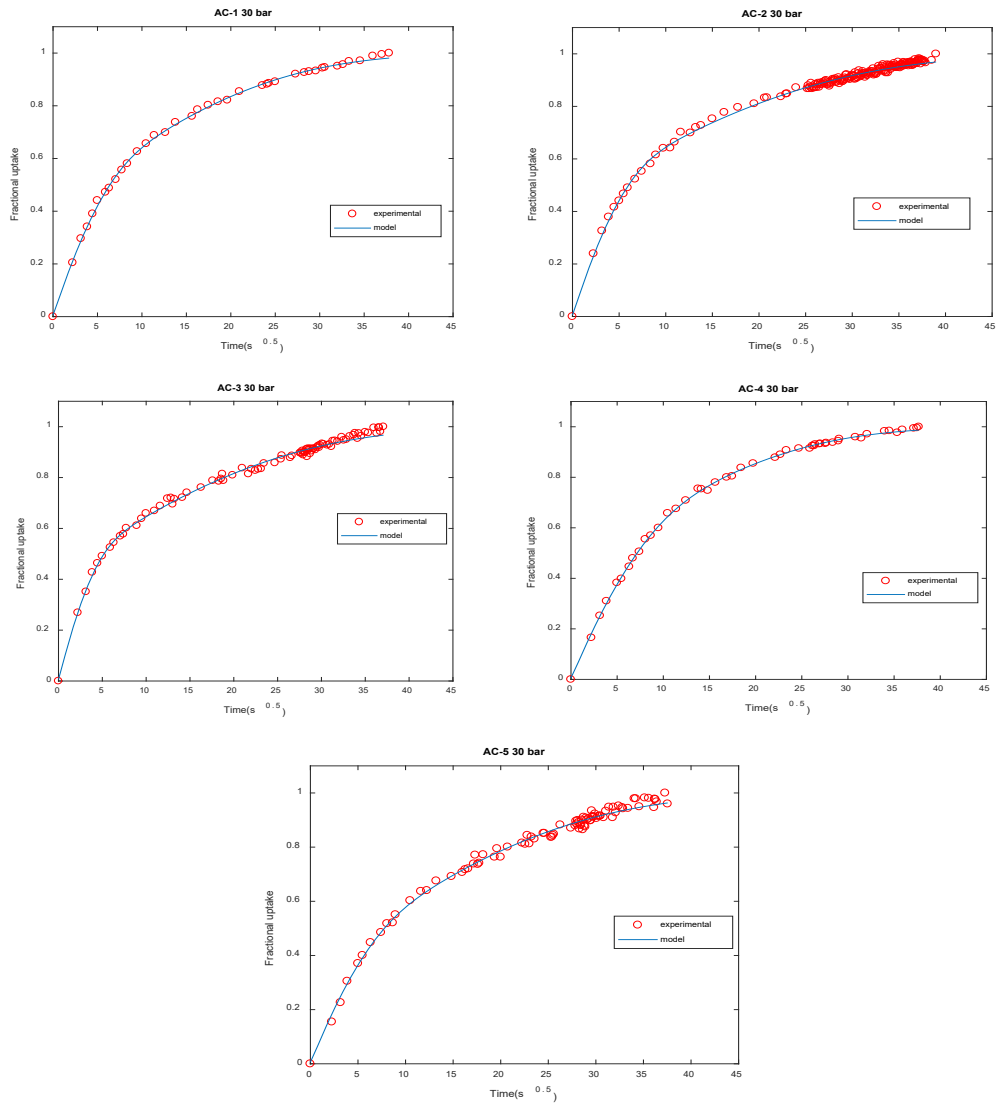


Figure 4.4 The methane adsorption rate at 30bar fitted using the bidisperse diffusion model for the shale samples.

$\frac{D_a'}{R_a^2}$ shows a decrease trend with pressure except for the 40bar of sample AC-1 and AC -3 (Table 4.2). For these two samples, the determined $\frac{D_a'}{R_a^2}$ at the pressure step of 40bar is larger than that at 30bar, which was also reported in the previous work (Cui et al., 2004; Dang et al., 2017). The decrease trend suggests a negative pressure effect on the macropore diffusivity. It has been explained that shale matrix could swell due to methane adsorption. The swelling narrows the pore throat and reduces the permeability (Rani et al., 2018). Even if no swelling exists in shale matrix, the increased adsorbed gas content with increasing pressure could tighten the path for gas transport as well (Li et al., 2016).

Table 4.3 displays that the $\frac{D_a'}{R_a^2}$ increases with increasing temperature for sample AC-1 and AC-5, while the $\frac{D_i'}{R_i^2}$ shows no obvious trend with increasing temperature, indicating limited temperature effect on the micropore effective diffusivity.

Table 4.2 Gas diffusion parameters from the bidisperse model for the shale samples at 25°C (using Equation 2.14 in Chapter 2.3.5).

Pressure(bar)	AC-1(25°C)			AC-2(25°C)			AC-3(25°C)		
	$\frac{D_a'}{R_a^2}$	$\frac{D_i'}{R_i^2}$	$\frac{\beta}{\alpha}$	$\frac{D_a'}{R_a^2}$	$\frac{D_i'}{R_i^2}$	$\frac{\beta}{\alpha}$	$\frac{D_a'}{R_a^2}$	$\frac{D_i'}{R_i^2}$	$\frac{\beta}{\alpha}$
10	0.0062	0.00029	4.6	0.00572	0.0002	4.3	0.0068	0.0002	3.5
20	0.0033	0.00025	5.5	0.00417	0.00021	4.2	0.0051	0.00026	4.6
30	0.0031	0.00020	4.5	0.00416	0.00020	4.2	0.0034	0.00017	10
40	0.0034	0.00021	10	0.00304	0.00024	8.1	0.0038	0.00015	13
50	0.0030	0.00019	5.3	0.00313	0.00017	8.3	0.0033	0.00012	15
	AC-4(25°C)			AC-5(25°C)					
	$\frac{D_a'}{R_a^2}$	$\frac{D_i'}{R_i^2}$	$\frac{\beta}{\alpha}$	$\frac{D_a'}{R_a^2}$	$\frac{D_i'}{R_i^2}$	$\frac{\beta}{\alpha}$			
10	0.0068	0.00028	5.8	0.00437	0.00034	6.3			
20	0.0040	0.00019	5.7	0.00344	0.00021	11			
30	0.0039	0.00025	5.0	0.00284	0.00017	6.3			
40	0.0043	0.00019	6.9	0.00225	0.00023	4.8			
50	0.0038	0.00019	8.6	0.00227	0.00019	8.9			

Table 4.3 Gas diffusion parameters from bidisperse model for sample AC3-1 and AC3-5 at 45 and 60°C (using Equation 2.14 in Chapter 2.3.5).

pressure(bar)	AC-1(45°C)			AC-1(60°C)		
	$\frac{D_a'}{R_a^2}$	$\frac{D_i'}{R_i^2}$	$\frac{\beta}{\alpha}$	$\frac{D_a'}{R_a^2}$	$\frac{D_i'}{R_i^2}$	$\frac{\beta}{\alpha}$
10	0.006456	0.00026	5.4	0.006766	0.00072	7.9
20	0.003905	0.00039	7.1	0.004035	0.00045	7.5
30	0.00364	0.00034	3.6	0.003936	0.00030	3.0
40	0.004434	0.00019	1.3	0.004309	0.00017	14
50	0.003626	0.00012	7.8	0.003848	0.00011	6.0
pressure(bar)	AC-5(45°C)			AC-5(60°C)		
	$\frac{D_a'}{R_a^2}$	$\frac{D_i'}{R_i^2}$	$\frac{\beta}{\alpha}$	$\frac{D_a'}{R_a^2}$	$\frac{D_i'}{R_i^2}$	$\frac{\beta}{\alpha}$
10	0.00474	0.00031	19	0.006154	0.00024	11.9
20	0.004236	0.00028	2.5	0.005713	0.00028	2.4
30	0.002956	0.00016	2.0	0.003323	0.00014	2.4
40	0.003802	0.00025	3.2	0.002843	0.00016	3.4
50	0.002828	0.00024	3.3	0.002893	0.00016	6.4

As the macropore effective diffusivity is much larger than the micropore effective diffusivity, the $\frac{D_a'}{R_a^2}$ is compared among all the shale samples. Fig 4.5 shows that TOC has a weak positive relationship with $\frac{D_a'}{R_a^2}$ at 10bar, while a strong positive relation exists between the $\frac{D_a'}{R_a^2}$ at 10bar and micropore volume. This phenomenon demonstrates that the contribution of micropore volume to the macropore effective diffusivity is more significant than the TOC. Sample AC-2 with low TOC but large micropore volume has a great macropore effective diffusivity. It might be implied that the larger micropore volume offers more available void space for gas diffusion. However, the sum of the mesopore and macropore (<100nm) volume shows no relationship with the $\frac{D_a'}{R_a^2}$ at 10 and 50bar (Figure 4.6), indicating the pores in the range of 2 to 100nm have little contribution to the macropore effective diffusivity. Therefore, the diffusion at low pressure in shale is mainly controlled by micropores rather than mesopores and macropores.

Herein, a hypothetic pore model is proposed in Figure 4.7. Pores in shale play different roles in gas transport and storage: micropore connected with mesopore or macropore dominates the diffusion as a throat; mesopore or macropore is related to gas storage sites but not for diffusion. The hypothetic pore model in shale could explain the different relations of the macropore effective diffusivity to the micropore volume and the sum of the mesopore and macropore (<100nm) volume, but more investigations are necessary to verify the model.

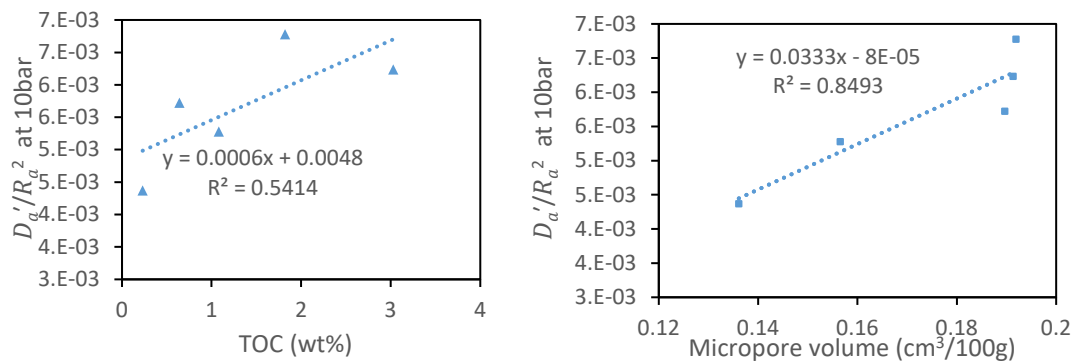


Figure 4.5 The relation of $\frac{D_a'}{R_a^2}$ at 10bar to the TOC and micropore volume for the shale samples.

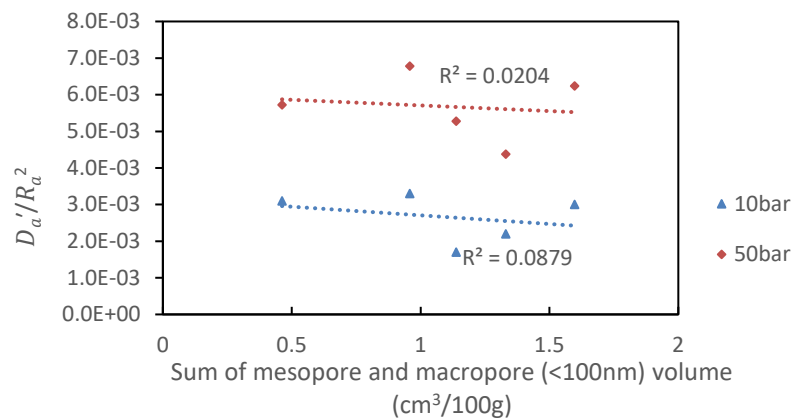


Figure 4.6 The relations of $\frac{D_a'}{R_a^2}$ at 10 and 50bar to the sum of mesopore and macropore (<100nm) volume.

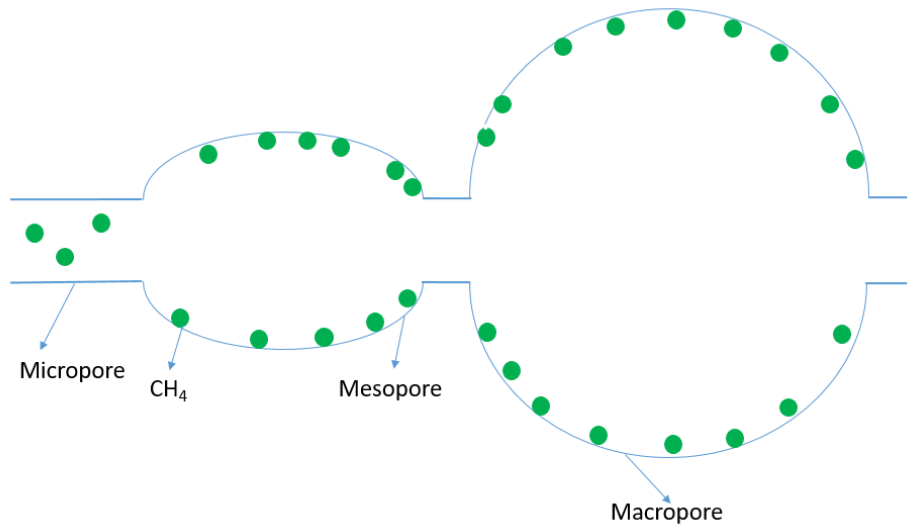


Figure 4.7 A hypothetical pore model in shale: micropore is not in fact a pore but it plays the role of the throat and contributes to the diffusion.

It is worth mentioning that macropore and micropore diffusivity are not discussed in this study. For the determination of the macropore and micropore diffusivity in the bidisperse model, pore structure parameters are needed to be known, including porosity and specific surface area for both micropore and macropore. However, these parameters are unobtainable, as it is hard to distinguish the micropore and macropore precisely.

4.4 Conclusion

The methane adsorption kinetics and diffusion of 5 shale samples from the Perth Basin in Western Australia were studied. The methane adsorption rate was measured experimentally and the effective diffusivities were fitted using a bidisperse diffusion model. The major conclusions are as follows:

- Pressure has a negative effect on methane adsorption rate, while temperature can positively affect the adsorption rate. Methane adsorption rate shows a positive relationship with TOC at high pressure (50bar) and the micropore volume is positively related to the methane adsorption rate at 30 bar.
- The relationship between TOC and the macropore effective diffusivity at low pressure (10bar) is positive but weak, while micropore volume from low-pressure CO₂ adsorption displays a good positive relation with the macropore effective diffusivity at low pressure (10bar). However, no relation was found

between the sum volume of mesopores and macropores (<100nm) and the macropore effective diffusivity.

- A hypothetical pore model is proposed to explain the effect of pores on diffusion in shale: micropore controls the effective diffusivity as a throat, while mesopore or macropore (<100nm) has limited contribution to the diffusion.
- These findings highlight that the micropores in shales need to be redefined as pore throats that connect pores rather than to play as a pore itself.

References

- Cui, X., Bustin, R.M. and Dipple, G., 2004. Selective transport of CO₂, CH₄, and N₂ in coals: insights from modeling of experimental gas adsorption data. *Fuel*, 83(3): 293-303.
- Dang, W., Zhang, J., Wei, X., Tang, X., Wang, C., Chen, Q. and Lei, Y., 2017. Methane Adsorption Rate and Diffusion Characteristics in Marine Shale Samples from Yangtze Platform, South China. *Energies*, 10(5): 626.
- Li, Z.-Z., Min, T., Kang, Q., He, Y.-L. and Tao, W.-Q., 2016. Investigation of methane adsorption and its effect on gas transport in shale matrix through microscale and mesoscale simulations. *International Journal of Heat and Mass Transfer*, 98: 675-686.
- Rani, S., Prusty, B.K. and Pal, S.K., 2018. Adsorption kinetics and diffusion modeling of CH₄ and CO₂ in Indian shales. *Fuel*, 216: 61-70.
- Wang, J., Wang, B.e., Li, Y., Yang, Z., Gong, H. and Dong, M., 2016. Measurement of dynamic adsorption–diffusion process of methane in shale. *Fuel*, 172: 37-48.
- Yuan, W., Pan, Z., Li, X., Yang, Y., Zhao, C., Connell, L.D., Li, S. and He, J., 2014. Experimental study and modelling of methane adsorption and diffusion in shale. *Fuel*, 117: 509-519.

Chapter 5

A prediction model for methane adsorption capacity of shales

5.1 Introduction

The methane adsorption capacity of shale samples at a certain pressure can be predicted using the Langmuir parameters. Thus, it is necessary to have a quantitative model of the Langmuir parameters for evaluating the methane adsorption capacity in shales. However, the Langmuir parameters are controlled by various factors (Gasparik et al., 2014a). It has been reported that the Langmuir volume is related to the compositional properties (total organic content, thermal maturity, and clay minerals content), pore structure properties (specific surface area and micropore volume) and reservoir conditions (pressure, temperature and moisture content) (Dang et al., 2017; Guo, 2013; Ji et al., 2012; Zhang et al., 2013). As for the Langmuir pressure, the most considered controlling factor is temperature, but it was also observed that the Langmuir pressure is related to composition and volume of small pores (Ji et al., 2012; Myers, 2004; Zhang et al., 2012). Furthermore, a power-law decrease trend was found between the Langmuir pressure and Vitrinite Reflectance (Gasparik et al., 2014a). Based on the controlling factors of the Langmuir parameters, prediction models for the methane adsorption capacity of shale gas have been proposed by many scholars (Li et al., 2017; Liu et al., 2017; Zhang et al., 2012). As listed in Table 5.1, however, the considered factors in the models are different. In terms of the Langmuir volume, TOC is the only factor for organic-rich shales. Liu et al. (2017) also considered TOC and clay content. Li et al. (2017) used other parameters in the model, such as the amount of residual hydrocarbon and temperature to improve accuracy. Zhang et al. (2012) classified the shales in terms of thermal maturity and expressed the Langmuir pressure as a function of temperature. Temperature is the only considered factor in the model of the Langmuir pressure by Liu et al. (2017), while the content of clay minerals, illite, feldspar, and carbonate was used by Li et al. (2017). However, some of the relevant parameters are hard to obtain from conventional well-logs, such as the contents of

residual hydrocarbons, illite, feldspar, and carbonate. Furthermore, the prediction models of methane adsorption capacity in previous studies were established on insufficient data or data from specific basins. To assess the methane adsorption capacity in shales, it is required to establish a prediction model based on representative data and proper factors.

Table 5.1 Factors considered in the prediction model for Langmuir parameters in previous studies.

	Langmuir volume	Langmuir pressure
Zhang et al. (2012)	TOC	temperature and thermal maturity
Liu et al. (2017)	TOC and clay content	temperature
Li et al. (2017)	TOC, clay content, temperature and residual of hydrocarbon (s_1)	the content of clay minerals, illite, feldspar, and carbonate minerals

In this chapter, we analyzed the controlling factors of methane adsorption capacity in shales and built a prediction model based on high-pressure methane adsorption data measured in our lab and some data from the literature (Appendix I). Given that the experimental temperatures are not constant, the Langmuir parameters were modeled at experimental temperature first and then the temperature dependence of Langmuir parameters was explored. The models can contribute to the understanding and evaluation of the methane adsorption in shales.

5.2 Results

Since the adsorption isotherms of the shale samples were measured at different temperatures and the amount of data at each high temperature is limited, a model of the Langmuir volume at an experimental temperature of 30°C was considered first. Experimental isotherms determined in the range of 25-30°C were considered similar due to the small temperature difference. In a second step, the model was updated for the methane adsorption under actual reservoir conditions, at higher reservoir temperature.

5.2.1 Model of Langmuir volume at experimental temperature

As the collected adsorption data of 10 samples are not available at experimental temperature, a total of 56 samples from 5 basins were studied for the model of Langmuir volume at experimental temperature. Figure 5.1 shows the positive relationship between the TOC and Langmuir volume at experimental temperature, with a coefficient of determination of 0.87, indicating the critical role of organic matter in methane adsorption in shales. However, more data are still required as a limited number of shale samples in the TOC range of 10 to 25 wt% exists in Figure 5.1.

Compared to the TOC, clay content appears to have a much lesser influence on the Langmuir volume (Figure 5.2), demonstrating a limited contribution to the methane adsorption. However, it has been reported that the contribution of clay minerals to methane adsorption is significant for low TOC shale samples (Fan et al., 2015; Ji et al., 2012). To explore the effect of clay on methane adsorption in shales, the samples studied were classified into three groups of low (0-1.5%), medium (1.5-3%), and high (>3%) based on the TOC content.

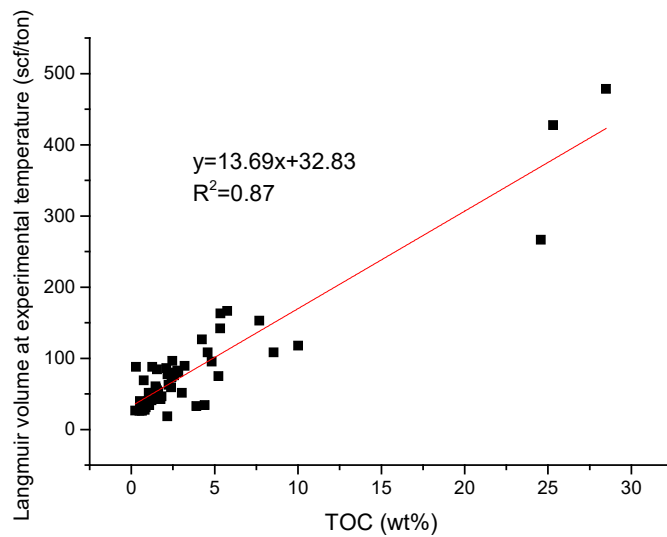


Figure 5.1 The relationship between the TOC and Langmuir volume at experimental temperature for the shale samples studied.

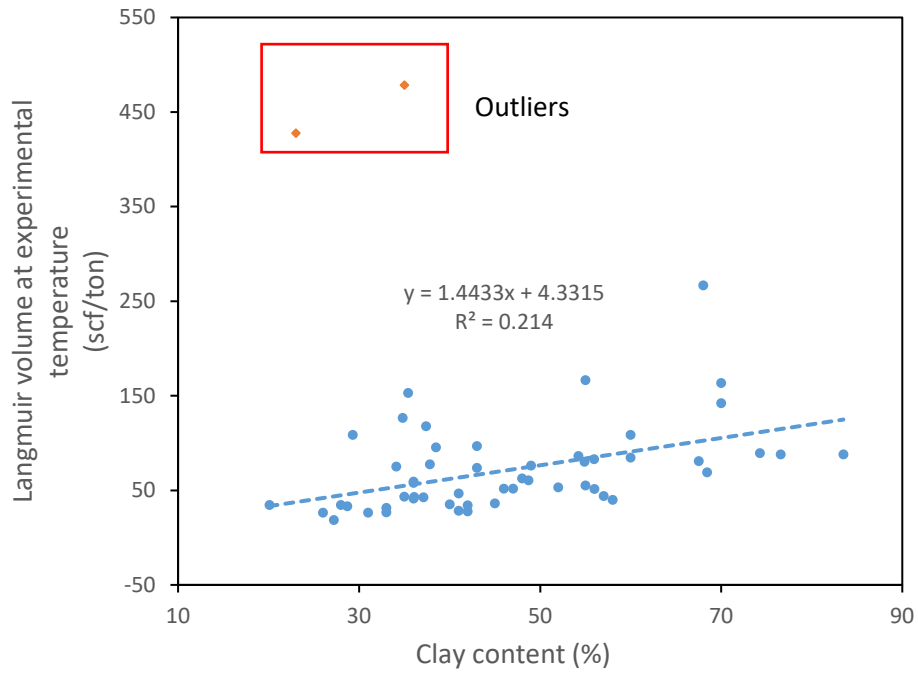


Figure 5.2 A weak relationship exists between the clay content and Langmuir volume at experimental temperature for the studied shale samples.

As for the clay content, Figure 5.3 displays a good relationship between the clay content and Langmuir volume at experimental temperature for the low TOC (0-1.5% TOC) samples but not for medium and high TOC samples. The phenomenon demonstrates that the clay content is the critical controlling factor of methane adsorption for low TOC shales, while its effect weakens in higher TOC samples due to the organic matter. Furthermore, the slopes of the relationship between the clay content and Langmuir volume at experimental temperature for the three groups of shales have no big difference, with the range of 1 to 1.73. The similarity of the slopes indicates that there is no remarkable difference between organic-poor and organic-rich shales with respect to the adsorption capacity of clay minerals. Note that the type of clay minerals was not specified for their relationship to Langmuir volume. The reason is that the content of each clay type is hard to obtain directly from well-logs and illite dominates the clay content for this data set.

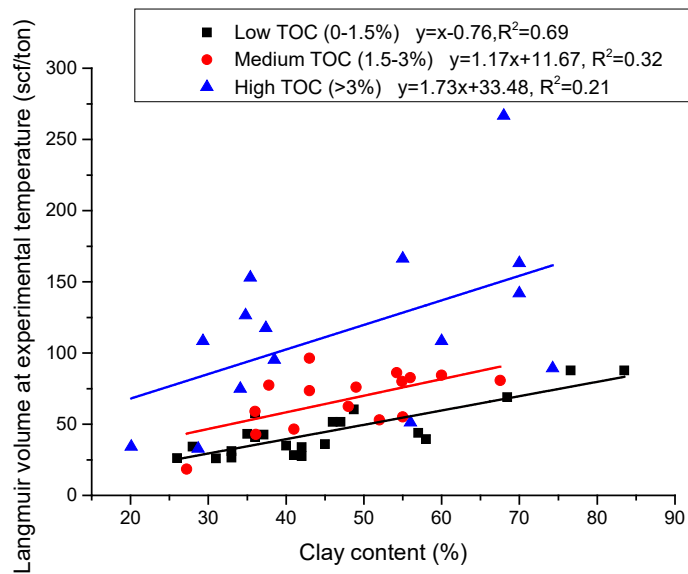


Figure 5.3 The relationship between the clay content and Langmuir volume at experimental temperature for low, medium and high TOC shale samples.

Apart from the TOC and clay content, thermal maturity is also believed to control the methane adsorption in shales. It has been reported that the relationship between the TOC-normalized maximum methane adsorption capacity (Langmuir volume divided by the TOC) and thermal maturity is positive for mature shales and negative for over mature shales (Gasparik et al., 2014a; Zhang et al., 2012). However, the thermal maturity in terms of T_{max} displays no relationship to the TOC-normalized Langmuir volume at experimental temperature for the collected data (Figure 5.4). The phenomenon could be due to the fact that the TOC-normalized Langmuir volume may be influenced by clay content, especially for the low TOC shale, and other factors such as kerogen type and thermal maturity levels may have impacts on methane adsorption capacity. Therefore, the thermal maturity is not considered in the model of the Langmuir volume at experimental temperature.

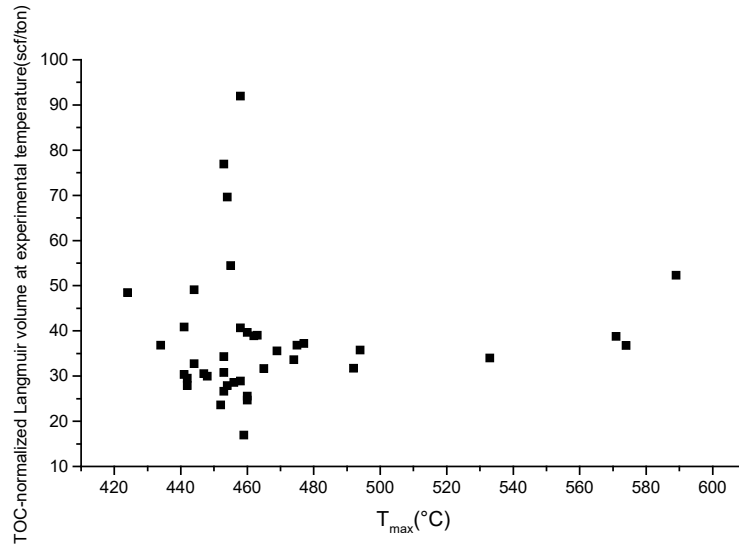


Figure 5.4 There is no meaningful relationship between the TOC-normalized Langmuir volume at experimental temperature and T_{max} for the shale samples studied.

Given the Langmuir volume at experimental temperature, TOC and clay content in this study, a multiple linear regression was carried out to derive a model for the Langmuir volume at the experimental temperature. The regression, using the 56 data sets, yielded the following regression:

$$V_L = 13.87TOC + 0.79V_{sh} - 4 \quad \text{Equation 5.1}$$

By determining the coefficients in the following equation:

$$V_L = a \times TOC + b \times V_{sh} + c \quad \text{Equation 5.2}$$

where a , b and c are the fitting coefficients, which can be determined using the 56 studied samples in by multiple linear regression; here V_L is the Langmuir volume at experimental temperature, scf/ton; TOC is the total organic carbon, wt%; V_{sh} is the total clay content, %.

The predicted versus measured Langmuir volume values at experimental temperature plotted in Figure 5.5 shows a good correlation.

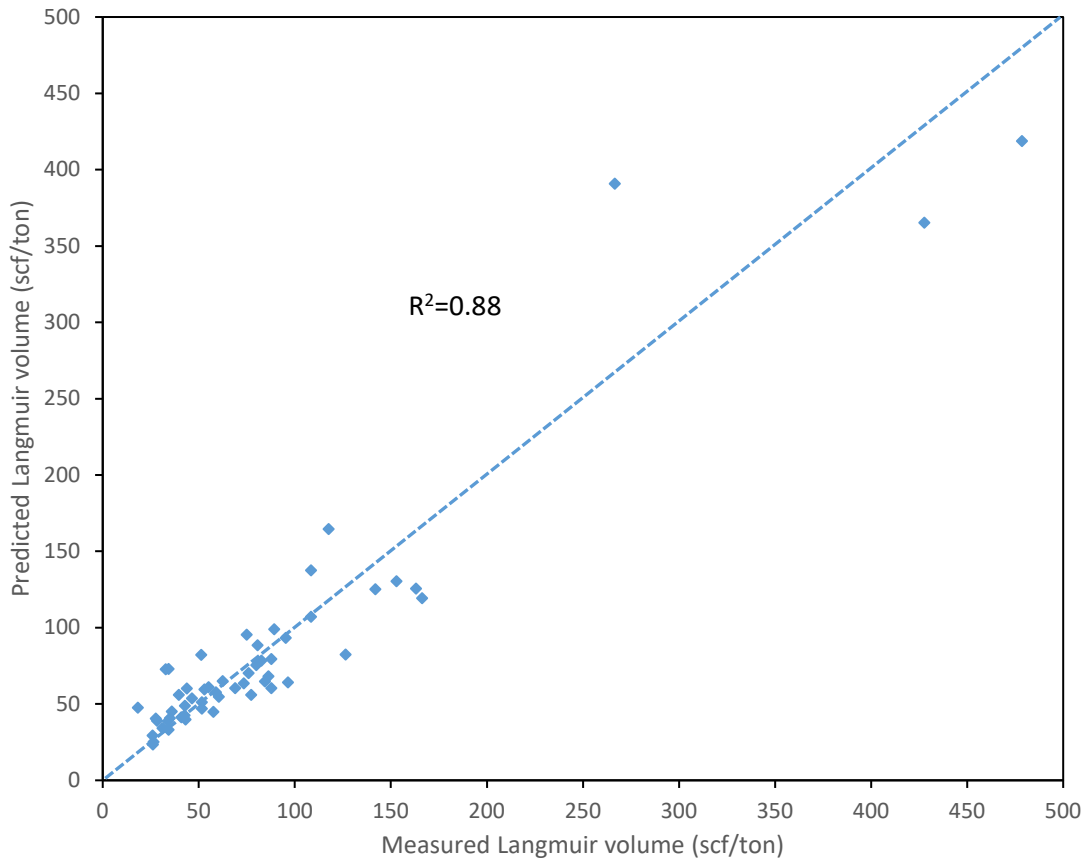


Figure 5.5 The relationship between the measured and predicted Langmuir volume at experimental temperature.

5.2.2 Model of Langmuir volume at reservoir temperature

As the methane adsorption in shale is an exothermic process, the methane adsorption capacity is reduced at a higher temperature. It has been observed that the Langmuir volume decreases with increasing temperature (Guo, 2013; Ji et al., 2015). A linear negative correlation exists between the Langmuir volume and temperature, which can be written in the following equation:

$$V_L(T) = -dT + e \quad \text{Equation 5.3}$$

Where $V_L(T)$ is the Langmuir volume at reservoir temperature, scf/ton; T is the reservoir temperature, °C; d and e are the fitting coefficients. The value of the trend-line slope, d , is denoted as decrease rate of Langmuir volume with increasing temperature, which quantitatively describes the decrease of Langmuir volume with temperature. It has been shown that methane adsorption on the organic matter is more sensitive to the temperature than methane adsorption on the minerals (Ji et al., 2012).

The finding is also confirmed in Figure 5.6, which displays a positive relationship between the TOC and decrease rate of V_L , with an R^2 of 0.58. With this relationship, the decrease rate of V_L (d) can be calculated based on the TOC using Equation 5.4:

$$d = 0.35\text{TOC} - 0.05 \text{ (scf/ton/}^\circ\text{C)} \quad \text{Equation 5.4}$$

Given that the Langmuir volume at experimental temperature discussed in last section, the Langmuir volume at reservoir temperatures can be estimated using the decrease rate of V_L or the d value from Equation 5.4. Thus, the Langmuir volume at reservoir temperature can be written as:

$$\frac{V_L(T) - V_{L0}}{T - T_0} = -d \quad \text{Equation 5.5}$$

By rearrangement:

$$V_L(T) = [13.87\text{TOC} + 0.79V_{sh} - 4] - (T - T_0)(0.35\text{TOC} - 0.05) \quad \text{Equation 5.6}$$

where $V_L(T)$ is the Langmuir volume at reservoir temperature, scf/ton; T is the reservoir temperature, $^\circ\text{C}$; T_0 is the experimental temperature, $^\circ\text{C}$; TOC is the total organic carbon, wt%; V_{sh} is the total clay content, %.

As the available data for the temperature dependence of Langmuir volume cover only a TOC range from 0.23 to 5.15 wt%, the result here may not be reliable for shales with larger TOC. Moreover, the samples with the TOC range of 3.03 to 5.15 wt% have a larger variation on the relationship than low TOC samples. Therefore, more data are required for the shale samples with TOC larger than 3.03 wt% in terms of the temperature dependence of Langmuir volume.

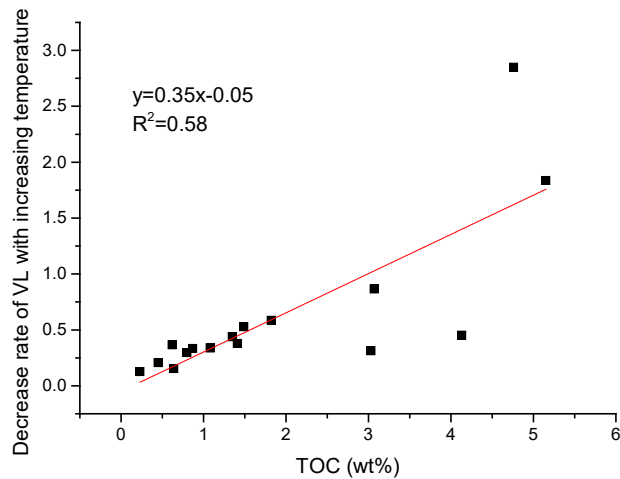


Figure 5.6 The relationship between the TOC and decrease rate of Langmuir volume with increasing temperature.

5.2.3 Model of Langmuir pressure at experimental temperature and reservoir temperature

Langmuir pressure is also required to calculate the methane adsorption capacity in actual reservoir conditions. The reciprocal of the Langmuir pressure represents the affinity of the gas for sorbent. It has been concluded that the adsorption affinity on the organic matter is stronger than that on clay minerals (Ji et al., 2012). Thermal maturity and volume of small pores were also regarded as controlling factors of the Langmuir pressure (Gasparik et al., 2014a; Myers, 2004). In the present study, the Langmuir pressure shows no trend with the thermal maturity, TOC or clay content, but a logarithmic-law trend exists in the Langmuir volume, with R^2 of 0.31 (Figure 5.7). The poor correlation might result from the sensitive and various controlling factors of the Langmuir pressure. The shale sample with a large Langmuir volume has a high Langmuir pressure, which represents a weak adsorption affinity of methane. As reported, the organic matter and small pore have stronger adsorption affinity of methane compared to the clay and large pore, respectively. In this case, the adsorption affinity of methane in shale reflects the proportion of adsorbed methane in small pore and organic matter. Thus, the weak adsorption affinity in the shale sample with a large Langmuir volume might infer that the proportion of adsorbed methane in the small pore and organic matter is low. Since the relationship between the Langmuir volume and Langmuir pressure is obtained from a large amount of data, the relationship can

be informative. Therefore, the Langmuir pressure can be predicted using the following equation:

$$P_L = 93.8 \ln(V_L - 9.3) \quad \text{Equation 5.7}$$

where P_L and V_L are the Langmuir pressure and Langmuir volume at experimental temperature in psi and scf/ton, respectively.

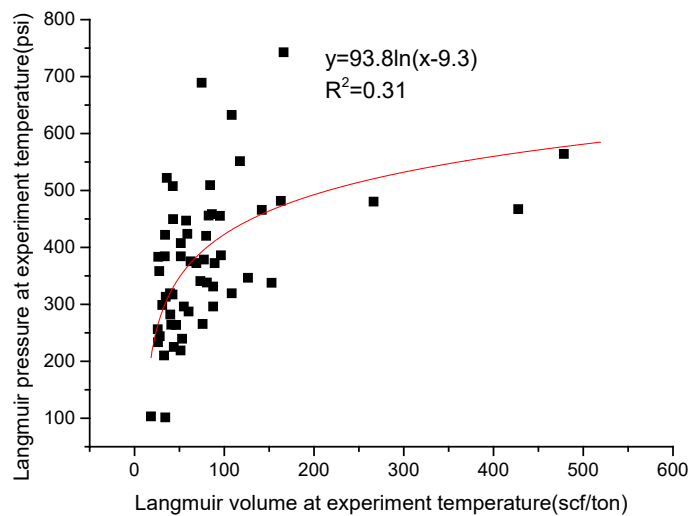


Figure 5.7 The relationship between the Langmuir pressure and Langmuir volume at experimental temperature for the samples studied.

The temperature dependence of the Langmuir pressure has been described by the following equation (Xia et al., 2006):

$$\ln\left(\frac{1}{P_L}\right) = \frac{m}{T+273} + n \quad \text{Equation 5.8}$$

Where m and n are the fitting coefficients, resulting from the thermodynamic parameters: the heat of adsorption and the standard entropy of adsorption. These parameters have been compared between the organic matter and clay minerals, concluding that the enthalpy of adsorption of methane on organic matter is higher than its enthalpy of adsorption on clay. A linear relationship between the heat of adsorption and the standard entropy of adsorption has been proposed for different types of kerogen, clay and shale samples at different thermal maturity (Gasparik et al., 2014a). It might imply that the thermodynamic parameters are related to the TOC. For each shale sample, the coefficients m and n are determined using a linear fit between $\ln\left(\frac{1}{P_L}\right)$

and $\frac{1}{T+273}$. In terms of the samples studied, the plot of m with TOC is shown in Figure 5.8 as the following equation:

$$m = 1215.3\text{TOC}^{0.179} \quad \text{Equation 5.9}$$

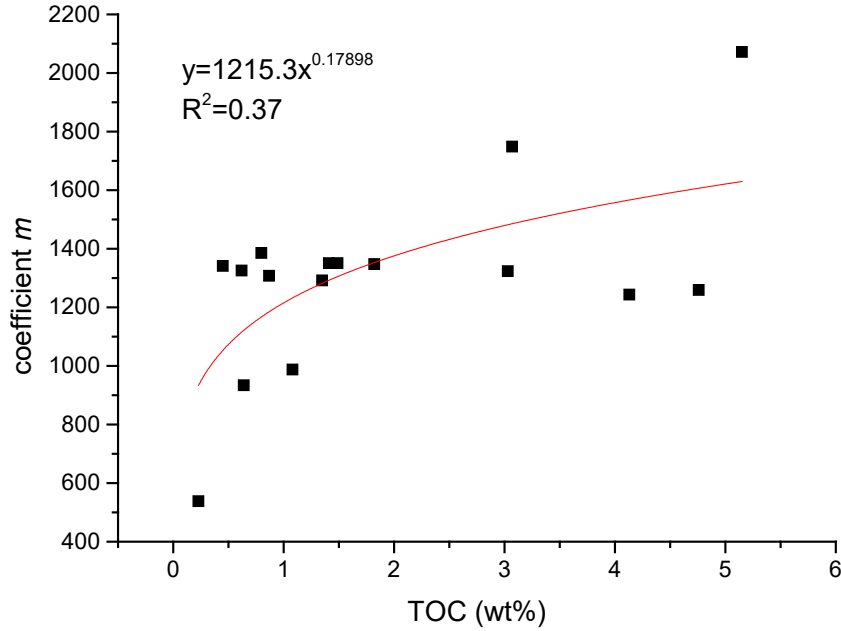


Figure 5.8 The relationship between the fitting coefficient m and the TOC.

Combined with the prediction model for the Langmuir pressure at experimental temperature, the Langmuir pressure at reservoir temperature ($P_{L(T)}$) can be obtained using the following equations:

$$\ln\left(\frac{P_L(T)}{P_L}\right) = m\left(\frac{1}{T_0+273} - \frac{1}{T+273}\right) \quad \text{Equation 5.10}$$

$$P_L(T) = P_L \times e^{(1215.3\text{TOC}^{0.179}) \times \left(\frac{1}{T_0+273} - \frac{1}{T+273}\right)} \quad \text{Equation 5.11}$$

$$P_L(T) = 93.8 \ln(13.87\text{TOC} + 0.79V_{sh} - 13.3) \times e^{(1215.3\text{TOC}^{0.179}) \times \left(\frac{1}{T_0+273} - \frac{1}{T+273}\right)} \quad \text{Equation 5.12}$$

where m is the fitting coefficient in Equation 5.8; T_0 is the experimental temperature, °C; T is the reservoir temperature, °C.

Therefore, the methane adsorption capacity at a certain pressure and temperature can be estimated by the Langmuir model, Equation 5.13:

$$gc(T, P) = \frac{V_L(T) \times P}{P_L(T) + P} \quad \text{Equation 5.13}$$

where $gc(T)$ is the adsorbed amount of gas at certain temperature and pressure, scf/ton; $V_L(T)$ is the Langmuir volume at reservoir temperature, scf/ton; $P_L(T)$ is the Langmuir pressure at reservoir temperature, psi; P is the reservoir pore pressure, psi.

5.3 Discussion and conclusions

In this chapter, we proposed a prediction model for the methane adsorption capacity in shales based on the results of high-pressure methane adsorption experiments. The methane adsorption capacity at certain pressure and temperature can be estimated using the Langmuir model with the Langmuir parameters. Herein, the prediction model for methane adsorption in shales was built in 4 steps: a model of the Langmuir volume at experimental temperature, the temperature dependence of the Langmuir volume, a model of the Langmuir pressure at experimental temperature, the temperature dependence of Langmuir pressure.

The model of the Langmuir volume at experimental temperature considers the TOC and clay content but not the thermal maturity, which shows no relationship with the TOC-normalized Langmuir volume. The predicted Langmuir volume at experimental temperature was plotted against the measured results, showing a good R-square. However, more data is still required to improve the model, as shale samples in the TOC range of 10 to 25 wt% is rarely measured.

For the other three steps, the relationships are informative but not precise enough to provide a reliable prediction. A positive relationship exists between the TOC and decrease rate of Langmuir volume with increasing temperature based on the published data, which requires more data for the shale samples with TOC larger than 3 wt%. As the Langmuir pressure is sensitive to too many factors, it is hard to estimate using the TOC and clay content. The temperature dependence of Langmuir pressure is related to the TOC. Furthermore, as the high-pressure methane adsorption experiments on shales were measured under different conditions in the references, the amount of samples for the temperature dependence of the Langmuir parameters is insufficient, which limits the accuracy of the related models.

Moisture was not considered in this chapter, but is also regarded as an important controlling factor on methane adsorption in shales (Li et al., 2016; Wang and Yu, 2016; Zou et al., 2018). The moisture in shales occupies pore volume or blocks pore throats, thus reducing the adsorption capacity. However, the levels of moisture content used in

the references are too different to collect sufficient comparable data. Moreover, it is hard to determine the moisture content under in-situ conditions and its variation within a shale reservoir.

The major application of this work is that the well-log data can be used to calculate TOC and V_{sh} without any problem and therefore this study can help to calculate V_L and P_L at the reservoir condition for volumetric calculation of absorbed gas in shale reservoirs.

References

- Dang, W., Zhang, J., Wei, X., Tang, X., Chen, Q., Li, Z., Zhang, M. and Liu, J., 2017. Geological controls on methane adsorption capacity of Lower Permian transitional black shales in the Southern North China Basin, Central China: Experimental results and geological implications. *Journal of Petroleum Science and Engineering*, 152: 456-470.
- Fan, E., Shuheng Tang, Chenglong Zhang, Qiulei Guo and Sun, C., 2015 Methane sorption capacity of organics and clays in high-over matured shale-gas systems. *Energy, Exploration & Exploitation*, 32: 16.
- Gasparik, M., Bertier, P., Gensterblum, Y., Ghanizadeh, A., Krooss, B.M. and Littke, R., 2014a. Geological controls on the methane storage capacity in organic-rich shales. *International Journal of Coal Geology*, 123: 34-51.
- Gasparik, M., Rexer, T.F.T., Aplin, A.C., Billemont, P., De Weireld, G., Gensterblum, Y., Henry, M., Krooss, B.M., Liu, S., Ma, X., Sakurovs, R., Song, Z., Staib, G., Thomas, K.M., Wang, S. and Zhang, T., 2014b. First international inter-laboratory comparison of high-pressure CH₄, CO₂ and C₂H₆ sorption isotherms on carbonaceous shales. *International Journal of Coal Geology*, 132: 131-146.
- Guo, S., 2013. Experimental study on isothermal adsorption of methane gas on three shale samples from Upper Paleozoic strata of the Ordos Basin. *Journal of Petroleum Science and Engineering*, 110: 132-138.
- Guo, S., Lü, X., Song, X. and Liu, Y., 2017. Methane adsorption characteristics and influence factors of Mesozoic shales in the Kuqa Depression, Tarim Basin, China. *Journal of Petroleum Science and Engineering*, 157: 187-195.

- Ji, L., Zhang, T., Milliken, K.L., Qu, J. and Zhang, X., 2012. Experimental investigation of main controls to methane adsorption in clay-rich rocks. *Applied Geochemistry*, 27(12): 2533-2545.
- Ji, W., Song, Y., Jiang, Z., Chen, L., Li, Z., Yang, X. and Meng, M., 2015. Estimation of marine shale methane adsorption capacity based on experimental investigations of Lower Silurian Longmaxi formation in the Upper Yangtze Platform, south China. *Marine and Petroleum Geology*, 68, Part A: 94-106.
- Ji, W., Song, Y., Jiang, Z., Wang, X., Bai, Y. and Xing, J., 2014. Geological controls and estimation algorithms of lacustrine shale gas adsorption capacity: A case study of the Triassic strata in the southeastern Ordos Basin, China. *International Journal of Coal Geology*, 134–135: 61-73.
- Li, J., Li, X., Wang, X., Li, Y., Wu, K., Shi, J., Yang, L., Feng, D., Zhang, T. and Yu, P., 2016. Water distribution characteristic and effect on methane adsorption capacity in shale clay. *International Journal of Coal Geology*, 159: 135-154.
- Li, T., Tian, H., Xiao, X., Cheng, P., Zhou, Q. and Wei, Q., 2017. Geochemical characterization and methane adsorption capacity of overmature organic-rich Lower Cambrian shales in northeast Guizhou region, southwest China. *Marine and Petroleum Geology*, 86: 858-873.
- Liu, Y.C., Chen, D.X., Qiu, N.S., Wang, Y., Fu, J., Huyan, Y., Jia, J.K. and Wu, H., 2017. Reservoir characteristics and methane adsorption capacity of the Upper Triassic continental shale in Western Sichuan Depression, China. *Australian Journal of Earth Sciences*, 64(6): 807-823.
- Myers, A.L., 2004. Characterization of nanopores by standard enthalpy and entropy of adsorption of probe molecules. *Colloids and Surfaces A: Physicochemical and Engineering Aspects*, 241(1–3): 9-14.
- Wang, L. and Yu, Q., 2016. The effect of moisture on the methane adsorption capacity of shales: A study case in the eastern Qaidam Basin in China. *Journal of Hydrology*, 542: 487-505.
- Wang, Y., Zhu, Y., Liu, S. and Zhang, R., 2016. Methane adsorption measurements and modeling for organic-rich marine shale samples. *Fuel*, 172: 301-309.
- Xia, X., Litvinov, S. and Muhler, M., 2006. Consistent Approach to Adsorption Thermodynamics on Heterogeneous Surfaces Using Different Empirical Energy Distribution Models. *Langmuir*, 22(19): 8063-8070.

- Zhang, T., Ellis, G.S., Ruppel, S.C., Milliken, K., Lewan, M. and Sun, X., 2013. Effect of Organic Matter Properties, Clay Mineral Type and Thermal Maturity on Gas Adsorption in Organic-Rich Shale Systems, Unconventional Resources Technology Conference, Denver, Colorado, 12-14 August 2013, pp. 1996-2001.
- Zhang, T., Ellis, G.S., Ruppel, S.C., Milliken, K. and Yang, R., 2012. Effect of organic-matter type and thermal maturity on methane adsorption in shale-gas systems. *Organic Geochemistry*, 47: 120-131.
- Zou, J., Rezaee, R. and Liu, K., 2017. The effect of temperature on methane adsorption in shale gas reservoirs. *Energy & Fuels*.
- Zou, J., Rezaee, R., Xie, Q., You, L., Liu, K. and Saeedi, A., 2018. Investigation of moisture effect on methane adsorption capacity of shale samples. *Fuel*, 232: 323-332.

Chapter 6

Conclusions

Facing the decline of conventional gas resources, unconventional natural gas such as shale gas has drawn much attention all over the world. Within the shale gas system, a significant amount of adsorbed gas has been observed. To evaluate the gas storage in shale, it is necessary to understand the mechanisms of methane adsorption in shale. In this study, we analyzed shale samples from Western Australia to explore the controlling factors of methane adsorption capacity in shale. High-pressure methane adsorption and low-pressure nitrogen and carbon dioxide sorption experiments were carried out to obtain the characteristics of methane adsorption and pore structure, respectively. The results showed that external and internal parameters both have critical impacts on methane adsorption capacity in shale. External parameters such as pressure, temperature and moisture were comprehensively investigated by conducting experiments at various conditions; internal parameters related to the organic matter, inorganic matter and pore structure were also examined using experimental data measured in our lab and some data from the literature. Based on our findings of methane adsorption in shale, a prediction model for methane adsorption was constructed, which makes it possible to evaluate methane adsorption capacity in shale using well-log data. Besides, how the adsorbed gas influences gas transport in shale was taken into account, providing a better understanding of gas transport in shale. Although our detailed conclusions were addressed in each chapter, here comes the highlighted conclusions and understanding about methane adsorption in shale.

6.1 Concluding remarks

The effect of temperature on methane adsorption in shale is negative, as it is an exothermic process. However, this effect varies among shale samples with different compositions: high TOC shale samples are more sensitive to temperature increase than low TOC samples. It might infer that the effect of temperature on methane adsorbed on kerogen is greater than that on clay minerals. This finding helps to evaluate the

methane adsorption capacity in shale at reservoir temperature. A relationship between the TOC and temperature effect on methane adsorption can be obtained based on a sufficient database. Up to date, however, shale samples measured at different temperatures on high-pressure methane adsorption mostly have TOC lower than 3 wt%.

The effect of moisture on methane adsorption in shale was analyzed using a sample preparation method of pre-adsorbed water. The adsorbed water in shale occupies sorption sites or blocks pore network connectivity to reduce the methane adsorption in shale. This effect of moisture on methane adsorption decreases first and then keeps stable with increasing pressure, which implies the moisture effect is greater on small pores than bigger pores. Small pores like micropores can be thoroughly blocked by adsorbed water, while bigger pores like mesopores are less likely to be blocked. Moreover, the effect of moisture on methane adsorption is positively related to TOC. It might infer that adsorbed water not only blocks clay-hosted small pores directly but also organic matter-hosted small pores indirectly. This hypothesis is based on the assumption that water is preferentially adsorbed on clay minerals rather than organic matter in shale.

In addition, the comparison of pore structure characteristics between wet and dry samples show some information about the distribution of adsorbed water in shale. A shift to smaller pore size exists in PSD of big mesopores (16-50 nm) and macropores (>50 nm) for three analyzed shale samples. The phenomenon indicates that adsorbed water distributes in these pores as water film with a certain thickness, which can be generally determined by the distance of the shift. This finding offers an indirect method of measuring the thickness of adsorbed water in shale if it is a common phenomenon.

To evaluate methane adsorption capacity in shale under reservoir condition, it is necessary to understand the combined effect of moisture and high temperature on methane adsorption. Moisture and high temperature reduce the methane adsorption in shales individually, and the two factors weaken each other on methane adsorption when coexisting in shales. The possible reason is that both factors mainly work on small pores. Given the combined effect of moisture and high temperature, the methane adsorption capacity of shale may show no relationship with the TOC. As only one relative humidity (84%) was used in this study which offers a very high moisture level,

more experimental data obtained at different RH and a method determining the RH under reservoir condition are required.

Thermodynamic parameters such as the heat of adsorption and the standard entropy of adsorption were determined from the temperature dependence of the Langmuir pressure in this study. Comparing with the published data, the heat of adsorption for the dry samples in this study is lower due to the lower TOC and coarser particle size. The dry samples show a positive relationship between the heat of adsorption and the TOC, which suggests the process of methane adsorption on organic matter release more heat than that on clay minerals. As for the standard entropy of adsorption, methane adsorbed on clay minerals has more mobility than methane adsorbed on kerogen, which indicates different configurations of adsorbed methane between clay minerals and kerogen.

The difference in thermodynamic parameters between the dry and wet samples is due to the blocking of small pores by adsorbed water, illustrating that methane adsorbed in the blocked small pores release more heat and have less mobility comparing with the methane adsorbed in the big pores. As the findings of thermodynamic parameters are pore scale, it is necessary to explore the thermodynamic parameters at different adsorption layers to provide a better understanding.

Methane adsorption kinetics in shale were measured and the results were interpreted using the bidisperse diffusion model. The results of adsorption rate showed that pressure has a negative effect on methane adsorption rate, while temperature can positively affect the adsorption rate. Similarly, the pressure effect on the macropore diffusivity is negative, while the temperature effect on the macropore effective diffusivity is positive. A good positive relationship exists between the micropore volume (<2nm, from low-pressure CO₂ adsorption) and macropore effective diffusivity at low pressure (10bar), while no relationship was found between the sum mesopore and macropore volumes (<100nm) and the macropore effective diffusivity. Micropore therefore controls diffusion as a throat, which needs to be redefined to connect pores rather than as pore itself. Besides, a pore model considering adsorption layers is needed to address the effect of adsorbed methane on gas diffusion in shale, as the adsorption layers could narrow pore throat.

A prediction model was constructed for methane adsorption capacity in shale, considering both external (pressure and temperature) and internal parameters (TOC and clay content). The model provides good Langmuir volume at experimental temperature, which was plotted against measured results with a good correlation. However, more data of shale samples in the TOC range of 10 to 25 wt% are required to improve the model. It is hard to predict the methane adsorption capacity at reservoir temperature due to the uncertainties in the temperature dependence of the Langmuir pressure. The model can help log analysts to quantify adsorbed gas from well-log data since TOC and V_{sh} , which are the measure inputs of the introduced models, can be obtained from well-log data as well.

6.2 Limitations

Methane adsorption capacity in shales was investigated using high-pressure and low-pressure adsorption experiments at various conditions, on a limited amount of samples and analyzed using different methods. Therefore, there are some limitations to this study:

- Maximum of pressure in high-pressure methane adsorption experiment is 7 MPa (1015psi), which is not indicative of reservoir conditions.
- Shale samples measured on high-pressure methane adsorption at different temperatures have TOC ranging from 0.23 to 3.07 wt%, which is not representative for high TOC shales.
- Only one level of moisture content was examined in the investigation of moisture effect on methane adsorption capacity in shales.
- A low-temperature (40°C) degassing process was conducted for wet samples before low-pressure adsorption experiments, which removed pre-adsorbed water inevitably.
- The experimental temperature used in high-pressure methane adsorption for wet samples was up to 60°C, which is higher than the temperature for preparation of the wet samples.
- It was assumed that moisture distributes on clay minerals rather than kerogen in the investigation of moisture effect on methane adsorption capacity in shales.
- Temperature dependence of the Langmuir pressure was determined only based on three experimental temperatures.

- The number of shale samples analyzed on adsorption kinetics and diffusion in shale is limited.
- The prediction models for Langmuir parameters at reservoir temperature are not reliable enough.

6.3 Recommendations and future research:

Given the complex properties of shale and complicated controlling factors of methane adsorption capacity, more research studies on various shale samples are demanded. The following points are recommended for future research on methane adsorption of shales:

- Methane adsorption capacity in shales measured at reservoir pressure, which is much higher than the maximum pressure (7 MPa, 1015psi) used in this study.
- High-pressure methane adsorption experiments at reservoir temperature on shale samples with TOC larger than 3 wt%, which have rarely been conducted up to date. The results can help to quantitatively describe the relationship between methane adsorption capacity and temperature in shales.
- The temperature effect on methane adsorbed at different adsorption layers, which can provide a better understanding of temperature effect on methane adsorption in shale.
- The combined effect of high temperature and moisture on methane adsorption capacity in shales using various moisture content and shale samples to expand the finding of this study.
- Distribution of adsorbed water in shales to understand the mechanism of moisture reducing methane adsorption capacity.
- The effect of pore geometry on methane adsorption in shale, which compares the methane adsorption in slits and cylinders at a wide range of size.
- As the prediction model for the Langmuir parameters at reservoir temperature in this study is not reliable enough, more high-pressure methane adsorption isotherms need to be collected or measured.
- As the effective diffusivities in shales change with increasing pressure, the relationship between the methane adsorption capacity and permeability is important to characterize permeability and understand gas transport in shales.

- A new model combining high-pressure methane and low-pressure nitrogen and carbon dioxide to determine the pore structure of shale, which may provide pore size distribution of organic and inorganic matter.

Appendix I

Source	TOC (wt%)	Clay (%)	T (°C)	Mesh	VL (scf/ton)	PL(psi)	Tmax (°C)	Decrease rate of VL	
Wang et al. (2016)	7.68	35.4	30	60	152.9	337.9	N/A	N/A	
	4.24	34.8	30	60	126.4	346.6	N/A	N/A	
	2.18	37.8	30	60	77.3	378.5	N/A	N/A	
	1.46	48.7	30	60	60.4	287.2	N/A	N/A	
	5.23	34.1	30	60	74.9	688.9	N/A	N/A	
	4.82	38.5	30	60	95.3	455.4	N/A	N/A	
	1.76	36.1	30	60	42.7	507.6	N/A	N/A	
	8.54	29.3	30	60	108.4	632.4	N/A	N/A	
	10.02	37.4	30	60	117.6	551.1	N/A	N/A	
	2.17	27.2	30	60	18.4	103.0	N/A	N/A	
	4.4	20.1	30	60	34.3	101.5	N/A	N/A	
	3.9	28.7	30	60	32.8	210.3	N/A	N/A	
	Our unpublished data	0.28	76.58	25	60	87.7	296.1	442	N/A
		0.52	N/A	25	60	40.0	281.9	453	N/A
1.26		83.49	25	60	87.7	331.3	454	N/A	
3.2		74.28	25	60	89.3	372.4	454	N/A	
2.82		67.52	25	60	80.6	338.2	456	N/A	
2.6		54.90	25	60	80.0	420.2	453	N/A	
2.11		54.22	25	60	86.2	458.3	441	N/A	
1.24		37.10	25	60	42.6	317.1	453	N/A	
2.76		55.97	25	60	82.6	455.6	448	N/A	
0.75		68.44	25	60	69.0	372.5	458	N/A	
Guo et al. (2017)		0.5	26	30	60-80	26.1	233.5	589	N/A
		0.95	40	30	60-80	35.0	313.3	475	N/A
	0.81	42	30	60-80	27.5	358.2	533	N/A	
	0.76	41	30	60-80	28.3	243.7	477	N/A	
	1.05	46	30	60-80	51.6	407.6	444	N/A	
	0.7	42	30	60-80	33.9	384.4	424	N/A	
	0.98	45	30	60-80	36.0	522.1	574	N/A	
	1.3	47	30	60-80	51.6	384.4	460	N/A	
	5.76	55	30	60-80	166.3	742.6	458	N/A	
	1.55	60	30	60-80	84.4	509.1	455	N/A	
	0.87	33	30	60-80	31.1	298.8	494	N/A	
	2.24	48	30	60-80	62.5	375.6	442	N/A	
	2.57	49	30	60-80	75.9	265.4	442	N/A	
	1.22	36	30	60-80	41.0	264.0	474	N/A	
	2.42	43	30	60-80	73.5	340.8	441	N/A	
	2.47	43	30	60-80	96.4	385.8	463	N/A	
	5.35	70	30	60-80	163.1	481.5	447	N/A	
	5.33	70	30	60-80	142.0	465.6	453	N/A	
	4.59	60	30	60-80	108.4	319.1	452	N/A	
	1.55	55	30	60-80	55.1	295.9	469	N/A	
	1.48	36	30	60-80	57.6	446.7	462	N/A	
	25.31	23	30	60-80	427.6	467.0	501	N/A	
	2.39	36	30	60-80	59.0	423.5	460	N/A	
	24.58	68	30	60-80	266.6	480.1	424	N/A	
	1.02	58	30	60-80	39.6	319.1	571	N/A	
	1.17	35	30	60-80	43.1	449.6	434	N/A	
	1.38	57	30	60-80	43.8	224.8	492	N/A	
	1.62	52	30	60-80	53.0	239.3	444	N/A	
	28.48	35	30	60-80	478.5	564.2	436	N/A	
	(Ji et al., 2015; Ji et al., 2014)	1.41	N/A	20	60	93.9	195.8	N/A	0.3778
			N/A	40	60	85.5	220.5	N/A	
			N/A	60	60	84.0	380.0	N/A	
N/A			80	60	73.5	433.7	N/A		
N/A			100	60	62.2	475.7	N/A		
4.13		N/A	20	60	135.6	207.4	N/A	0.452	
		N/A	40	60	128.9	220.5	N/A		
		N/A	60	60	119.7	382.9	N/A		
		N/A	80	60	109.8	422.1	N/A		
		N/A	100	60	99.9	464.1	N/A		
0.45		N/A	20	60	59.7	192.9	N/A	0.2066	
		N/A	40	60	54.4	223.4	N/A		
		N/A	60	60	51.9	381.5	N/A		
		N/A	80	60	47.0	427.9	N/A		
0.87		N/A	20	60	77.3	197.3	N/A	0.3337	
		N/A	40	60	71.7	224.8	N/A		
		N/A	60	60	68.9	393.1	N/A		
		N/A	80	60	57.9	420.6	N/A		
0.8		N/A	20	60	74.5	185.7	N/A	0.2966	
		N/A	40	60	71.0	221.9	N/A		
		N/A	60	60	68.9	382.9	N/A		

	1.49	N/A	80	60	61.8	435.1	N/A	0.5279	
		N/A	100	60	49.4	464.1	N/A		
		N/A	20	60	100.6	191.5	N/A		
		N/A	40	60	98.2	227.7	N/A		
		N/A	60	60	92.5	387.3	N/A		
		N/A	80	60	74.5	438.0	N/A		
	0.62	N/A	100	60	59.7	468.5	N/A	0.3655	
		N/A	20	60	71.7	198.7	N/A		
		N/A	40	60	66.4	219.0	N/A		
		N/A	60	60	60.0	384.4	N/A		
		N/A	80	60	54.0	436.6	N/A		
	1.35	N/A	100	60	41.3	468.5	N/A	0.4379	
		N/A	20	60	85.8	195.8	N/A		
		N/A	40	60	80.5	217.6	N/A		
		N/A	60	60	74.2	381.5	N/A		
		N/A	80	60	64.3	427.9	N/A		
	5.15	N/A	100	60	50.1	449.6	N/A	1.8362	
		N/A	30	60	216.8	207.4	N/A		
		N/A	40	60	202.7	216.1	N/A		
		N/A	50	60	184.7	307.5	N/A		
		N/A	60	60	159.6	388.7	N/A		
	4.76	N/A	70	60	146.6	419.2	N/A	2.8497	
		N/A	30	60	205.9	206.0	N/A		
		N/A	40	60	184.7	214.7	N/A		
		N/A	50	60	140.9	248.0	N/A		
		N/A	60	60	111.6	298.8	N/A		
	(Zou et al., 2017)	3.03	51.3	25	60	51.3	218.9	459	0.3135
				45	60	46.3	277.8		
60				60	40.2	346.9			
80				60	37.6	433.8			
0.64		26	25	60	26.0	256.1	458	0.1538	
			45	60	23.1	306.7			
			60	60	20.6	322.5			
			80	60	19.8	429.2			
1.82		46.5	25	60	46.5	263.8	460	0.5846	
			45	60	35.2	352.3			
			60	60	26.0	492.2			
			80	60	N/A	N/A			
1.08		34.2	25	60	34.2	422.1	465	0.337	
			45	60	29.5	544.6			
			60	60	22.2	562.0			
			80	60	20.5	729.7			
0.23		26.5	25	60	26.5	383.5	N/A	0.1257	
			45	60	24.0	398.3			
			60	60	22.1	445.3			
			80	60	20.7	505.4			
3.07		76	25	60	80.6	338.2	452	0.8646	
			45	60	63.7	371.7			
			60	60	50.3	481.4			
			80	60	N/A	N/A			

‘Every reasonable effort has been made to acknowledge the owners of copyright material. I would be pleased to hear from any copyright owner who has been omitted or incorrectly acknowledged.’

Appendix II

Paper “**Effect of particle size on high-pressure methane adsorption of coal**”
Petroleum Research, Volume 1, Issue 1, 2016, Pages 53-58.

Reza Rezaee¹

¹ WASM: Minerals, Energy and Chemical Engineering, Curtin University, 6151
Kensington, Western Australia.

Name	conception and design	Acquisition of data & method	Data conditioning & manipulation	Analysis & statistical method	Interpretation & discussion	Final approval
Reza Rezaee	<input checked="" type="checkbox"/>	<input type="checkbox"/>	<input type="checkbox"/>	<input type="checkbox"/>	<input type="checkbox"/>	<input type="checkbox"/>

I acknowledge that these represent my contribution to the above research output.

X


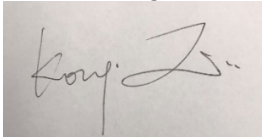
R.Rezaee

Paper “Effect of temperature on methane adsorption in shale gas reservoirs” *Energy & Fuels* **2017** 31 (11), 12081-12092.

Reza Rezaee¹ and Kouqi Liu²

¹ WASM: Minerals, Energy and Chemical Engineering, Curtin University, 6151 Kensington, Western Australia.

² Department of Petroleum Engineering, University of North Dakota, Grand Forks, ND 58202, USA

Name	conception and design	Acquisition of data & method	Data conditioning & manipulation	Analysis & statistical method	Interpretation & discussion	Final approval
Reza Rezaee	<input checked="" type="checkbox"/>	<input type="checkbox"/>	<input type="checkbox"/>	<input type="checkbox"/>	<input type="checkbox"/>	<input type="checkbox"/>
I acknowledge that these represent my contribution to the above research output.  <hr/> R. Rezaee						
Kouqi Liu	<input type="checkbox"/>	<input type="checkbox"/>	<input type="checkbox"/>	<input type="checkbox"/>	<input checked="" type="checkbox"/>	<input type="checkbox"/>
I acknowledge that these represent my contribution to the above research output. 						

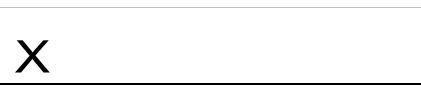

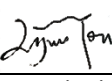
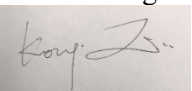

Paper “Investigation of moisture effect on methane adsorption capacity of shale samples” Fuel, Volume 232, 2018, Pages 323-332.

Reza Rezaee¹, Quan Xie¹, Lijun You², Kouqi Liu³, Ali Saeedi¹

¹ WASM: Minerals, Energy and Chemical Engineering, Curtin University, 6151 Kensington, Western Australia.

² State Key Laboratory of Oil and Gas Reservoir Geology and Exploitation, Southwest Petroleum University, Chengdu, Sichuan 610500, China


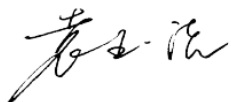
³ Department of Petroleum Engineering, University of North Dakota, Grand Forks, ND 58202, USA

Name	conception and design	Acquisition of data & method	Data conditioning & manipulation	Analysis & statistical method	Interpretation & discussion	Final approval
Reza Rezaee	<input checked="" type="checkbox"/>	<input type="checkbox"/>	<input type="checkbox"/>	<input type="checkbox"/>	<input type="checkbox"/>	<input type="checkbox"/>
I acknowledge that these represent my contribution to the above research output.						
 R.Rezaee						
Quan Xie	<input type="checkbox"/>	<input type="checkbox"/>	<input type="checkbox"/>	<input type="checkbox"/>	<input type="checkbox"/>	<input checked="" type="checkbox"/>
I acknowledge that these represent my contribution to the above research output.						
						
Lijun You	<input type="checkbox"/>	<input type="checkbox"/>	<input type="checkbox"/>	<input type="checkbox"/>	<input type="checkbox"/>	<input checked="" type="checkbox"/>
I acknowledge that these represent my contribution to the above research output.						
						
Kouqi Liu	<input type="checkbox"/>	<input type="checkbox"/>	<input type="checkbox"/>	<input type="checkbox"/>	<input checked="" type="checkbox"/>	<input type="checkbox"/>
I acknowledge that these represent my contribution to the above research output.						
						
Ali Saeedi	<input type="checkbox"/>	<input checked="" type="checkbox"/>	<input type="checkbox"/>	<input type="checkbox"/>	<input type="checkbox"/>	<input type="checkbox"/>
I acknowledge that these represent my contribution to the above research output.						
						

Paper “Investigation on the adsorption kinetics and diffusion of methane in shale samples” Journal of Petroleum Science and Engineering, Volume 171, 2018, Pages 951-958.

Reza Rezaee¹, Yujie Yuan¹

¹ WASM: Minerals, Energy and Chemical Engineering, Curtin University, 6151 Kensington, Western Australia.

Name	conception and design	Acquisition of data & method	Data conditioning & manipulation	Analysis & statistical method	Interpretation & discussion	Final approval
Reza Rezaee	<input checked="" type="checkbox"/>	<input type="checkbox"/>	<input type="checkbox"/>	<input type="checkbox"/>	<input type="checkbox"/>	<input type="checkbox"/>
I acknowledge that these represent my contribution to the above research output.						
<div style="border: 1px solid black; padding: 5px; width: fit-content;">  </div> <p>R.Rezaee</p>						
Yujie Yuan	<input type="checkbox"/>	<input type="checkbox"/>	<input type="checkbox"/>	<input type="checkbox"/>	<input checked="" type="checkbox"/>	<input type="checkbox"/>
I acknowledge that these represent my contribution to the above research output.						
						

Paper “A Prediction Model for Methane Adsorption Capacity in Shale Gas Reservoirs” Energies, Volume 12, 2019.

Reza Rezaee¹

¹ WASM: Minerals, Energy and Chemical Engineering, Curtin University, 6151 Kensington, Western Australia.

Name	conception and design	Acquisition of data & method	Data conditioning & manipulation	Analysis & statistical method	Interpretation & discussion	Final approval
Reza Rezaee	<input checked="" type="checkbox"/>	<input type="checkbox"/>	<input type="checkbox"/>	<input type="checkbox"/>	<input type="checkbox"/>	<input type="checkbox"/>
<p>I acknowledge that these represent my contribution to the above research output.</p> <p style="text-align: center;">X</p> <hr style="width: 30%; margin-left: 0;"/> <p>R.Rezaee</p>						